University of Calgary

PRISM Repository **https://prism.ucalgary.ca**

The Vault Open Theses and Dissertations

2016

The Role of THF Hydrate Veins on the Geomechanical Behaviour of Hydrate-Bearing Fine Grained Soils

Wu, Jiechun

Wu, J. (2016). The Role of THF Hydrate Veins on the Geomechanical Behaviour of Hydrate-Bearing Fine Grained Soils (Master's thesis, University of Calgary, Calgary, Canada). Retrieved from https://prism.ucalgary.ca. doi:10.11575/PRISM/28366

http://hdl.handle.net/11023/3536

Downloaded from PRISM Repository, University of Calgary

UNIVERSITY OF CALGARY

The Role of THF Hydrate Veins on the Geomechanical Behaviour of Hydrate-Bearing Fine Grained Soils

by

Jiechun Wu

A THESIS

SUBMITTED TO THE FACULTY OF GRADUATE STUDIES

IN PARTIAL FULFILMENT OF THE REQUIREMENTS FOR THE

DEGREE OF MASTER OF SCIENCE

GRADUATE PROGRAM IN CIVIL ENGINEERING

CALGARY, ALBERTA

DECEMBER, 2016

© Jiechun Wu 2016

Abstract

Natural gas hydrate, which can form complex vein structures within fine-grained sediments, pose a significant geohazard if the hydrate were to dissociate. Therefore, understanding the role of hydrate veins on the geomechanical behavior of hydrate-bearing fine-grained sediments is essential for sediment stability assessment.

This thesis presents the results of a laboratory study conducted to further understand the fine-grained soil behaviour with simplified cylindrical tetrahydrofuran (THF) hydrate veins within the soil. Compression tests were conducted on standalone THF hydrate veins of different diameters to determine their strength and stiffness. Subsequent consolidated undrained (CU) triaxial tests were conducted to determine the behaviour of fine-grained soils containing the same-size hydrate veins. Factors such as vein size and effective stress were considered to develop relationships between vein size and strength/stiffness of the hydrate-bearing soil. The results are used to consider the role that hydrates veins may have on natural sediments formed at different depths.

Acknowledgements

First of all, I would like to thank my supervisor, Dr. Jeffrey Priest, for supporting and mentoring me at University of Calgary, as well as giving me the opportunity to be challenged and learn as a student and a researcher. I also would like to thank Dr. Jocelyn Grozic for mentoring and enlightening me during my M.Sc. study. And thank you so much for your advice on my future career!

I would like to acknowledge Drs. R. Wong, M. Dann, B. Moorman for providing their perspectives and knowledge of engineering. I also would like to thank the technical staff at Department of Civil Engineering. I could have never overcome all the challenges in my laboratory work without their help. Special thanks to Mirsad Berbic for his technical support.

I would like to thank my fellow graduate students and friends in the department: Aditi Khurana, Chee Wong, Heli Gong, Jithamala Caldera, Qiang Chen, Scott McKean, Shuai Man for their advice and help on my courses and research during my M.Sc study. Special thanks to Will Smith for helping me start my research in the gas hydrate laboratory, teaching me about the experimental programs as well as mentoring and guiding me as a good friend!

Finally, I would like to thank my parents for their love, support and encouragement for the last 24 years! I would have never made this far without you. Also, I need to thank my lovely girlfriend Michelle. Meeting you is one of the greatest things happened in my life!

Table of Contents

Abstract ii
Acknowledgements iii
Table of Contents iv
List of Tables vi
List of Figures and Illustrations vii
List of Symbols, Abbreviations and Nomenclature xi

CHAPTER ONE: INTRODUCTION 1
1.1 Statement of problem 1
1.2 Objective of Research 2
1.3 Scope of Investigation 2
1.4 Outline of Thesis 3

CHAPTER TWO: LITERATURE REVIEW 5
2.1 Introduction 5
2.2 Characteristics of gas hydrate 5
2.3 Hydrate occurrence in nature 7
2.4 Experimental research on gas hydrate 10
2.4.1 Hydrate formation. 10
2.4.1.1 Formation in coarse-grained sediments. 11
2.4.1.2 Formation in fine-grained sediments. 12
2.4.2 Impact of hydrate on geomechanical behavior of sediments. 13
2.4.2.1 Previous research on coarse-grained sediments 14
2.4.2.2 Previous research on fine-grained sediments. 15
2.5 Summary 17

CHAPTER THREE: EXPERIMENTAL PROCEDURE 29
3.1 Introduction 29
3.2 Specimen Preparation 29
3.2.1 Soil preparation. 29
3.2.2 Hydrate veins formation. 30
3.2.3 Hydrate-bearing specimen formation. 31
3.3 Testing apparatus 32
3.4 Specimen mounting and cell assembly 33
3.4.1 Compression testing of THF vein specimens. 33
3.4.2 Compression testing of hydrate-bearing soil specimens. 34
3.5 Experimental test procedure 34
3.5.1 Compression testing on standalone synthetic hydrate cylindrical veins. 34
3.5.2 CU testing on soil specimens with and without hydrate. 35
3.6 Test parameters 36
3.6.1 Stress-strain behavior. 36
3.6.1.1 Deviatoric stress. 36
3.6.1.2 Axial strain. 37

3.6.1.3 Undrained shear strength. 37
3.6.1.4 Stiffness. 38
3.6.2 Pore pressure response. 38
3.6.3 Strength criteria. 39
3.6.4 q-p' stress behavior....40

CHAPTER FOUR: LABORATORY RESULTS AND DISCUSSION....56
4.1 Introduction....56
4.2 Baseline Compression Testing on Hydrate Veins 56
4.2.1 Stress-strain behavior. 56
4.2.1.1 Rate of shearing. 58
4.2.1.2 Confining pressure. 58
4.2.2 Failure mode. 59
4.3 Consolidated-Undrained (CU) Compression Testing....60
4.3.1 Stress-strain behavior. 60
4.3.2 Pore pressure response. 61
4.3.3 Effective stress paths. 62
4.3.4 Strength criteria. 63
4.3.5 Failure modes and post-shear analysis. 64
4.4 Geomechanical impact of THF hydrate veins and effective stress on hydrate-bearing specimens....65
4.4.1 Geomechanical impact of THF hydrate veins on hydrate-bearing specimens.65
4.4.1.1 Strength dependency on hydrate vein size. 66
4.4.1.2 Stiffness dependency on hydrate vein size. 67
4.4.2 Geomechanical impact of soil's effective stress on hydrate-bearing specimens. 68
4.4.2.1 Strength dependency on effective stress. 68
4.4.2.2 Stiffness dependency on effective stress. 69
4.4.3 Stiffness-strength correlation. 69
4.5 Potential impact of hydrate veins on natural sediments 70
4.6 Summary....72

CHAPTER FIVE: CONCLUSION....99
5.1 Overview....99
5.2 Summary of laboratory program....99
5.3 Conclusions....100
5.4 Recommendations....103

BIBLIOGRAPHY....104

List of Tables

Table 4.1: Summary of compression tests on hydrate vein specimens..... 74

Table 4.2: Summary of CU tests on hydrate-free and hydrate-bearing specimens. 74

List of Figures and Illustrations

Figure 2.1: (a) Structure I and (b) Structure II for gas hydrate (Sloan & Koh, 2007). 19

Figure 2.2: Hydrate stability zone in marine environment (Sloan & Koh, 2007). 20

Figure 2.3: (a) Thin, high angle gas hydrate veins from Krishna-Godavari Basin; (b) Partially dissociated core from Krishna-Godavari Basin; (c) Massive gas hydrate nodule from Krishna-Godavari Basin; (d) Gas hydrate layer and nodule from Gulf of Mexico; (e) Hydrate-bearing sandstone from Mount Elbert; (f) Gas hydrate in gravel from Mallik, Canada permafrost-hosted deposits (Winters, 2011). 21

Figure 2.4: X-ray CT images of samples from the Krishna-Godavari Basin showing pervasive hydrate veins forking and branching (white) and ice (blue) (Rees et al., 2011)... 22

Figure 2.5: Gas hydrate resource pyramid (Boswell & Collett, 2006). 23

Figure 2.6: Shear strength as a function of hydrate concentration for three effective confining stress (0.5,1 and 3 MPa). The methane hydrate results for σ_0' = 1 MPa are from Masui et al. (2005), and the results for σ_0' = 3 MPa are from Ebinuma et al. (2005). Solid triangles and squares denote sand mixtures with methane hydrate formed by gas percolation, and open triangles and squares represent methane hydrate formed from ice seeds. Filled circles show the sand-THF hydrate data from Yun et al. (2007) at 1 MPa (solid) and at 0.5 MPa (open circles) (Yun et al., 2007). 24

Figure 2.7: Stress-strain plots for sieved Ottawa sand (SOS) and Mackenzie Delta 2L-38 (MD) samples containing pore-fillings (Winters et al., 2004). 25

Figure 2.8: Shear strength of coarse-grained sediments as a function of effective confining pressure (Yun et al., 2007) 26

Figure 2.9: Stiffness of coarse-grained sediments as a function of effective confining pressure (Yun et al., 2007). 26

Figure 2.10: Shear strength of fine-grained sediments as a function of effective confining pressure (Yun et al., 2007). 27

Figure 2.11: Stiffness of fine-grained sediments as a function of effective confining pressure (Yun et al., 2007). 27

Figure 2.12: Comparison of (a) undrained shear strength and (b) undrained stiffness vs. hydrate vein area ratio, showing both undrained shear strength and undrained stiffness increase with hydrate saturation or hydrate vein area ratio (Smith, 2016). 28

Figure 3.1: Grain size distribution curve for the prepared fine-grained soil (Smith, 2016). 42

Figure 3.2: Sealed bucket that is able to be applied vacuum used to deair the slurry. 43

Figure 3.3: Specially designed and constructed consolidation cell with aluminum top plate built with a ram which can be connected to the load frame. 44

Figure 3.4: Extrusion tube of 70mm diameter used to extrude the fine-grained soil specimens.. 45

Figure 3.5: Formed (a) 0.25”, (b) 0.5”, (c) 0.75” and (d) 1”-diameter hydrate cylindrical veins within the aluminum foil molds. 46

Figure 3.6: Formed (a) 0.5”, (b) 0.75” and (c) 1”-diameter hydrate cylindrical veins unwrapped from the aluminum foil molds..... 47

Figure 3.7: (a) 0.25”, (b) 0.5”, (c) 0.75” and (d) 1”wood augers used to drill holes in the center of the fine-grained soil specimens for the placement of hydrate veins. 48

Figure 3.8: (a) 0.5”, (b) 0.75” and (c) 1”-diameter hydrate veins wrapped in a thin plastic wrap..... 49

Figure 3.9: A hydrate-bearing fine-grained soil specimen containing a 1”-diameter hydrate vein. 50

Figure 3.10: Modified low-temperature triaxial system including (a) 25 kN load frame and cell, (b) controlling system including two coolers, cooling tubes and cooling base plate (c) designed and constructed cooling system. 51

Figure 3.11: Schematic diagram of the modified low-temperature triaxial system. 52

Figure 3.12: Typical (a) excess pore pressure and (b) pore pressure coefficient (A) response to strain..... 53

Figure 3.13: Example plot for the strength criteria of the specimens. 54

Figure 3.14: Typical effective stress path for specimen. 55

Figure 4.1: Deviatoric load against axial strain for different diameters of hydrate veins. 76

Figure 4.2: Deviatoric stress against axial strain for different diameters of hydrate veins. 76

Figure 4.3: Peak stress applied to hydrate veins against cross-sectional area for the different hydrate veins. 77

Figure 4.4: Stiffness of hydrate veins against cross-sectional area for the different hydrate veins. 78

Figure 4.5: Deviatoric load against axial strain for hydrate vein specimens of (a) 0.5”, (b) 0.75” and (c) 1” diameter subjected to different strain rates. 79

Figure 4.6: Schematic diagram showing the stress condition of CU and UU tests on soil specimens. 80

Figure 4.7: Deviatoric load against axial strain for 1”-diameter hydrate vein specimens under 0 kPa and 500 kPa confining pressure. 81

Figure 4.8: Image of 0.5”-diameter hydrate vein showing failure due to horizontal fracturing. .. 82

Figure 4.9: Image of 0.75”-diameter hydrate vein showing failure due to diagonal fracturing. .. 83

Figure 4.10: Stress-strain curves for hydrate-free and hydrate-bearing specimens under 100 kPa effective stress. 84

Figure 4.11: Stress-strain curves for hydrate-free and hydrate-bearing specimens under 200 kPa effective stress. 85

Figure 4.12: Stress-strain curves for hydrate-free and hydrate-bearing specimens under 400 kPa effective stress. 86

Figure 4.13: Stress-strain curves for fine-grained specimens containing (a) no veins, (b) 0.25”-diameter vein, (c) 0.5”-diameter vein, (d) 0.75”-diameter vein and (e) 1”-diameter vein under different effective stress (100, 200 and 400 kPa)..... 87

Figure 4.14: Excess pore pressure measured during loading within (a) hydrate-free sediments and hydrate-bearing sediments containing (b) 0.25”-diameter hydrate vein, (c) 0.5”-diameter hydrate vein, (d) 0.75”-diameter hydrate vein and (e) 1”-diameter hydrate vein under different effective stress (100, 200 and 400 kPa). 88

Figure 4.15: Pore pressure coefficient (A) calculated for (a) hydrate-free sediments and hydrate-bearing sediments containing (b) 0.25”-diameter hydrate vein, (c) 0.5”-diameter hydrate vein, (d) 0.75”-diameter hydrate vein and (e) 1”-diameter hydrate vein under different effective stress (100, 200 and 400 kPa)..... 89

Figure 4.16: Effective stress path in q-p’ space for (a) hydrate-free sediments and hydrate-bearing sediments containing (b) 0.25”-diameter hydrate vein, (c) 0.5”-diameter hydrate vein, (d) 0.75”-diameter hydrate vein and (e) 1”-diameter hydrate vein under different effective stress (100, 200 and 400 kPa). 90

Figure 4.17: Mohr circles of stress, including Mohr-Coulomb failure lines for (a) hydrate-free sediments and hydrate-bearing sediments containing (b) 0.25”-diameter hydrate vein, (c) 0.5”-diameter hydrate vein, (d) 0.75”-diameter hydrate vein and (e) 1”-diameter hydrate vein. 91

Figure 4.18: Values of cohesion derived from Mohr-Coulomb failure criteria for fine-grained specimens as a function of the cross-sectional area of hydrate vein within the fine-grained specimens. 92

Figure 4.19: Examples of different failure modes of hydrate veins in hydrate-bearing specimens including (a) horizontal fracturing, (b) diagonal fracturing and (c) plastic creep failure..... 93

Figure 4.20: Undrained shear strength, Su as a function of hydrate vein area ratio for the specimens under different effective stress (100, 200 and 400 kPa)..... 94

Figure 4.21: Stiffness, E50 as a function of hydrate vein area ratio for the specimens under different effective stresses (100, 200 and 400 kPa). 95

Figure 4.22: Undrained shear strength as a function of effective stress for the specimens with different hydrate vein area ratio. 96

Figure 4.23: Stiffness as a function of hydrate vein area ratio for the specimens under different effective stresses (100, 200 and 400 kPa). 97

Figure 4.24: Correlation between undrained shear strength and stiffness of the hydrate-free and hydrate-bearing specimens. 98

List of Symbols, Abbreviations and Nomenclature

A	Pore pressure coefficient
AR	Hydrate vein area ratio
$A_{Specimen}$	The specimen area
A_{Vein}	The cross-sectional area of the vein
c’	Effective cohesion
C_4H_8O	Tetrahydrofuran
CU	Consolidated undrained
E_{50}	Secant modulus
H_0	Height of specimen after consolidation
LVDT	Linear voltage displacement transducer
p’	Effective mean normal stress
q	Deviatoric stress
q_{cs}	Deviatoric stress when specimen reaches the critical state
Q	Deviatoric load
S_h	Hydrate saturation
S_u	Undrained shear strength
S_{vh}	Hydrate vein saturation
THF	Tetrahydrofuran
u	Pore water pressure

u_0	Initial pore water pressure
u_{excess}	Excess pore water pressure
UU	Unconsolidated undrained
V_h	Hydrate volume
V_{vein}	Volume of hydrate vein
V_v	Void volume
$V_{v(soil)}$	Volume of voids in the surrounding soil
ε_a	Axial strain
ε_{cs}	Axial strain corresponding to deviatoric stress at the critical state
σ_0’	Effective confining stress
σ_1	Axial stress
σ_3	Cell pressure
σ_3’	Effective cell pressure
τ	Shear stress
ϕ’	Effective friction angle
ΔH	Axial displacement

Chapter One: Introduction

1.1 Statement of problem

Gas hydrates are ice-like compounds formed of methane gas and water that are stable under certain temperature and pressure conditions that exist within the sediments on the continental margins of the world's oceans and beneath permafrost in the Arctic (Sloan & Koh, 2008). Significant volumes of methane gas are sequestered in the form of gas hydrate, which can be released through hydrate dissociation if the temperature and pressure conditions are sufficiently altered. Therefore, in the recent years, gas hydrate has attracted considerable attention due to its potential as a significant future energy source (Boswell & Collett, 2011), a driver for global climate change (Haq, 1998) and a trigger for geotechnical hazards, since hydrate dissociation can significantly reduce the strength of sediments. (Sultan et al., 2007; Waite et al., 2009; Nimblett et al., 2005; Kayen & Lee, 1991; Grozic, 2010)

The physical properties of hydrate-bearing sediments, and the changes in sediment behavior during hydrate dissociation, is heavily dependent on the hydrate morphology and where it forms within the sediment. In fine-grained soils the hydrate has been found to exist as a complex vein structure, which might have an influence on the geomechanical behavior of these hydrate-bearing fine-grained sediments. However, the impact of gas hydrate veins on the behavior of fine-grained sediments is not clearly understood and thus improving our understanding is important to assess the risk that gas hydrates may pose.

1.2 Objective of Research

To better understand and quantify the impact of hydrate veins on the behavior of fine-grained soils, the following objectives are proposed to be accomplished:

(a) Improve the procedure for the formation of THF hydrate veins within fine-grained soils, in order to mimic the natural hydrate-bearing fine-grained sediments.
(b) Develop a technique and procedure for the testing of standalone THF hydrate veins for better understanding the mechanical behavior of THF hydrate veins
(c) Investigate the impact of hydrate veins of different sizes and the influence of effective stress on the strength behavior of hydrate-bearing fine-grained soils

1.3 Scope of Investigation

To accomplish the research objectives, hydrate-bearing fine-grained soil specimens were formed in the laboratory in an attempt to try and mimic natural hydrate-bearing fine-grained sediments. Cylindrical vertical hydrate veins, formed of THF, were placed into preformed voids within a fine-grained soil specimen. Consolidated undrained triaxial compression tests were then carried out on soil specimens with hydrate veins of varying diameters in order to better understand the inclusion of these hydrate veins on the strength of the soil specimens. As expected, increasing size of hydrate veins led to increases in soil strength compared to the non-hydrate bearing soil specimen. It is anticipated that the results of these tests will provide new insights on the impact of hydrate veins on fine-grained soil behavior and allow an assessment of the risk that subsequent hydrate dissociation may have on soil stability.

1.4 Outline of Thesis

Chapter one addresses the objectives of this research and how this research will contribute to the understanding of the impact of hydrate veins on the geomechanical behavior of hydrate-bearing fine-grained soils.

Chapter two provides an introduction to gas hydrate including its formation and morphology in nature. Previous research on gas hydrate formation techniques and geomechanical testing are also presented in this chapter.

Chapter three presents the experimental testing program that was carried out in this research. The methodology for forming cylindrical THF hydrate veins and subsequent hydrate-bearing soil specimens is presented. The detailed experimental methodology that was adopted to better understand the impact of hydrate veins on the geomechanical behavior of hydrate-bearing fine-grained soils is then described along with a description of the test parameters applicable to the triaxial test apparatus.

Chapter four illustrates and analyzes the results of the testing program carried out to better understand the role of hydrate veins on the geomechanical behavior of hydrate-bearing fine-grained soil specimens. The effect of test conditions such as effective stress condition, strain rates and hydrate veins size were investigated to develop a relationship between hydrate veins and the strength/stiffness of hydrate-bearing fine-grained soil specimens.

Chapter five summarizes the research carried out highlighting some of the main conclusions of the research as well as presenting recommendations for future research to overcome some of the limitation of this research.

Chapter Two: Literature Review

2.1 Introduction

This chapter provides an introduction and a review of gas hydrate within soils based on current knowledge. This chapter focuses on our current understanding of the morphologies of gas hydrate in different sediments and the physical properties of these hydrate-bearing sediments. In particular laboratory techniques applied to form hydrate in soil specimens are discussed and tests carried out on the specimens to determine the geomechanical behavior of hydrate-bearing soil specimens are highlighted.

2.2 Characteristics of gas hydrate

Gas hydrates are ice-like crystalline clathrate compounds formed of hydrocarbon gas molecules encaged in a lattice of hydrogen-bonded water molecules. In nature the most common gas encaged in the hydrate is methane, although higher hydrocarbon gases are encountered (ethane, propane). The size of the gas molecule within the water cages determines the structure of the gas hydrate (Sloan, 1998). The most common structure observed is Structure 1 hydrate (Figure 2.1a), which has small cages that are stabilized by small gas molecules such as methane. Another common structure is Structure 2 (Figure 2.1b) that has larger cages and are stabilized by heavier hydrocarbon gases (ethane, propane, etc.) and predominantly formed in pipelines. The hydrogen bonds within the hydrate structure leads to gas molecules being more densely packed together than when in its gas phase; 1 m^3 of gas hydrate will release 164m^3 of gas at STP (Kvenvolden, 1998).

Gas hydrates are thermobaric and exist under unique conditions of temperature and pressure (Sloan, 1998) that are typically found below the permafrost or within deep-water marine sediments. Gas hydrate occurs at different depths within these sediments and depends on the surface temperature (air or water) and the geothermal gradient within the sediment. The hydrate stability zone for marine environments is illustrated in Figure 2.2. It can be seen that it is technically possible for hydrates to exist in water depth of around 300m, however the ocean temperatures at this depth are around 7^{o}C in the specific temperature-pressure condition shown in Figure 2.2 (this is generally true of all oceans except the Arctic Ocean where water temperatures can approach 0^{o}C at these depths) and therefore hydrates are typically found in water depths greater than 1000m (Clennell et al., 1999).

The temperature and pressure conditions for gas hydrate stability and therefore the depths over which they are found is also dependent on water salinity and the type of gas molecules present. The presence of salts depresses water activity and pushes the hydrate stability envelope in Figure 2.2 to the right (higher pressure at a given temperature) (Dickens and Quinby-Hunt, 1997) while the presence of larger gas molecules (such as carbon dioxide, hydrogen sulphide and higher order hydrocarbons (ethane, propane)) gives rise to structure 2 hydrates and pushes the stability curve to the left (lower pressure at a given temperature) (Sloan, 1998). In addition, the size of the pore space, related to whether the host sediments is coarse grained or fine grained also has an impact on the depths that hydrate exist (Clennell et al., 1999). Reduction of pore sizes in fine grained sediments lead to an increase in capillary pressures that requires an extra thermodynamic drive to form hydrates, thus pushing the hydrate stability curve to the right. Therefore gas hydrates can exist over a wide range of depths with the sediment column.

2.3 Hydrate occurrence in nature

Gas hydrates are ubiquitous within sediments on the continental margins of all the world's oceans and deep seas and evidenced in recovered core samples from a multitude of drilling expeditions that have taken place, such as those in the Gulf of Mexico, the Cascadia continental margin of North America, the Black Sea, the Caspian Sea, the Sea of Okhotsk, the Sea of Japan, the Atlantic Ocean, Artic Ocean, India, China and South Korea (Collett et al., 2009).

Changes in temperature and pressure that occur during core recovery from the seafloor leads to significant dissociation of the gas hydrate, with only large forms of gas hydrate surviving the journey from the seafloor to the drill deck. Therefore most gas hydrates occurrences are inferred through the influence of gas hydrate dissociation on core samples, such as cold spots in the core sample (hydrate dissociation is an endothermic reaction), reduced salinity of core sample pore water (gas hydrate is formed from pure water) and excess gas pressure in the core (hydrate dissociation releases large quantities of gas). Therefore meaningful characterisation of how hydrate forms within the sediment and its impact on sediment properties was problematic.

To help address this shortfall in understanding of the behaviour of gas hydrate-bearing sediments pressure coring tools were developed that helped reduce sample disturbance in these sediments by maintaining pore pressure and temperature within the hydrate stability zone during core recovery (Schultheiss et al., 2006, 2008). Numerous drilling expeditions using pressure coring techniques have been dedicated to locating marine gas hydrate and understanding the geological and geotechnical behavior of gas hydrate-bearing soil sediments. These include the India

National Gas Hydrate Program (NGHP) Expedition 01 (Collett et al., 2008), offshore of China (Zhang et al., 2007), the Ulleung Basin Gas Hydrate expedition 1 (UBGH1) (Bahk et al., 2009; Kim et al., 2011), the Ulleung Basin Gas Hydrate expedition 2 (UBGH2) (Kim et al., 2013) and have greatly contributed to our understanding of marine gas hydrates and hydrate-bearing sediments.

Samples recovered from these drilling expeditions have shown that hydrate morphology is strongly dependent on the type of sediment in which it grows ranging from being disseminated within the pore space in coarse-grained sediments (Winters, 2011) through to the formation of hydrate nodules, veins or fractures in fine-grained sediments (Rees et al., 2011; Priest et al., 2014). This phenomenon can be explained by the notion that the growth of gas hydrate is dependent on the lithology of the sediments (Brewer et al., 1998; Clennell et al., 1999; Ruppel et al., 1997). The different forms of gas hydrates occurrences within different sediments are highlighted in Figure 2.3.

Disseminated natural gas hydrate is typically observed within coarse-grained sediments (Collett, 1999; Winters et al., 1999a). The large pore sizes in coarse-grained sediment allows gas hydrate to nucleate and grow within the void space. The large void spaces in coarse-grained sediments gives rise to higher initial permeability, which readily allows methane gas to flow through the sediment helping the homogenous distribution of disseminated gas hydrate to grow within the pore space (Collett, 1993).

In fine-grained sediments, the small pore size and high capillary pressure inhibit the growth of disseminated hydrate within the pore space (Clennell et al., 1999). As such hydrate in fine-grained sediments exhibit a 'grain displacing' morphology that includes discrete nodules, complex veins and planer sheets structures (Cook et al., 2008; Kim et al., 2013; Rees et al., 2011; Winters et al., 2011). Figure 2.4 shows the complex vein structure of samples recovered from NGHP1. This form of hydrate can be generated by two mechanisms: (1) The fracture existed before the hydrate was formed and acted as a conduit for fluid flow and veined/fractured hydrate formation. (2) Hydraulic fracturing can be induced by increased fluid pressure due to free gas or pore fluid flow (Rees et al., 2011). The growth of hydrate will continue if methane gas saturated fluid pressure is greater than the effective confining stress of the fine-grained sediments (Scherer, 1993).

A 'resource pyramid' for gas hydrate shown in Figure 2.5 highlights occurrences of gas hydrate within different sediment types and displays the relative volume of hydrates in a giving setting with the most promising resources at the top and the most technically challenging at the base. The pyramid highlights that although the most promising hydrate resources occur in high porosity sand-dominated and gravel formations where high hydrate saturation can occur this is only a small portion of the hydrates within marine sediments. The largest occurrence of gas hydrates is found within fine-grained sediments. Although high hydrate saturations can occur in these sediments the recovery of methane from them is problematic due to the low permeability and potential failure of the sediment without hydrate (Boswell & Collett, 2006). Therefore, understanding the behavior of hydrate-bearing coarse-grained sediments is important for

extraction of methane, understanding the behavior of hydrate-bearing-bearing fine-grained sediments maybe more important for assessing its impact as a geohazard.

2.4 Experimental research on gas hydrate

Due to the extreme environments in which gas hydrates form, related to the hydrate stability conditions, obtaining and testing of intact naturally occurring hydrate-bearing sediment samples for detailed characterization is difficult and expensive. Although in recent years pressure coring techniques have enabled cores to be recovered under in-situ pressures, the testing of such cores has been very limited due to lack of testing apparatus that would enable transfer of core samples from the pressure core holder to the apparatus without releasing the in-situ pressures. Therefore, the vast majority of research into the influence of gas hydrate on sediment behaviour has focused on characterizing the behaviour of laboratory synthesised hydrate-bearing soil specimens.

2.4.1 Hydrate formation.

The formation of gas hydrate within laboratory prepared specimens is challenging due to hydrate stability condition that are required along with the low solubility of methane in water (Stoll & Bryan, 1979; Winters et al., 2000). As it was assumed that hydrate preferentially formed in coarse-grained sediments and was inhibited in fine-grained soils much research to date has been conducted on characterising hydrate-bearing sands specimens, and only in the last few years has research been conducted on hydrate-bearing fine-grained specimens.

2.4.1.1 Formation in coarse-grained sediments.

Early attempts at forming gas hydrate in coarse-grained sediments involved injecting methane gas directly into a water saturated sand sample at pressure and temperature conditions suitable for hydrate stability. As hydrate forms at the gas/water interface, the injection of gas led to hydrate forming at or close to the inlet port creating blockages that prevented further gas injection, also they were unable to control the subsequent distribution of the formed hydrate (Makogon, 1981). Subsequent researchers developed different techniques to control the formation, volume and/or distribution of gas hydrate in sands. One technique involved flushing water supersaturated with methane gas through a specimen with a temperature gradient between the inlet and outlet ports such that hydrate formation was initiated within the specimen (Spangenberg et al., 2005). Although this technique was effective at creating hydrate disseminated throughout the specimen, the time for hydrate formation was of the order of months. In addition, the distribution could not be easily controlled. To reduce the formation time another technique adopted was the 'excess gas method' where a finite volume of water is added to the dry sediment, either as a fluid (Priest et al., 2005) or as ice crystals (Stern et al., 1996, Masui et al., 2005) with gas subsequently injected into the pore space, increasing pore pressure into the hydrate stability field to initiate hydrate formation. An alternative technique, termed the 'excess water' method (Priest et al., 2009) was used that controlled hydrate saturation by limiting the volume of gas injected into the specimen with water subsequently injected increasing the pore pressure to initiate hydrate formation.

2.4.1.2 Formation in fine-grained sediments.

The low permeability of fine-grained sediments makes the formation of gas hydrates in these sediments more challenging than that for coarse-grained sediments where the permeability is sufficiently large to allow the flow of water or gas through the specimen within meaningful time scales. A number of researchers formed hydrate-bearing specimens by mixing the soil with pre-formed hydrate granules. Li et al. (2010) mixed kaolin with pre-formed hydrate powder in a freezer before compacting the mixture at 10 MPa to make specimens. In this case the specimens were frozen to maintain hydrate stability.

An alternative approach to making hydrates in fine-grained sediments was taken by using THF as a hydrate former. THF is miscible with water and forms hydrate at 4°C at atmospheric pressure (Bathe et al., 1984; Gough & Davidson, 1971). By controlling the fraction of water and THF, hydrate-bearing soils specimens with a known hydrate saturation can be formed (Yun et al., 2007). Another advantage of THF is that THF has no gas phase, which simplifies the formation process of hydrate (Lee et al., 2007). Although THF hydrate is not a perfect analog for methane gas hydrate in nature due to the distinction from methane molecules in terms of size, polarization and other characteristics, as well as the difficulty in forming hydrate-bearing sediments of low hydrate saturation (Lee et al., 2008), it is suggested that the differences between THF and methane during hydrate formation are minor compared to the influence of formation history, laboratory techniques utilized and the distribution of hydrate in the pore space. (Lee et al., 2007).

Yun et al. (2007) and Lee et al. (2010) formed hydrate-bearing fine-grained specimens by mixing dry fine-grained sediments with selected THF-water solutions to form a saturated paste, which was then consolidated under constant effective stress. Rees et al. (2011) and Priest et al. (2014) have shown that hydrate in fine-grained sediments exhibit a grain displacing morphology that typically includes near vertical complex vein structures. However, both of the methods identified above created predominantly disseminated hydrate within the soil mixture, and therefore do not represent typical morphology observed in nature for fine-grained sediments. To overcome the difficulties associated with controlling hydrate vein growth in fine-grained sediments, Smith (2016) transferred a pre-formed cylindrical, standalone THF hydrate vein into a cylindrical void of a pre-consolidated fine-grained soil specimen. This method allows the control of hydrate vein size or hydrate saturation but the solid THF hydrate was observed to undergo slow dissolution when it came into contact with the pore water of the sediment.

2.4.2 Impact of hydrate on geomechanical behavior of sediments.

The presence of gas hydrate and its interaction with the sediment matrix will give rise to differences in geomechanical properties of marine gas hydrate-bearing sediments compared to non-hydrate bearing soils. The presence of hydrate enhances the strength and stiffness of the hydrate-bearing sediments and the magnitude of the increase will depend on which form of hydrate exists and in which sediment it forms. The subsequent dissociation of hydrate, through hydrate production methods or global warming, can significantly reduce the strength of the sediment. The loss of strength and stiffness is not only related to a loss of hydrate grains or veins within the sediment but also a reduction in effective stress due to the increased excess pore pressure induced by the free methane gas (Kwon et al., 2008). Therefore gas hydrate

dissociation can lead to significant reduction in strength, increasing deformation and the eventual failure of hydrate-bearing sediments (Kwon et al., 2010; Sultan et al., 2004). Understanding the impact of hydrate on the geomechanical behavior of hydrate-bearing sediments is therefore important for safety issues in gas hydrate production and geohazard assessment and prevention.

2.4.2.1 Previous research on coarse-grained sediments.

A number of distinct growth habits have been observed in coarse grained sediments where the hydrate can reside in the pores space and gave rise to minor interactions with the sediment (pore-filling), appear to mimic sediment grains and help carry imposed loads (load-bearing) or resided at particle contacts and cement sediment grains together (cementing). It was suggested that these growth habits were dependent on the hydrate formation method adopted (Priest et al., 2009) which gave rise to significant differences in behaviour of the sediment (Waite et al., 2009).

Generally, research conducted on hydrate-bearing coarse-grained sediments, including both natural samples and laboratory-formed specimens have shown that the shear strength and stiffness of coarse-grained sediments is related to a number of different factors, including hydrate saturation, density, strain rate, confining stress and hydrate morphology. The peak strength and stiffness of hydrate-bearing coarse-grained sediments increase with hydrate saturation as shown in Figure 2.6 (Ebimuma et al., 2005; Masui et al., 2005; Yun et al., 2007). Winters et al. (2004) tested coarse-grained samples recovered from the Mackenzie Delta, Northwest Territories and found the strength of hydrate-bearing samples was much higher than similar samples without hydrate. Results for the tests are shown in Figure 2.7 to illustrate the strength difference. Peak strength and stiffness of specimens also increases with increasing effective stress but the strength

behavior is dominated by hydrate properties rather than the effective stress at 100% hydrate saturation, as shown in Figure 2.8 and Figure 2.9. Hydrate distribution within the pore space also affects the behavior of coarse-grained soils. A pronounced increase in strength and stiffness of hydrate-bearing coarse-grained soil occurs when hydrate exhibits a cementing behavior. However, the behavior of hydrate-bearing coarse-grained soil might not be affected when hydrate is pore-filling, while load-bearing behavior of hydrate can have a pronounced effect on behavior when hydrate saturation exceeds 30% (Ebimuma et al., 2005; Masui et al., 2005).

2.4.2.2 Previous research on fine-grained sediments.

The geomechanical behavior of hydrate-bearing fine-grained sediments is not well understood due to the difficulty of sampling natural samples and replicating natural samples in the laboratory.

Yun et al. (2010) tested the strength of hydrate-bearing fine-grained sediments recovered from the Krishna-Godavari Basin offshore India with the instrumented pressure testing chamber (IPTC). They observed significant variation in undrained shear strength along the length of the cores and at different orthogonal planes around the core. The variations in undrained shear strength of the core samples were found to correlate with the presence of hydrate veins with significantly higher strengths recorded where hydrate were present relative to that for sediments without hydrates. In addition, the shear strengths of the sediment without hydrate being present were appreciably lower than that expected for normally consolidated sediments at the depths they were recovered. Subsequent shore based tests highlighted the high in-situ water content of the sediments from the Krishna-Godavari Basin along with very low undrained shear strength

when tested at these high water contents (Priest et al., 2014). It was therefore surmised that the strength of hydrate-bearing sediments within the Krishna-Godavri basin was increased by the presence of hydrate veins, which inhibited normal consolidation and helped to support the overburden stress applied on the sediments.

Li et al. (2011, 2012) studied the strength behavior of hydrate-bearing fine-grained soils by mixing kaolin clay with pre-formed hydrate powder and concluded that the deviatoric stress of the specimen increased with increase in confining stress and reduction in temperature. Yun et al. (2007) carried out undrained triaxial tests on THF-hydrate-bearing fine-grained specimens formed by mixing dry soil with a THF-water solution. The results are shown in Figure 2.10 and Figure 2.11. Peak strength and stiffness increase nonlinearly with hydrate saturation, but become stress-independent at a 100% hydrate saturation. However, disseminated hydrates were formed in these tests that didn't mimic the natural morphology of hydrate in fine-grained sediments as vein or fracture structure (Rees at al., 2011).

To better quantify the influence of hydrate veins on sediment behavior, Smith (2016) carried out unconsolidated-undrained triaxial tests on fine-grained soil specimen containing a cylindrical THF hydrate vein and concluded that the undrained shear strength and stiffness of the specimen increased with hydrate saturation or hydrate vein size, as shown in Figure 2.12. The results led to the relationships suggesting that a 'threshold' vein size existed where undrained strength and stiffness were entirely controlled by the soil below the threshold and hydrate-controlled above the threshold. However, due to the slow dissolution of THF hydrate when in contact with the sediment pore water only UU tests were carried out. Therefore the impact of effective stress still

remains unknown and the influence of the hydrate veins at low concentrations may have been underestimated.

2.5 Summary

Gas hydrates are ice-like solid compound formed at low temperature and high pressure condition. Methane is the most common gas to form gas hydrate. Methane gas hydrates are mostly found below the permafrost or within deep-water marine sediments. Attention has been focused on gas hydrate due to its potential as an energy source, its potential role in global warming and its potential as a potential geotechnical hazard.

Gas hydrates are found within coarse-grained and fine-grained sediments when hydrate stability conditions are present. However, the morphology of gas hydrate in coarse-grained and fine-grained sediments is different. Hydrates are commonly observed disseminated homogeneously within the pore space of coarse-grained sediments, and heterogeneously distributed in fine-grained sediments as complex structures such as nodules, veins and fractures and lenses. The morphology and distribution habit of hydrate have a significant effect on the geomechanical behavior of hydrate-bearing sediments.

The presence of hydrate enhances the strength and stiffness of the hydrate-bearing sediment and the subsequent dissociation of hydrate can significantly reduce the strength of the sediment. Therefore, understanding the impact of hydrate on the geomechanical behavior of hydrate-bearing sediments is important. The geomechanical behavior of hydrate-bearing coarse-grained

sediments is well understood so this research focuses on that of hydrate-bearing fine-grained sediments, which is not well understood due to the difficulty of sampling natural samples.

Smith (2016) observed an increase in peak strength and stiffness of hydrate-bearing fine-grained specimens with increasing hydrate saturation by conducting shear tests on specimens formed by THF hydrate formation method. Only unconsolidated-undrained triaxial tests were carried out by Smith (2016) on fine-grained soil specimens. It was concluded that the undrained shear strength and stiffness of the specimen increased with hydrate saturation. However, significant hydrate dissolution was encountered that may have affected the results and conclusions of his research, also the influence of effective stress on the geomechanical behavior of hydrate-bearing fine-grained sediments was not investigated. Thus, in this research consolidated-undrained (CU) tests will be carried out on specimens to investigate geomechanical behavior of hydrate-bearing fine-grained soil sediments, and the influence of effective stress.

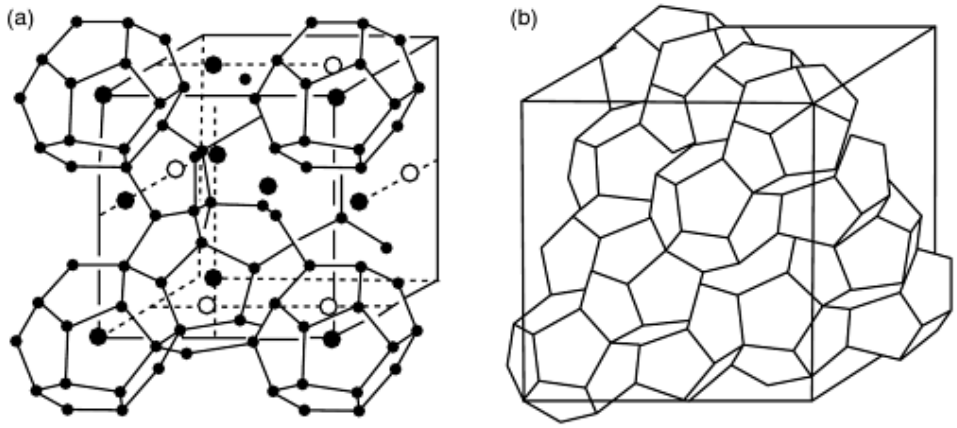

Figure 2.1: (a) Structure I and (b) Structure II for gas hydrate (Sloan & Koh, 2007).

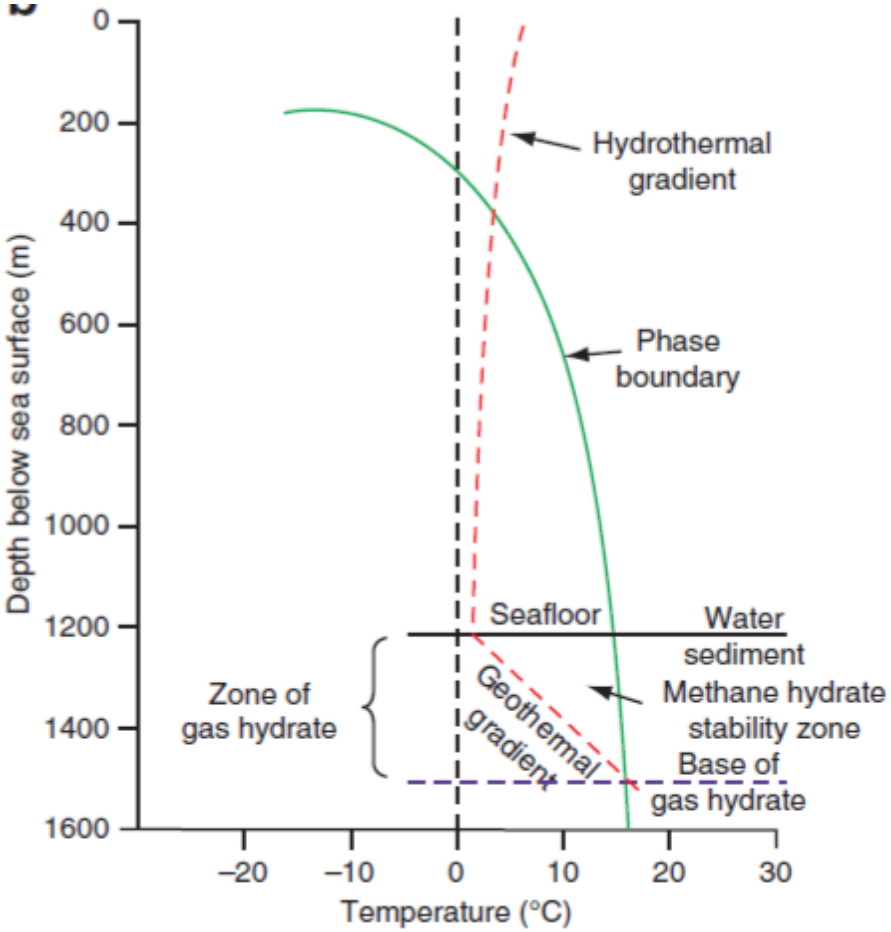

Figure 2.2: Hydrate stability zone in marine environment (Sloan & Koh, 2007).

Figure 2.3: (a) Thin, high angle gas hydrate veins from Krishna-Godavari Basin; (b) Partially dissociated core from Krishna-Godavari Basin; (c) Massive gas hydrate nodule from Krishna-Godavari Basin; (d) Gas hydrate layer and nodule from Gulf of Mexico; (e) Hydrate-bearing sandstone from Mount Elbert; (f) Gas hydrate in gravel from Mallik, Canada permafrost-hosted deposits (Winters, 2011).

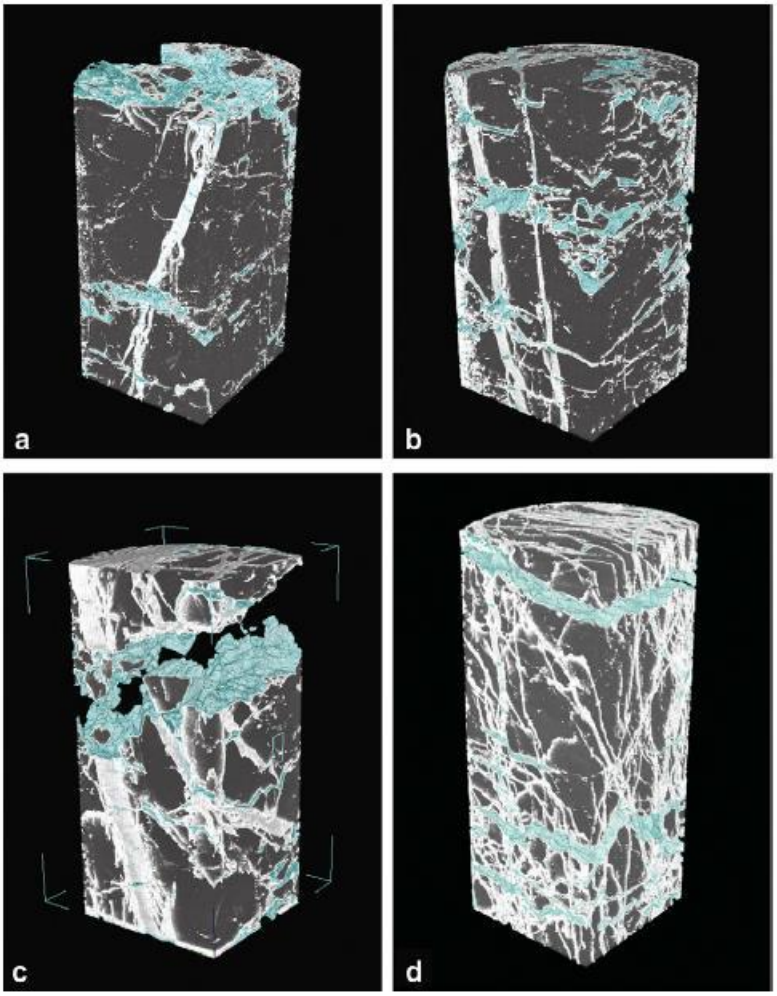

Figure 2.4: X-ray CT images of samples from the Krishna-Godavari Basin showing pervasive hydrate veins forking and branching (white) and ice (blue) (Rees et al., 2011).

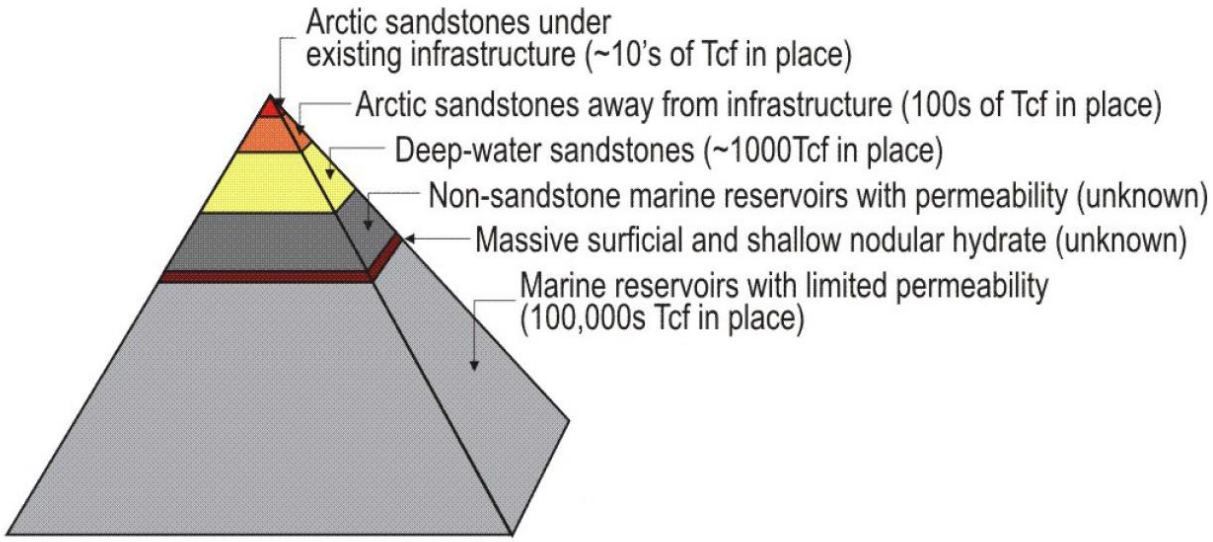

Figure 2.5: Gas hydrate resource pyramid (Boswell & Collett, 2006).

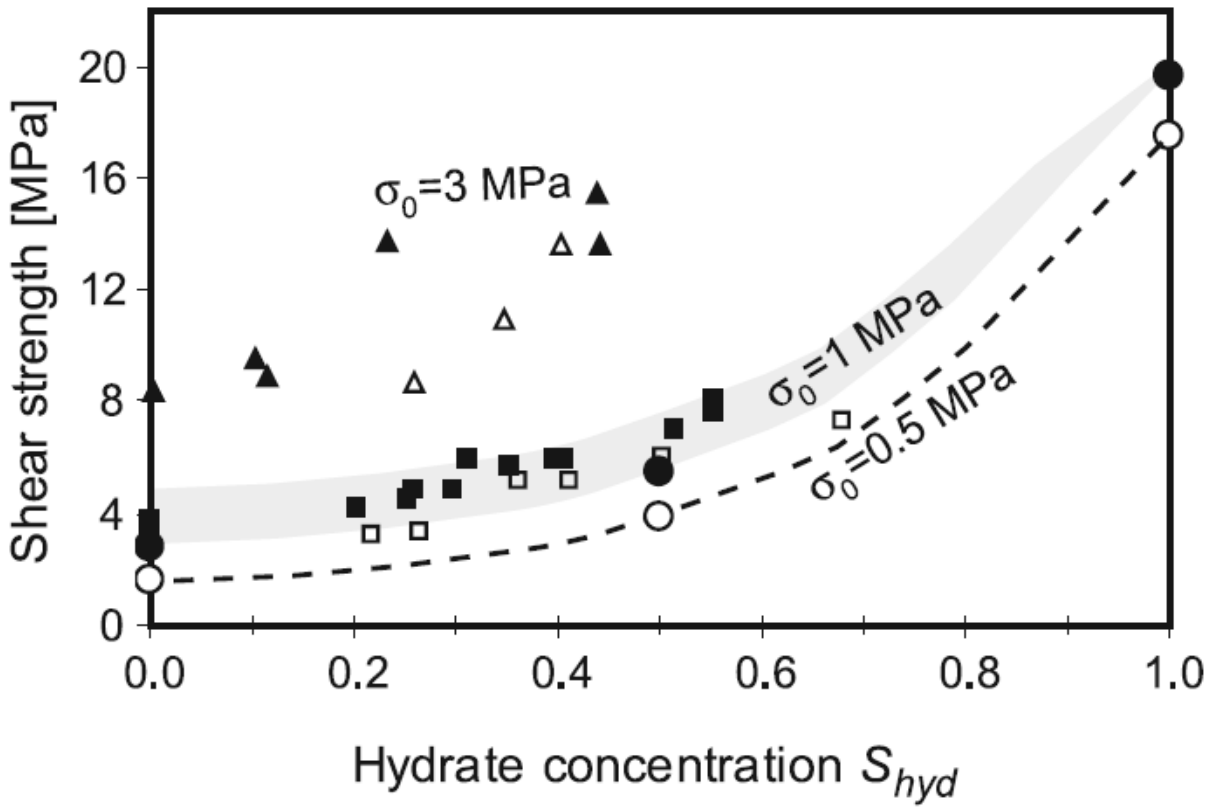

Figure 2.6: Shear strength as a function of hydrate concentration for three effective confining stress (0.5,1 and 3 MPa). The methane hydrate results for σ_0' = 1 MPa are from Masui et al. (2005), and the results for σ_0' = 3 MPa are from Ebinuma et al. (2005). Solid triangles and squares denote sand mixtures with methane hydrate formed by gas percolation, and open triangles and squares represent methane hydrate formed from ice seeds. Filled circles show the sand-THF hydrate data from Yun et al. (2007) at 1 MPa (solid) and at 0.5 MPa (open circles) (Yun et al., 2007).

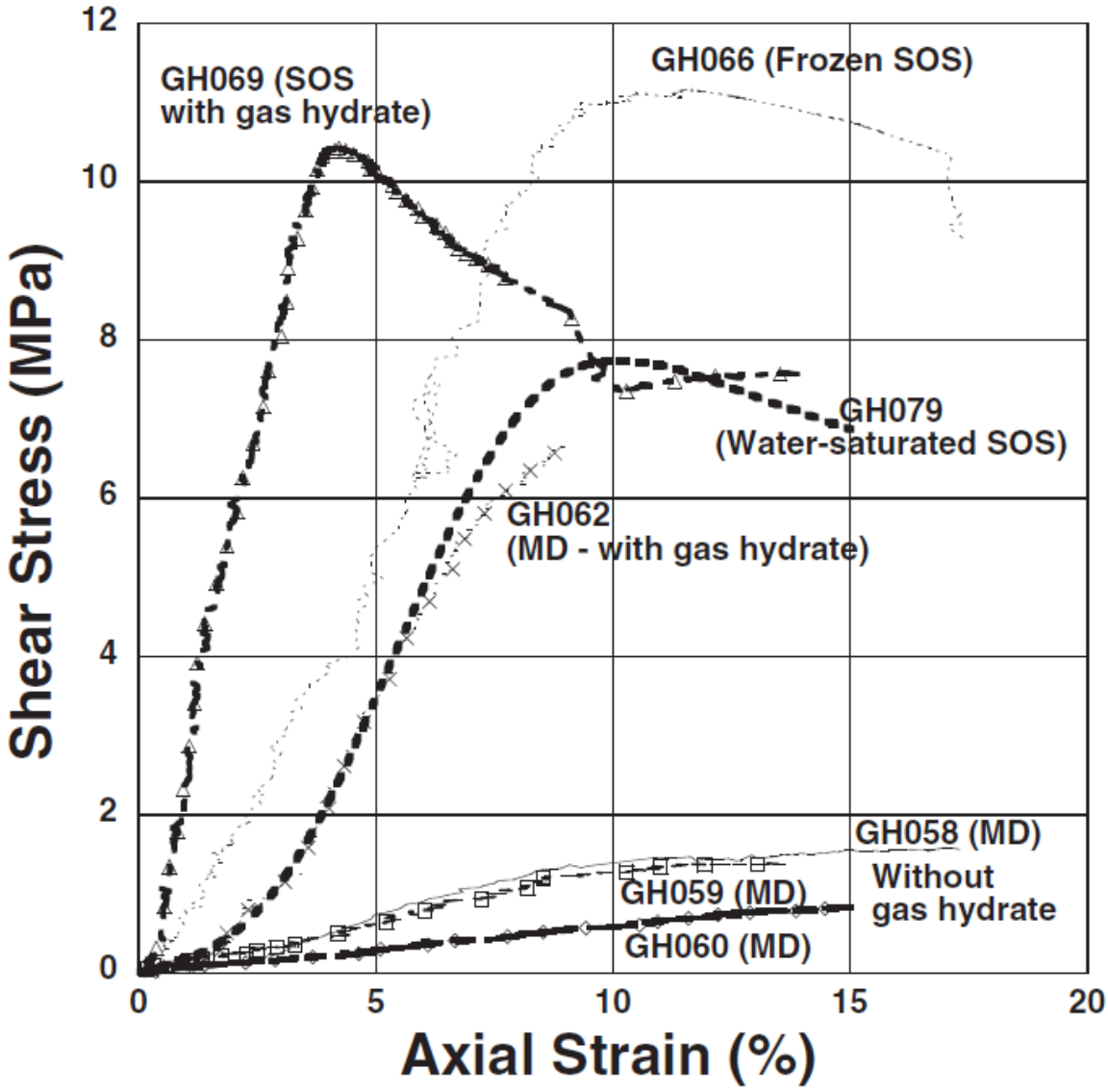

Figure 2.7: Stress-strain plots for sieved Ottawa sand (SOS) and Mackenzie Delta 2L-38 (MD) samples containing pore-fillings (Winters et al., 2004).

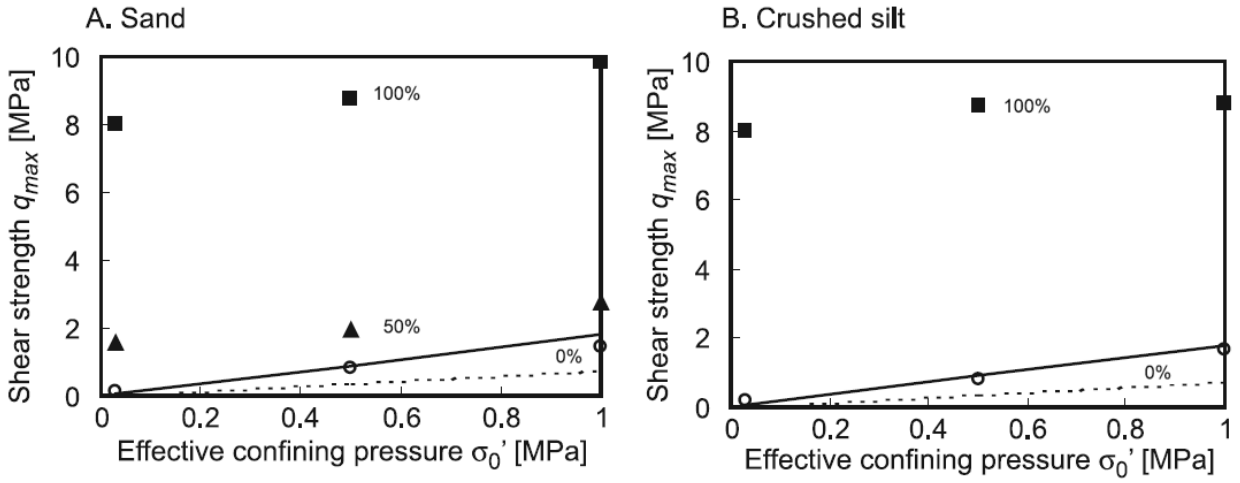

Figure 2.8: Shear strength of coarse-grained sediments as a function of effective confining pressure (Yun et al., 2007)

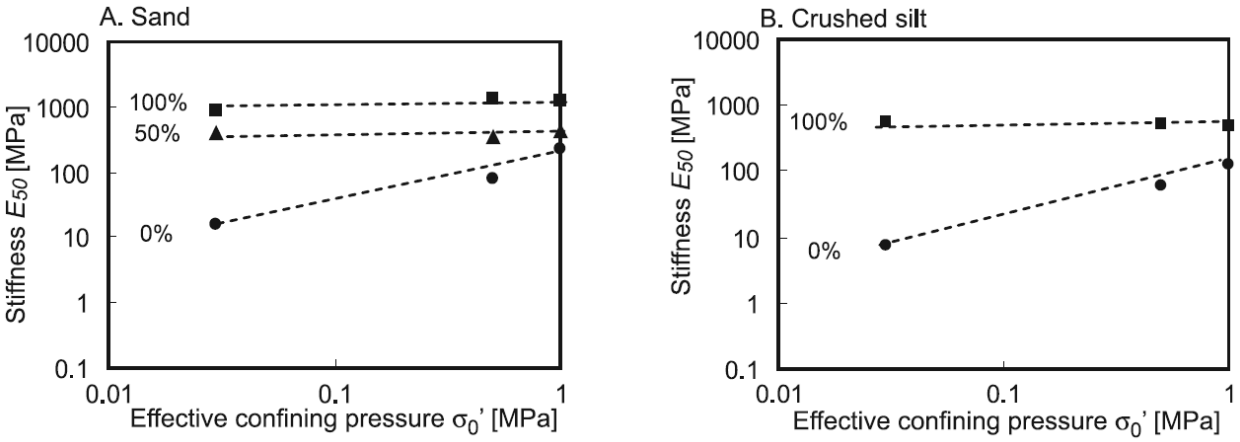

Figure 2.9: Stiffness of coarse-grained sediments as a function of effective confining pressure (Yun et al., 2007).

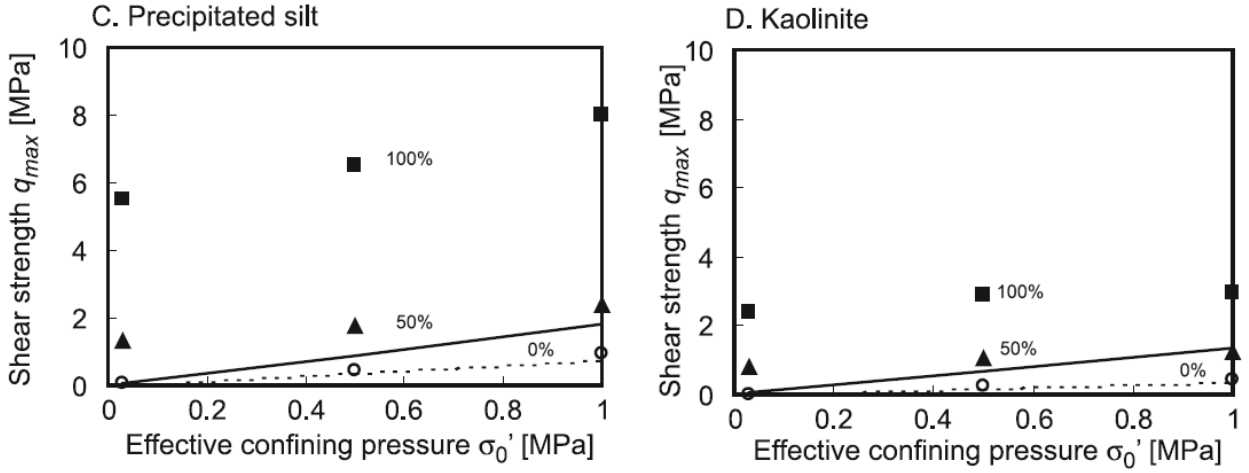

Figure 2.10: Shear strength of fine-grained sediments as a function of effective confining pressure (Yun et al., 2007).

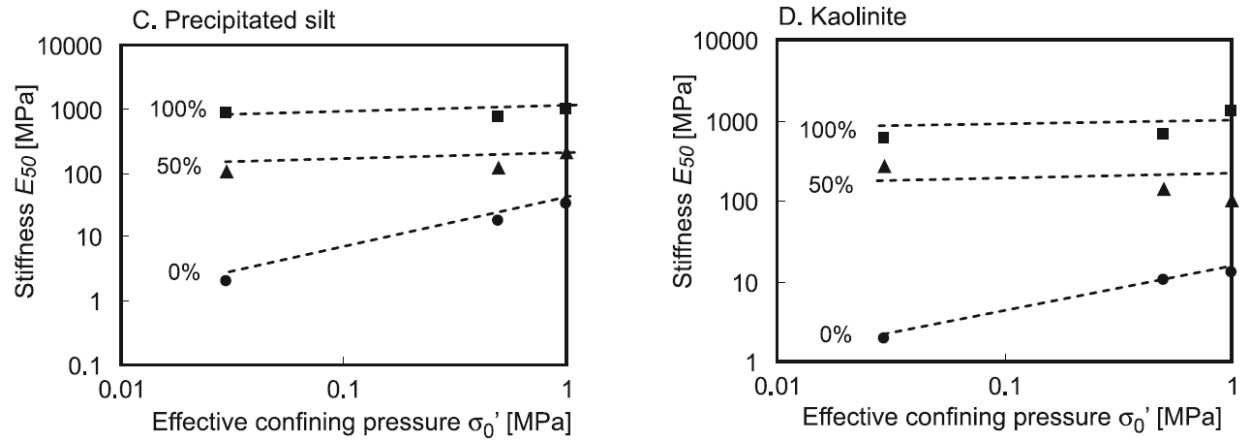

Figure 2.11: Stiffness of fine-grained sediments as a function of effective confining pressure (Yun et al., 2007).

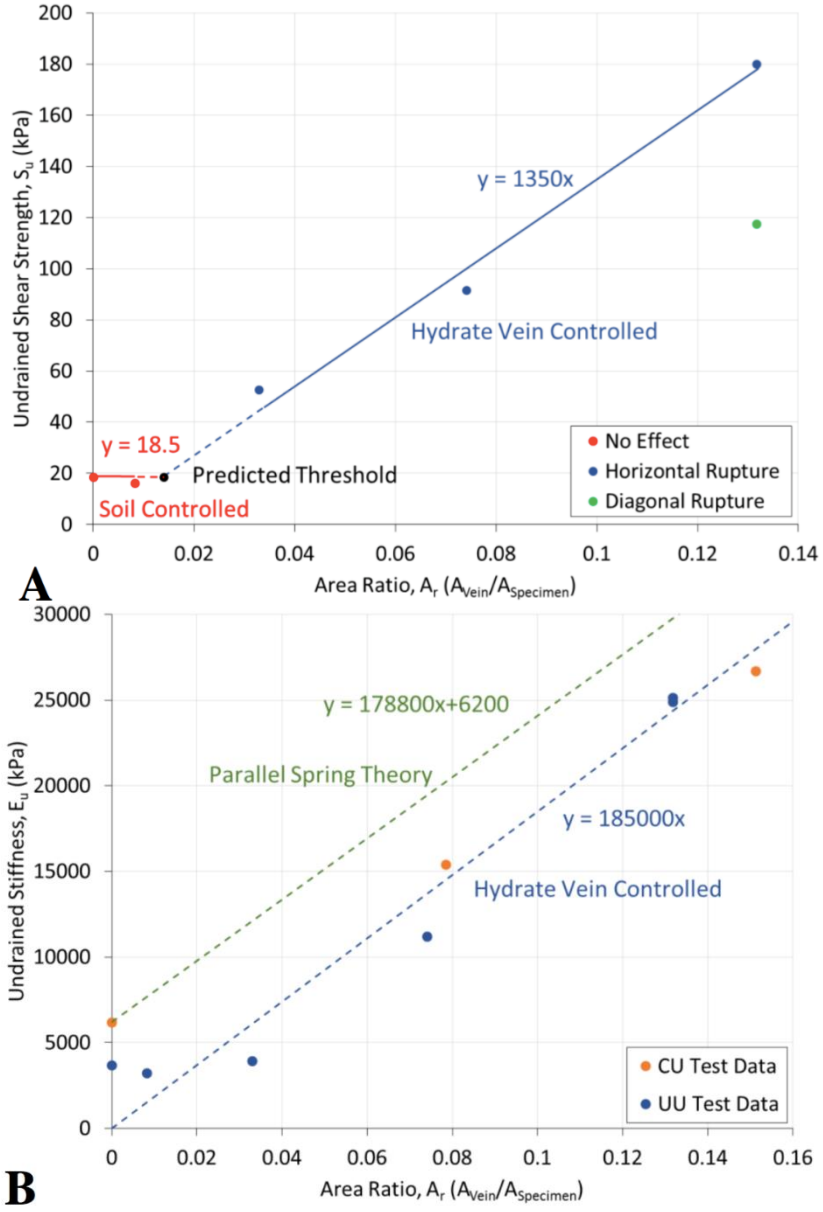

Figure 2.12: Comparison of (a) undrained shear strength and (b) undrained stiffness vs. hydrate vein area ratio, showing both undrained shear strength and undrained stiffness increase with hydrate saturation or hydrate vein area ratio (Smith, 2016).

Chapter Three: Experimental Procedure

3.1 Introduction

The presence of hydrate veins in fine-grained sediments may pose a significant geohazard in terms of slope instability since the strength of the hydrate veins may influence the behaviour of the sediment, which can be significantly weakened upon dissociation. This chapter therefore details the experimental test program that was adopted and carried out to help investigate the influence of hydrate veins on the geomechanical behaviour of fine-grained soils. The methodology that was developed and utilized to form fine-grained soil specimens, cylindrical THF veins and finally hydrate-bearing fine-grained soil specimens is highlighted. A laboratory apparatus, the triaxial test apparatus, and the testing protocols used to investigate the behaviour of THF hydrate veins and the geomechanical behavior of fine-grained soil specimens containing these veins is presented.

3.2 Specimen Preparation

3.2.1 Soil preparation.

Typically hydrate veins occur in fine-grained soil therefore soil specimens were formed to replicate a typical marine fine-grained sediment. A soil mixture by weight of 35% Kaolin Clay and 65% Sil Industrial Mineral Flour 325 mesh silica silt was chosen as the experimental soil to be consistent with former research done by Smith (2016). The grain size distribution of the chosen soil, and its comparison with typical marine sediments in which gas hydrate occur is illustrated in Figure 3.1.

A soil slurry was initially prepared by mixing a known mass of dry clay and silt particles with sufficient water to give a water content of 0.55. This slurry was transferred into a bucket and sealed, as shown in Figure 3.2, so that a vacuum could be applied to de-air the soil mixture. The de-aired slurry was then poured into a consolidation cell with porous metal discs located at the top and bottom thus allowing for free double drainage of pore water during consolidation. A ram attached to the top plate, housing the porous disc was used to apply a vertical stress of 100 KPa. Filter papers were placed between the cylindrical soil specimen and both the top and bottom porous metal discs to avoid soil migration, which might block the pores of the porous metal discs and delay the pore water drainage and consolidation. The consolidation cell and loading ram are shown in Figure 3.3.

Cylindrical soil specimens were formed after consolidation by inserting a 70 mm internal diameter extrusion tube (Figure 3.4) into the consolidated soil, which was subsequently removed and the soil specimen extruded and trimmed to a length of 140 mm.

3.2.2 Hydrate veins formation.

Tetrahydrofuran (THF) (C_4H_8O) was used to form hydrate veins due to its advantages as a proxy for methane hydrate as highlighted by previous laboratory studies outlined in Chapter 2. To investigate the behavior of THF hydrate veins, standalone cylindrical hydrate veins of 6.35 mm (0.25”), 12.7 mm (0.5”), 19.05 mm (0.75”) and 25.4 mm (1”) diameter and 140 mm high were formed using THF and water. Vertical, cylindrical, synthetic, standalone THF-hydrate veins of different sizes were used to simplify the complex morphology of natural hydrate in fine-grained sediments.

The molar ratio for 100% hydrate formation is typically considered to be 1:17 of THF and water, respectively. However, the evaporation of THF during hydrate formation can lead to excess water within the solution and incomplete formation of the hydrate (Zeng et al., 2006). Therefore, a 1:15 molar ratio was used that ensured complete formation of 100% THF hydrate veins (Smith, 2016). The hydrate veins were formed by initially mixing THF with de-aired water with a molar ratio of 1:15. This solution was then poured into preformed molds for the individual cylindrical veins. These molds (Figure 3.5) were made by wrapping aluminum foil around a former of the required diameter with vacuum grease between the foil sheets to prevent leakage of the THF-water mixture. The former was subsequently removed and THF/water solution poured into the molds. The molds were then transferred into a freezer at -20 °C to initiate hydrate formation. A piece of foil was placed on the top of the mold to help prevent evaporation of the THF during hydrate formation. The formed THF hydrate veins are shown in Figure 3.6 (except the 0.25" cylinder).

3.2.3 Hydrate-bearing specimen formation.

Hydrate-bearing specimens were formed by placing the formed THF veins within preformed vein voids within the center of the fine-grained soil specimens (Section 3.2.1). The vein voids were created by drilling a continuous cylindrical and vertical hole through the soil specimen with wood augers of different sizes (0.25", 0.5", 0.75" and 1"), highlighted in Figure 3.7. After drilling the holes the soil was placed back into the refrigerator to cool the specimen back down to 2°C, which was within the hydrate stability zone.

Extensive testing done by Smith (2016) had shown that the THF hydrate veins would rapidly dissociate once the THF hydrate was outside its hydrate stability point (temperature above 4.13°C at atmospheric pressure). In addition, when the hydrate was in contact with water the THF hydrate would undergo slow dissolution due to the THF concentration gradient between the THF hydrate and free water. As CU tests of hydrate-bearing specimens would take several days to complete, this may lead to THF dissolution, as the THF would have been in contact with the pore water of the soil specimens. To limit this potential, the hydrate vein specimens were wrapped in a thin plastic wrap membrane to avoid direct contact between the THF hydrate and water before being inserted in the vein voids. For the 0.25”-diameter vein testing was conducted within the aluminum mold since fracturing of this vein occurred when trying to remove the aluminum foil after hydrate formation. The THF hydrate cylinders with the plastic film wrap for the 0.5”, 0.75” and 1”-diameter are shown in Figure 3.8 with Figure 3.9 showing the soil specimens with the hydrate vein inserted in the center of the specimen.

3.3 Testing apparatus

A computer controlled low-temperature triaxial system was used for testing individual THF hydrate veins as well as the hydrate-bearing soil specimens, as shown in Figure 3.10 and illustrated schematically in Figure 3.11. The apparatus featured a 25kN load frame with external load cell (0.05% precision) connected to a ram that applied a vertical load to the specimens (whether THF veins or soil). The apparatus cell walls were made of clear acrylic that allowed clear visual observation of the mode of failure of the THF veins or soil specimens during a test. Two servo-controlled hydraulic pumps allowed confining cell and pore pressures of up to 2 MPa to be applied to the specimen within the cell with an accuracy of ±1 kPa. Cell pressure and pore

water pressure were measured independently by a pressure transducer with ±0.1 kPa resolution. Axial displacement of the specimen was measured by an external LVDT mounted on the load ram.

The triaxial system was modified to enable testing at temperatures required for THF hydrate stability (<4°C). This was achieved using two refrigerated circulators that were used to pump coolant fluids through copper tubes submerged in the cell water and mounted in an aluminum plate housed beneath the triaxial base plate. The base plate pedestal was pre-cooled to 1 °C to avoid hydrate dissociation due to the direct contact between the bottom of hydrate and the base plate pedestal. The triaxial cell was covered with an insulation jacket to minimize heat transfer between the cell and the ambient room temperature. The temperature of the cell was maintained at around 1°C and was monitored throughout the test by a thermocouple placed inside the cell.

3.4 Specimen mounting and cell assembly

3.4.1 Compression testing of THF vein specimens.

Compression tests on THF hydrate veins were performed in the triaxial cell. In these tests THF veins were centrally located on the chilled cell base pedestal with the axial load piston lowered onto the top of the THF vein. To ensure that the hydrate vein was maintained within its hydrate stability field during cell assembly and subsequent compression testing crushed ice was placed around the hydrate vein until the cell was assembled and filled with chilled water. THF veins were tested while wrapped in the plastic membrane as identified in Section 3.2.3.

3.4.2 Compression testing of hydrate-bearing soil specimens.

Prior to mounting the soil specimen all the drainage lines to the cell, porous discs, base pedestal and top cap and filter papers were saturated with deaired water, following ASTM Standard D4767. Radial filter drains were wrapped around the specimen with filter papers placed on the top and bottom of the specimen. The specimen was then mounted on the chilled base pedestal and top cap placed on the top. Crushed ice was placed around the soil specimen to maintain specimen temperature. The cell was placed around the specimen and proper seating and alignment of the piston with the top cap was ensured by bringing the axial load piston into contact with the top cap. The cell was then filled with deaired chilled water and sealed with vacuum grease to avoid any leaks.

During specimen mounting and cell assembly, the hydrate-bearing specimen was only exposed to room temperatures for around 10 minutes. Observation of specimen after the test suggested that the thermal conductivity of the chilled soil specimen was sufficiently low so as to prevent hydrate dissociation during set-up.

3.5 Experimental test procedure

3.5.1 Compression testing on standalone synthetic hydrate cylindrical veins.

The detailed characterization of cylindrical hydrate veins was required to better understand the geomechanical behaviour of fine-grained specimens containing cylindrical hydrate veins. Therefore, compression tests were conducted to investigate the stress-strain behaviour of the standalone synthetic cylindrical THF hydrate veins.

Axial compression tests were carried out on 6.35 mm (0.25”), 12.7 mm (0.5”), 19.05 mm (0.75”) and 25.4 mm (1”) diameter by 140 mm high cylindrical hydrate veins. Tests were conducted under strain control with axial load and axial displacement measured with time throughout the test. A number of different strain rates were considered, which were selected as 0.05, 0.3 and 0.5%/min. These strain rates were chosen to consider the range of strain rates that had been applied during CU and UU tests on hydrate-bearing fine-grained soil specimens (Smith, 2016). In those tests a strain rate of 0.05%/min was applied during CU tests, while a strain rate of 0.3%/min was applied during UU tests. The additional strain rate of 0.5%/min was to provide additional range to investigate the impact of strain rates on the behavior of hydrate veins.

3.5.2 CU testing on soil specimens with and without hydrate.

Consolidated-Undrained (CU) triaxial tests were first conducted on fine-grained soil specimens without hydrate to study the geomechanical behaviour of fine-grained soil and provide base-line values for comparison with the geomechanical behaviour of hydrate-bearing fine-grained specimens. The CU test is used to determine the strength and stress-strain behaviour of a cylindrical cohesive soil specimen. Both cell confining pressure and back pressure were raised to achieve specimen saturation before proceeding the consolidation stage. In the CU tests the specimens are initially isotopically consolidated to a defined confining stress with open drainage and consequently sheared in axial compression at a constant rate of axial deformation with drainage of the specimen prevented. The consolidation phase allows cell pressure and back pore pressure to be applied to the soil specimen to mimic the in-situ stress conditions on the natural sediments at certain depth.

In our CU tests all-around effective stress (cell pressure-back pressure) was first applied to the specimen to consolidate the specimen. Consolidation occurred overnight and was deemed to have finished when any excess pore pressure generated during the application of effective stress is fully dissipated (less 5% of initial excess) and no continuing axial displacement is observed. Saturates filter paper drains were placed in position around the specimen to accelerate the consolidation process. Back pressure was applied to the pore water during the consolidation of the soil specimen so that any air remaining may be dissolved. CU tests were conducted at three different effective stress conditions (100, 200 and 400 kPa). Once specimens were consolidated the specimen was sheared (undrained) at a constant shear rate of a 0.05%/min.

3.6 Test parameters

Automated recording of test data was undertaken throughout the tests. The values measured in the triaxial tests include cell pressure, σ_3, pore water pressure, u, the ram load, Q, and axial displacement of the sample, ΔH (measured by the ram displacement). From these measurements the various test parameters that can define soil behaviour can be calculated and highlighted below.

3.6.1 Stress-strain behavior.

3.6.1.1 Deviatoric stress.

Stress applied to the soil can be calculated from the load applied to the ram, which was measured by a force sensor mounted between the ram and the 25kN load frame, and the area of the specimen as follows:

$$q = Q/A_{specimen} \quad (3.1)$$

where,

q = deviatoric stress applied on the specimen, kPa, Q = ram load applied to the specimen, kN, and $A_{specimen}$ = cross-sectional area of the specimen, m^2

3.6.1.2 Axial strain.

Axial displacement of the specimen was measured by an external LVDT mounted on the load ram and axial strain, ε_a of the specimen was calculated as follows:

$$\varepsilon_a = \Delta H/H_0 \quad (3.2)$$

where,

ΔH = change in specimen height during loading as measured by the movement of the ram, mm, and H_0 = height of specimen after consolidation, mm

From the stress and strain values calculated above the stress applied on the specimens can then be plotted against the axial strain during shearing of the specimen to have a better understanding of the stress-strain behavior of the specimens.

3.6.1.3 Undrained shear strength.

Shear strength is used to describe the magnitude of the shear stress that a material can sustain. Undrained shear strength of the soil is an important parameter for evaluating soil stability. The undrained shear strength (S_u) of all the specimens is defined as half of the deviatoric stress when the specimen reaches the critical state (q_{cs}), as illustrated in the equation:

$$S_u = \frac{q_{cs}}{2} \quad (3.3)$$

where,

q_{cs} = deviatoric stress applied on the specimen at critical state

3.6.1.4 Stiffness.

The stiffness of a material is its resistance to deformation. The secant modulus, E_{50}, which is determined at half of the deviatoric stress at critical state drawn through the origin of the stress-strain curve. The stiffness of the specimen is calculated as follows:

$$E_{50} = \frac{q_{cs}/2}{\varepsilon_{cs}} \tag{3.4}$$

where,

q_{cs} = deviatoric stress applied on the specimen at critical state

ε_{cs} = axial strain corresponding to deviatoric stress at critical state

3.6.2 Pore pressure response.

The strength and stiffness characteristics of soil are best understood by visualizing it as a skeleton of solid particles with voids filled with water in saturated soil. Only the skeleton of the solid particles and not the water can carry shear stress. The normal stress on any plane is the sum of the two stress components, namely the stress carried by the solid particles and the pore pressure of the fluid in the void space. Therefore, the pore pressure response is important for understanding the strength and stiffness behavior of soil. Pore pressure was measured by a transducer connected to the base cap. Excess pore pressure and pore pressure coefficient (A)

were plot against axial strain to illustrate the pore pressure change during shear, and they are calculated as follows:

$$u_{excess} = u - u_o \tag{3.5}$$

where,

u_{excess} = excess pore pressure, kPa, and

u = pore pressure measured by pressure sensor, kPa, and

u_0 = initial pore pressure measured by pressure sensor, kPa

$$A = (u-u_0)/(\sigma_1-\sigma_3) \tag{3.6}$$

Where,

σ_1 = Axial stress, kPa, and

σ_3 = cell pressure, kPa

Example plots of excess pore pressure and pore pressure coefficient (a) versus axial strain are shown in Figure 3.12(a) and (b), respectively.

3.6.3 Strength criteria.

The purpose of understanding the shear strength of the hydrate-free and hydrate-bearing sediments is to predict or estimate the failure of these materials. The Mohr-Coulomb failure criterion is one method for determining the strength of the soil in relation to the friction angle and normal effective stress on the failure plane of the soil.

The strength criterion can be described by the following equation:

$$\tau = c' + \sigma' \tan\phi' \quad (3.7)$$

where,

τ is the shear stress;

c', the cohesion, which is the tensile stress of the soil at no effective stress;

σ', the effective normal stress;

ϕ', the angle of internal friction in terms of σ'

The Mohr-Coulomb failure can be determined by plotting the Mohr circles of stress (τ vs σ') from a series of tests on specimens at different stress conditions. As the Mohr-Coulomb is a limiting stress condition the stresses in the soil cannot lie above the Mohr-Coulomb failure line as described by Equation 4.1. To draw the Mohr circles of stress the maximum (σ'_1) and minimum (σ'_3) principal effective stress (see section 3.6.2) at failure are derived from each test and plotted. The Mohr coulomb failure line is then defined by fitting a tangent line through the Mohr circles for each test. An example plot presenting the strength criteria of the soil specimens is shown in Figure 3.13.

3.6.4 q-p' stress behavior.

A stress path is a plot of a theoretical or experimental relationship between two stress parameters. In the undrained shear tests where pore pressure is measured the stress path can be defined in relation to total stress or effective stress. Roscoe et al. (1958) stated that deviatoric stress, q, and the effective mean normal stress, p', are related in the region that is between the

normally consolidated state and critical state of the soil. In a triaxial test in which the orthogonal horizontal stresses are the same, $\sigma_2 = \sigma_3$, then the stress parameters are defined as follows:

$$q = \sigma_1' - \sigma_3' \tag{3.8}$$

$$p' = (\sigma_1' + 2\sigma_3')/3 \tag{3.9}$$

where,

σ_1' = effective axial stress ($\sigma_1 - u$), kPa, and

σ_3' = effective cell pressure ($\sigma_3 - u$), kPa

An example plot of the stress path followed by a soil in a triaxial test for a normally consolidated fine-grained soil in q-p' space is shown in Figure 3.14.

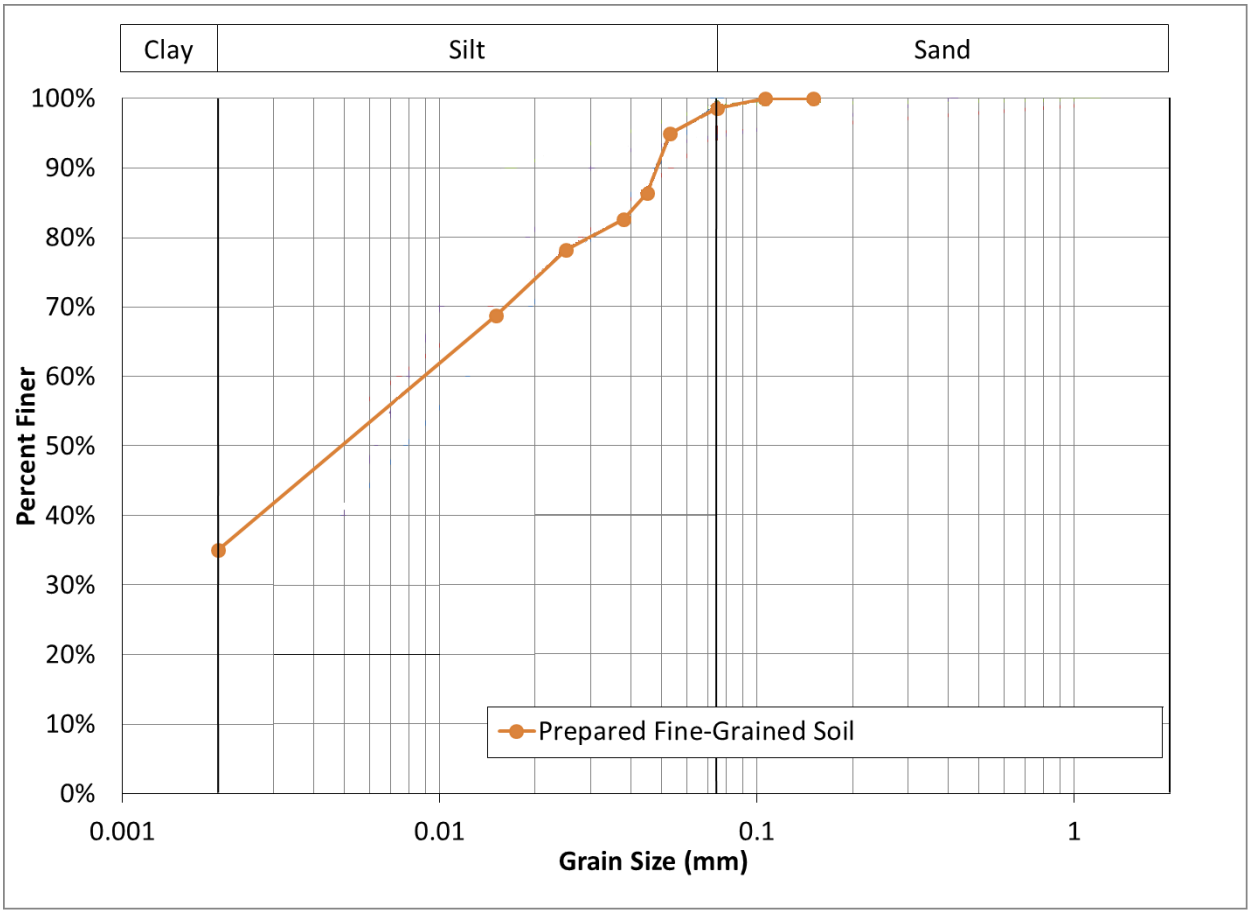

Figure 3.1: Grain size distribution curve for the prepared fine-grained soil (Smith, 2016).

Figure 3.2: Sealed bucket that is able to be applied vacuum used to deair the slurry.

Figure 3.3: Specially designed and constructed consolidation cell with aluminum top plate built with a ram which can be connected to the load frame.

Figure 3.4: Extrusion tube of 70mm diameter used to extrude the fine-grained soil specimens.

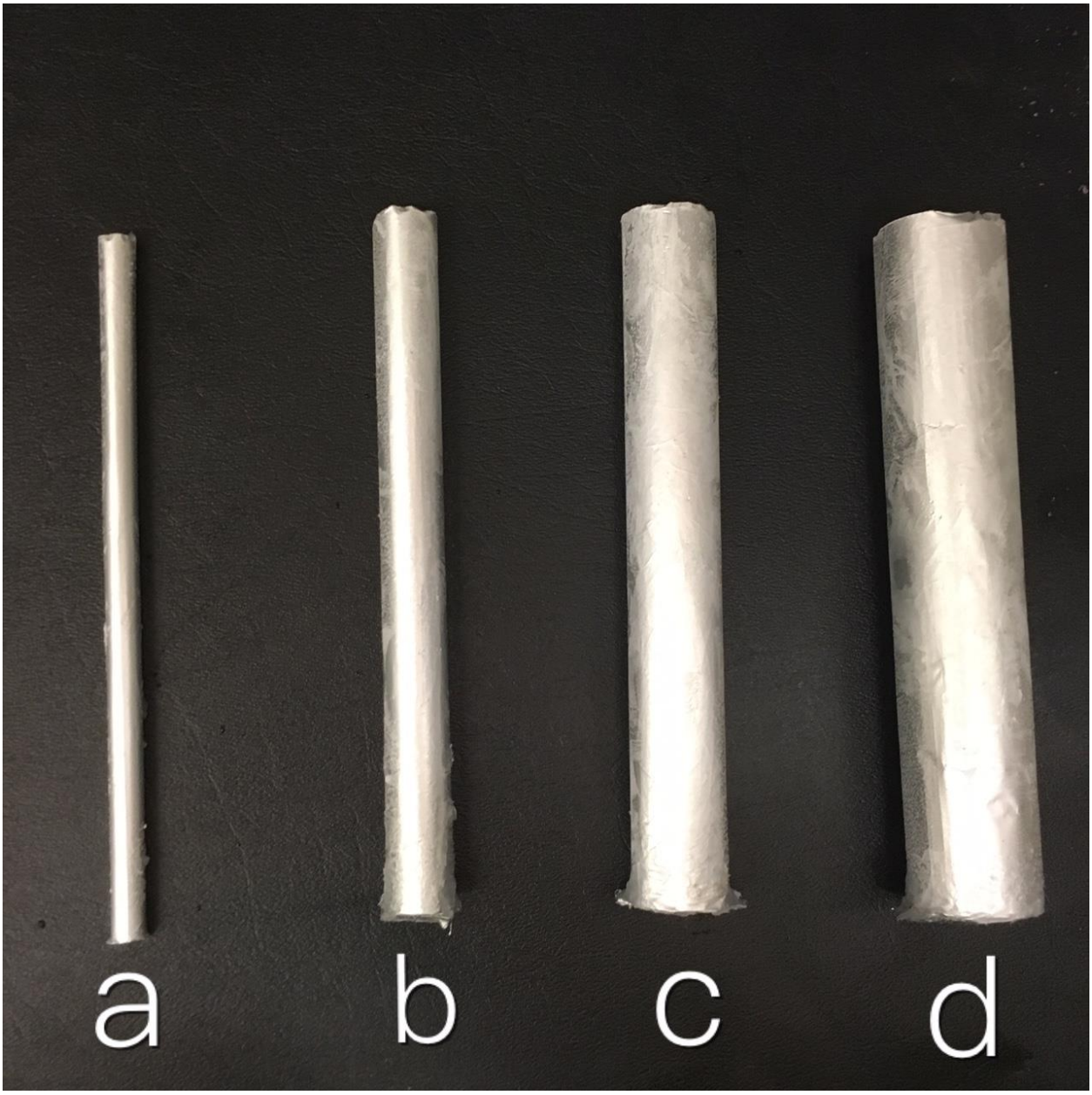

Figure 3.5: Formed (a) 0.25”, (b) 0.5”, (c) 0.75” and (d) 1”-diameter hydrate cylindrical veins within the aluminum foil molds.

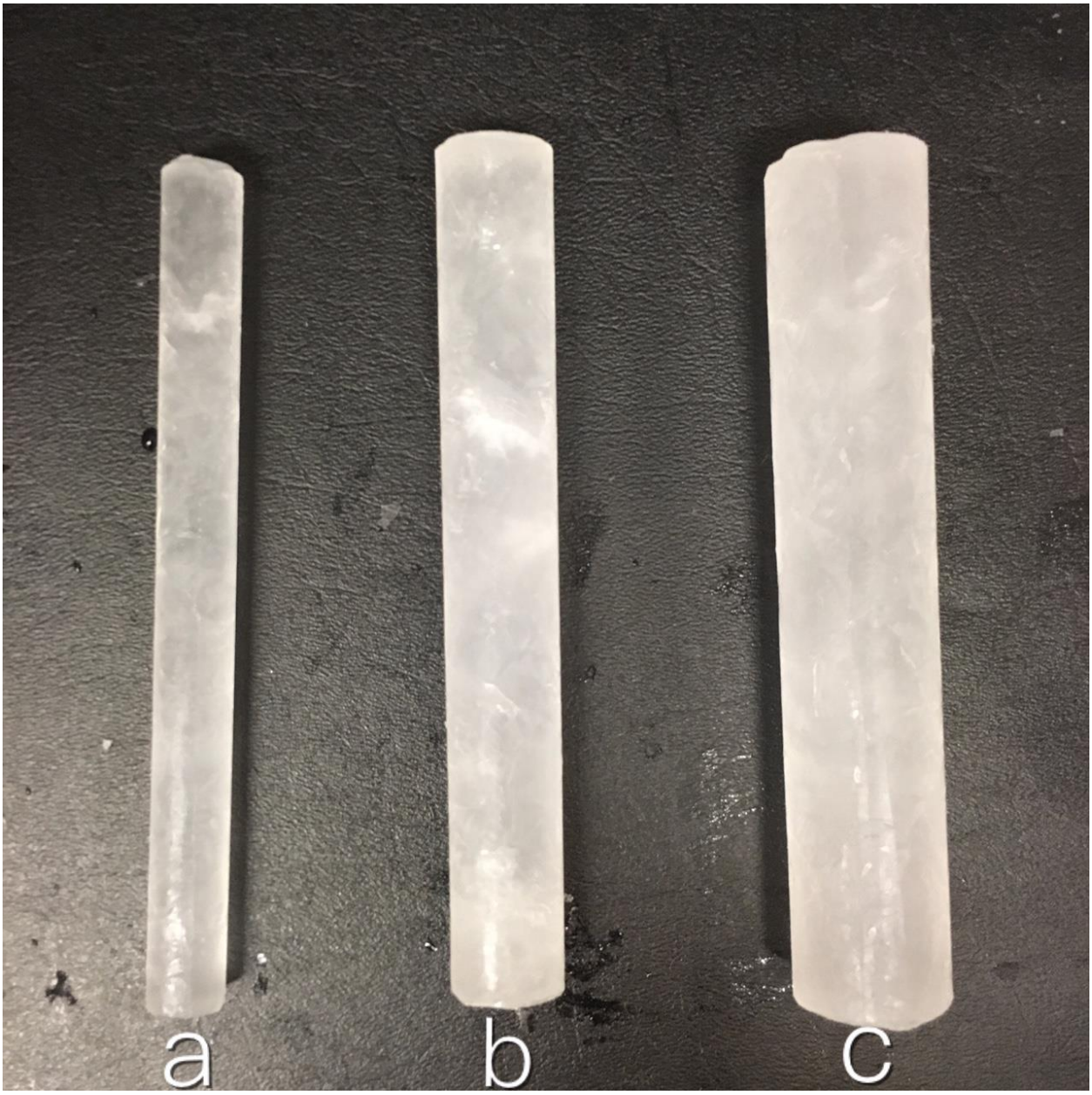

Figure 3.6: Formed (a) 0.5”, (b) 0.75” and (c) 1”-diameter hydrate cylindrical veins unwrapped from the aluminum foil molds.

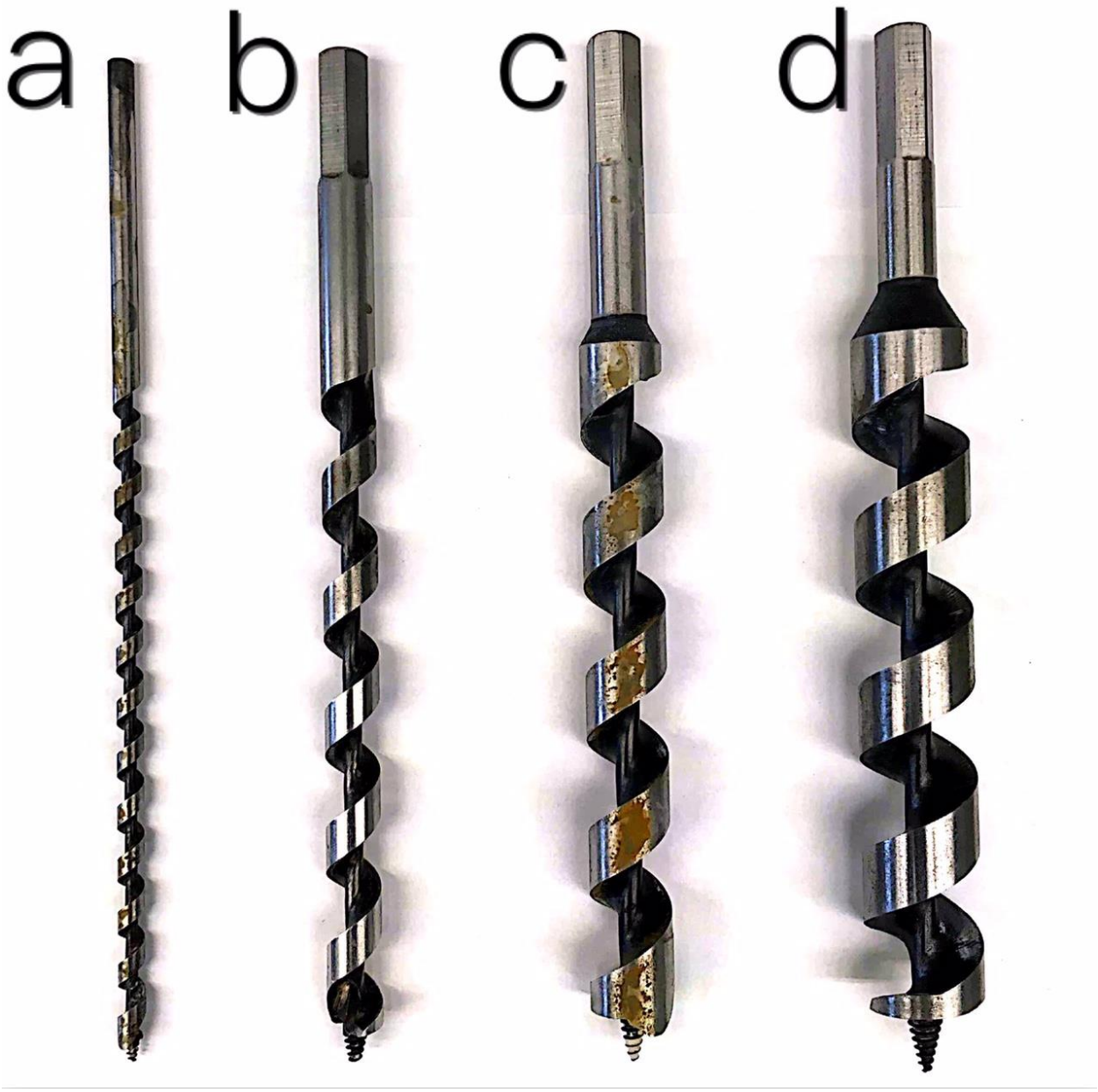

Figure 3.7: (a) 0.25”, (b) 0.5”, (c) 0.75” and (d) 1”wood augers used to drill holes in the center of the fine-grained soil specimens for the placement of hydrate veins.

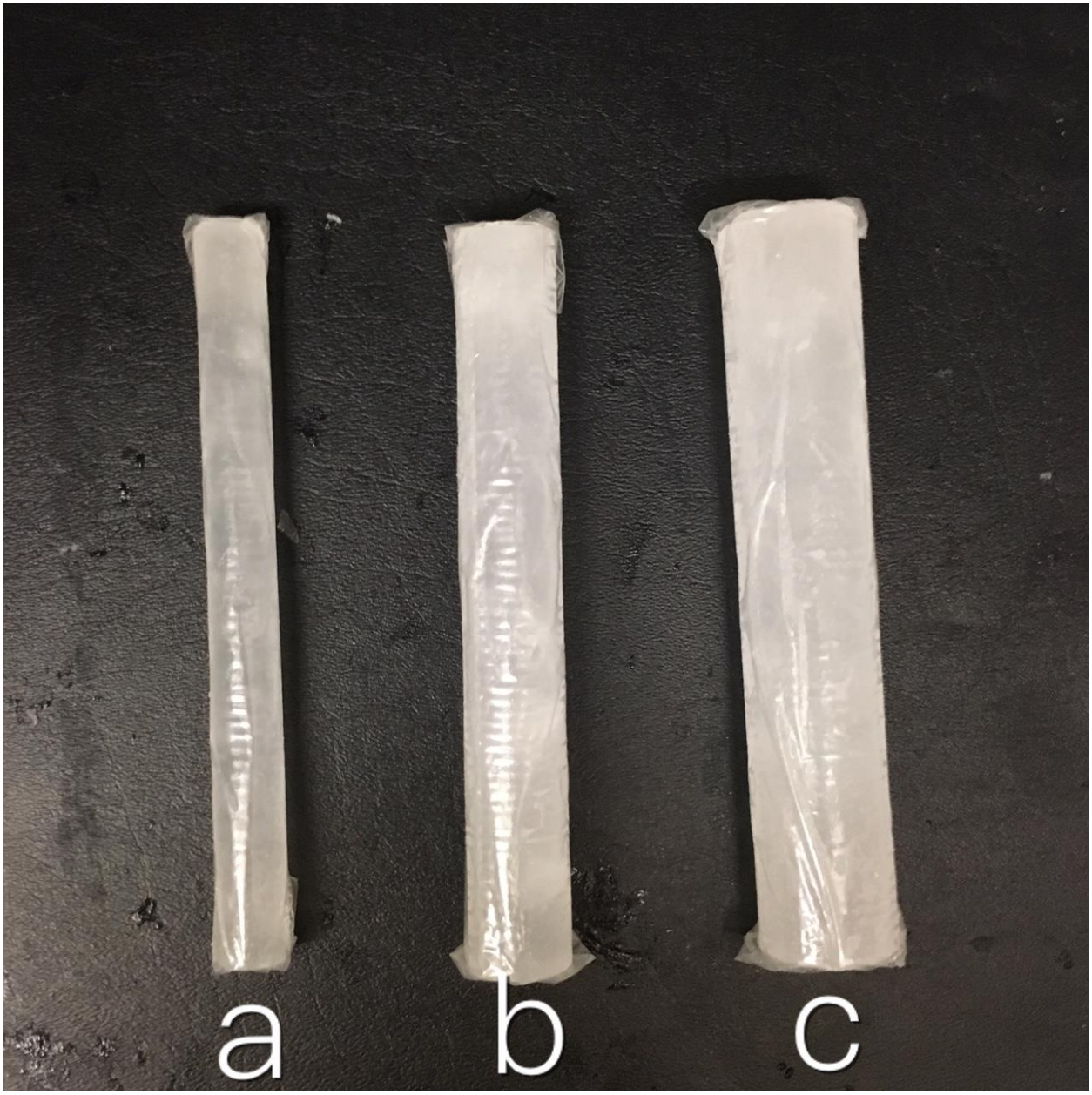

Figure 3.8: (a) 0.5”, (b) 0.75” and (c) 1”-diameter hydrate veins wrapped in a thin plastic wrap.

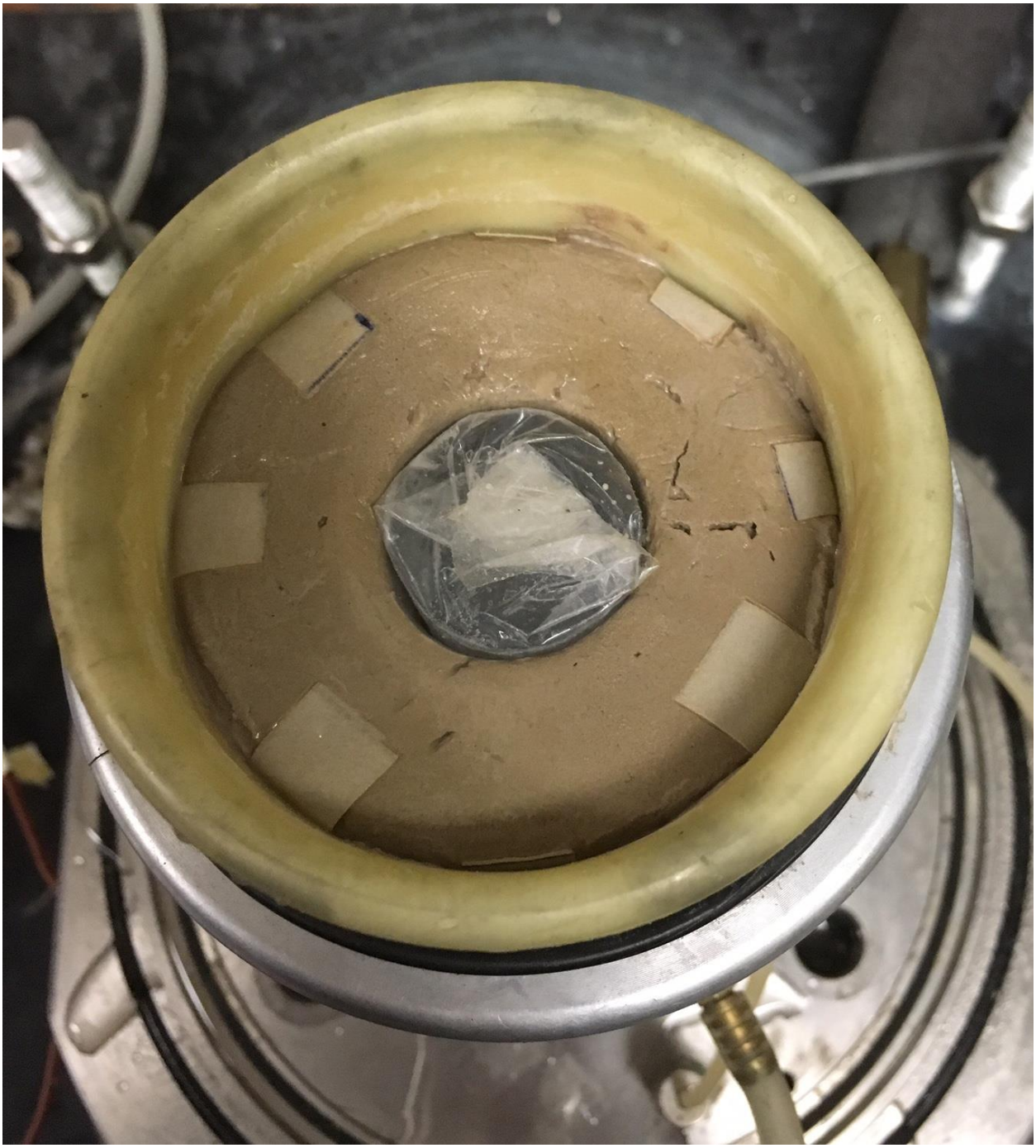

Figure 3.9: A hydrate-bearing fine-grained soil specimen containing a 1”-diameter hydrate vein.

Figure 3.10: Modified low-temperature triaxial system including (a) 25 kN load frame and cell, (b) controlling system including two coolers, cooling tubes and cooling base plate (c) designed and constructed cooling system.

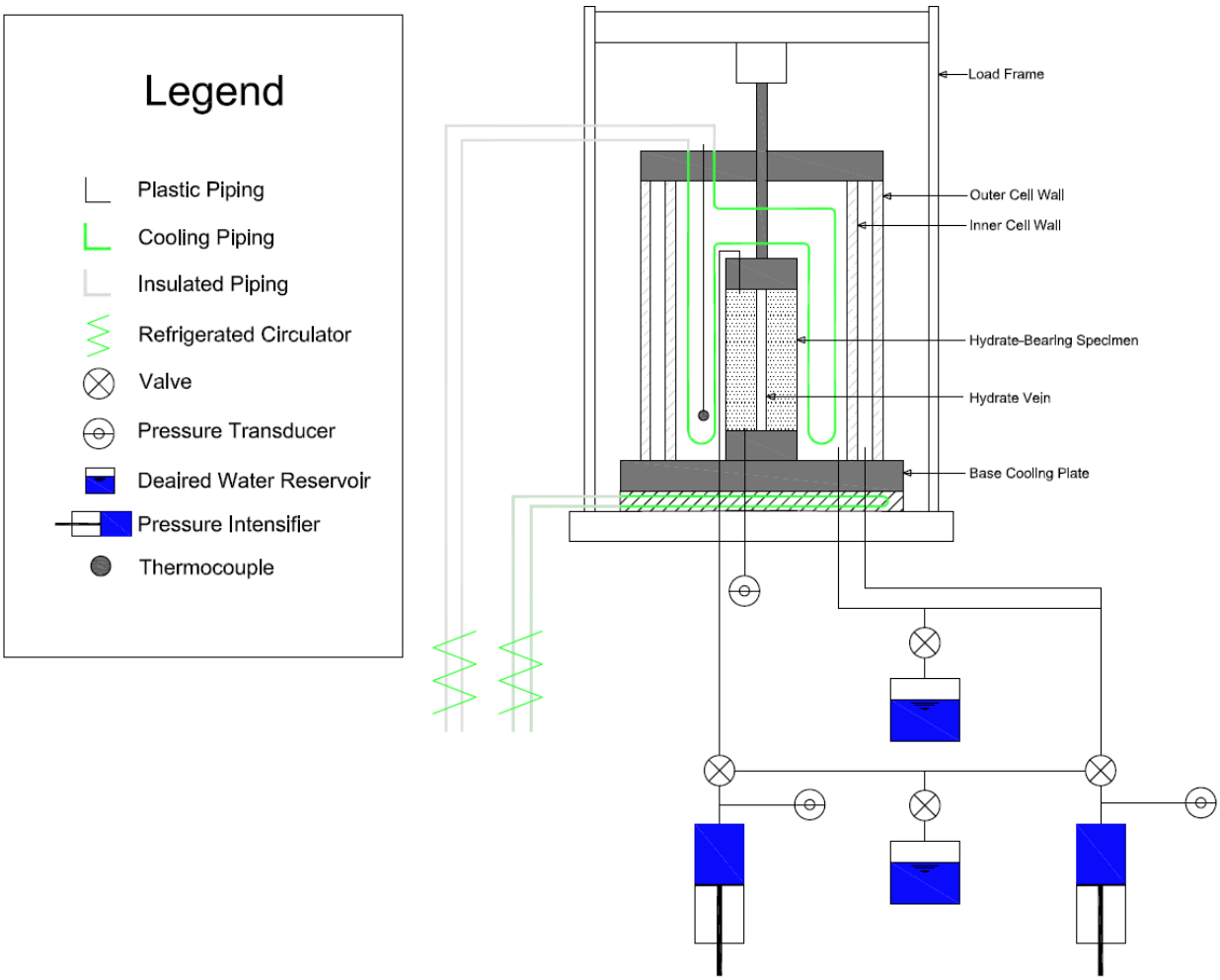

Figure 3.11: Schematic diagram of the modified low-temperature triaxial system.

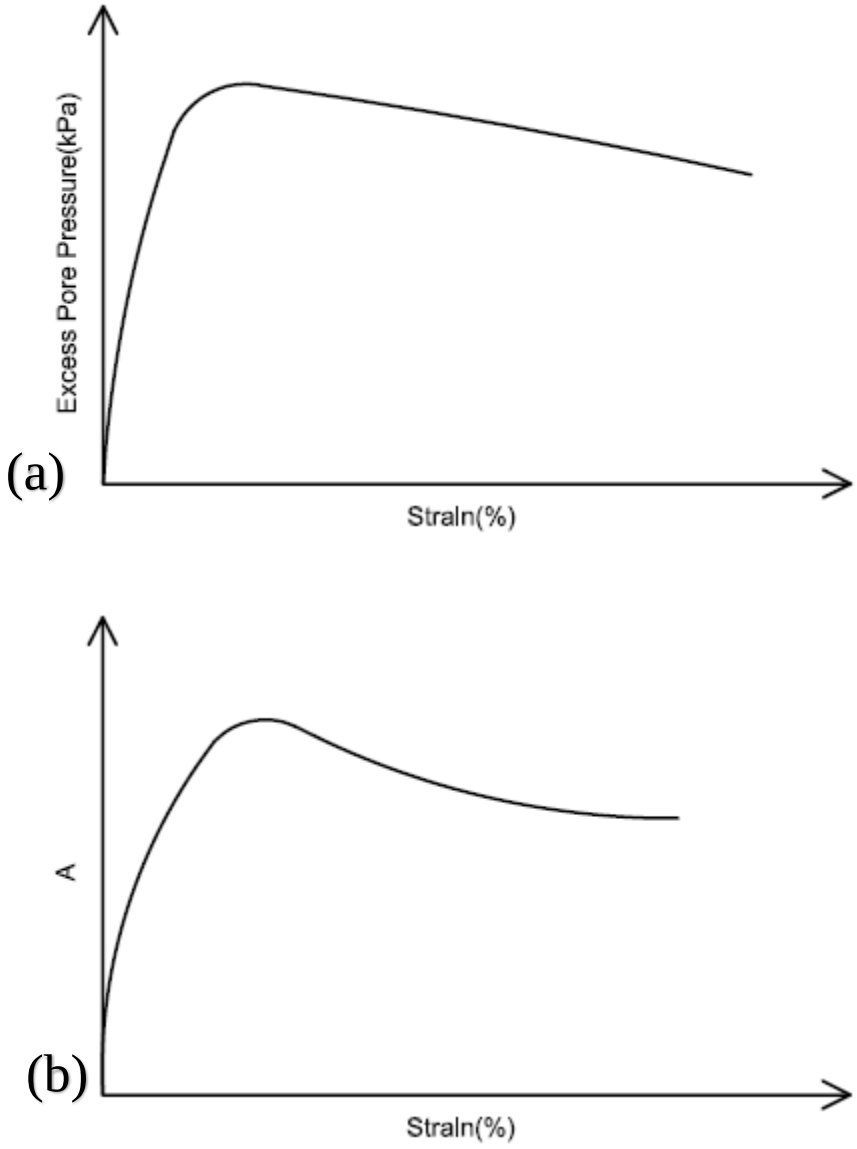

Figure 3.12: Typical (a) excess pore pressure and (b) pore pressure coefficient (A) response to strain.

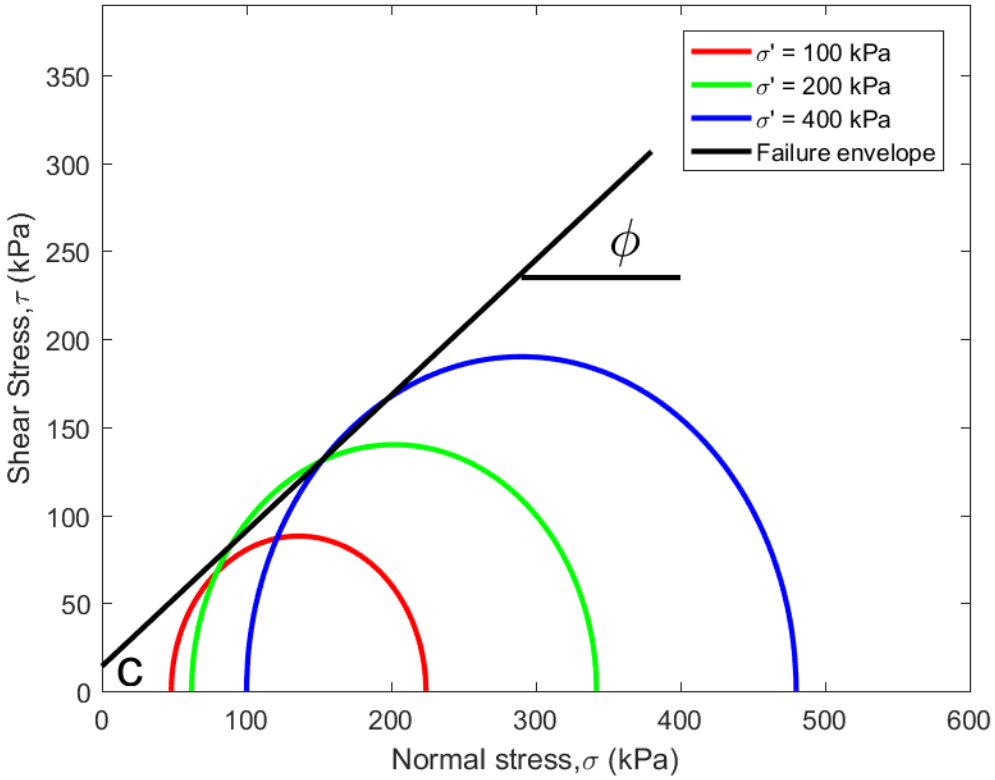

Figure 3.13: Example plot for the strength criteria of the specimens.

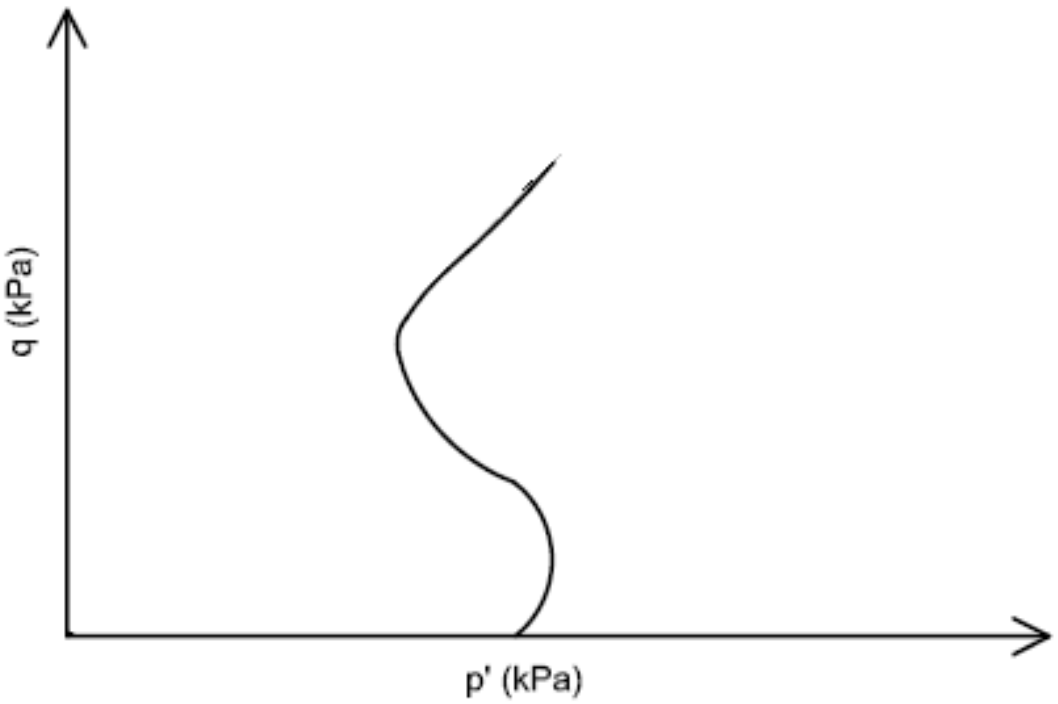

Figure 3.14: Typical effective stress path for specimen.

Chapter Four: Laboratory Results and Discussion

4.1 Introduction

This chapter presents the results of the laboratory tests designed to investigate the impact of hydrate veins on the geomechanical behaviour of hydrate-bearing fine-grained sediments.

4.2 Baseline Compression Testing on Hydrate Veins

As this research is considering the impact of hydrate veins on the behaviour of fine-grained soils, strength tests were conducted first to investigate the performance of hydrate veins under a range of different conditions, such as strain rate and confining stress. Compression tests were carried out on 6.35 mm (0.25”), 12.7 mm (0.5”), 19.05 mm (0.75”) and 25.4 mm (1”) diameter and 140 mm height cylindrical THF hydrate veins to understand how the inclusion of stiff hydrate veins change the geomechanical behavior of the host sediments. Strain controlled tests were carried out with strain rates of 0.05, 0.3 and 0.5%/min to investigate the impact of strain rate on the stress-strain behavior of hydrate veins. All the compression tests on hydrate veins are summarized in Table 4.1.

4.2.1 Stress-strain behavior.

As highlighted above hydrate veins of different diameters were subjected to axial compression tests. Figure 4.1 presents deviatoric load, Q against axial strain, ε_a for different vein diameters at a strain rate of 0.05%/min (Specimen V1-V4, Table 4.1). The results clearly show that as vein diameter increases a corresponding increase in Q that can be carried by the hydrate vein occurs. The peak load, Q that can be carried increases from 0.1 kN for the 0.25” vein up to 1.45 kN for the 1” vein. Typically for a given material a unique relationship exists between stress vs strain.

To consider this Figure 4.2 presents the deviatoric stress, q plotted against ε_a for the different hydrate veins shown in Figure 4.1. It can be seen that when plotted as axial stress against axial strain the different hydrate veins exhibit similar behavior. All veins show similar increases in strength with increasing strain and reaching similar peak strength (defined as the point of peak stress) with significant post peak reduction in strength, suggesting brittle failure of the hydrate veins.

Figure 4.3 shows the measured peak strength against hydrate vein cross-sectional area for the different veins while Figure 4.4 shows the measured vein stiffness, E_{50} against hydrate vein cross-sectional area, where E_{50} is the secant modulus obtained from the slope of the line joining the origin to the point on the stress-strain curve corresponding to 50% of the peak deviatoric stress for each vein. It can be seen from these that the peak strength and stiffness of the different hydrate veins are in reasonably close agreement.

Visual observations of the hydrate veins during testing suggest that failure of the hydrate vein occurs due to the development of a rupture plane in the vein (see section 4.2.2) around the measured peak stress. Preliminary compression tests of hydrate veins with and without plastic membrane showed similar peak stresses at failure. However, the plastic membrane provided some restraint to the post peak rupturing of the veins by preventing complete separation of the ruptured pieces.

Given the reasonable close agreement in peak stress for the different hydrate veins suggests that the strength of the hydrate veins is independent of vein diameter. In addition, factors such as

slenderness ratio of the veins (height to diameter) and therefore potential differences in buckling loads also do not seem to influence the overall strength of the hydrate vein.

The minor variation in strength and stiffness of the hydrate veins that were observed might be related to vertical alignment of the vein during set up, minor differences in the level and roughness of the top and bottom faces of the hydrate veins.

4.2.1.1 Rate of shearing.

As stated in Section 2, CU and UU tests that were conducted on hydrate-bearing fine-grained soil specimens gave rise to appreciable differences peak strength of the specimens that may have been related to the different strain rates that were applied in those tests. To consider the impact of hydrate vein strength as a function of strain rate tests were carried out on 0.5", 0.75" and 1"-diameter veins with different strain rates (0.05, 0.3 and 0.5%/min). Figure 4.5(a), (b) and (c) show the influence of strain rate for the three different vein diameters. It can be seen that the highest load corresponded to the lowest strain rate of 0.05%/min. However, given the close agreement in peak axial load observed for the three strain rates applied suggest that the vein strength is independent of strain rate.

4.2.1.2 Confining pressure.

Other parameters that are varied between CU and UU tests, for example the hydrate-bearing soil specimens of Smith (2016), are the total and effective confining stresses. Smith (2016) suggested that the increase in specimen strength between the CU and UU tests could have been related to the increase in effective stress on the soil matrix in the specimen and therefore

mobilising more soil strength to resist failure of the vein during shear. However, as the total stress was higher in the CU test than the UU tests the increase in strength may have been a function of the total stress acting on the specimen, and hence the hydrate vein, and not related to soil strength. The difference in stress condition between CU and UU tests on soil specimens is shown schematically in Figure 4.6.

To investigate the influence of total stress, and hence effective stress since the hydrate is soild, an additional compression test was carried out on a 1" diameter vein with a shear strain rate of 0.05%/min with a cell pressure of 500 kPa acting on the hydrate vein. Figure 4.7 shows the variation in Q with ε_a for the 1" diameter vein at confining pressure of 0 kPa and 500 kPa. The results illustrate remarkably similar behaviour up to peak behaviour. Post peak behaviour differed somewhat with the vein subject to higher confining pressure showing less brittle post peak behaviour. It is considered that the more gradual reduction in post peak stress for the specimen under 500 kPa is due to the plastic membrane providing greater resistance to sliding under higher confining stresses for the separate sections of the ruptured hydrate vein.

4.2.2 Failure mode.

The results from the testing conducted suggest that the strength and stiffness of hydrate veins under axial compression are largely independent of factors such as vein size, strain rate and confining pressure. Another factor that was observed during testing that might impact the overall behaviour of hydrate-bearing fine-grained soil specimens is the mode of fracture at peak stress.

Figure 4.8 and 4.9 show typical post shear images of the THF veins highlighting distinct differences in fracture geometry. In Figure 4.7 the THF vein appears to have fractured horizontally. In contrast, the specimen in Figure 4.8 shows a more typical shear failure along a diagonal plain. Visual examination of formed hydrate veins prior to testing typically show structural defects in the hydrate vein that may give rise to these different failure modes. However, the peak strength and initial stiffness of the hydrate vein specimens do not vary appreciably, suggesting that the failure mode for the vein does not significantly influence the behaviour of hydrate veins up to peak stress.

4.3 Consolidated-Undrained (CU) Compression Testing

4.3.1 Stress-strain behavior.

Consolidated-Undrained compression tests were carried out on fine-grained specimens, with and without hydrate veins in order to investigate the impact of hydrate veins and effective stress on the geomechanical behavior of the fine-grained soils. Table 4.2 summarizes the results of the variety of tests that were conducted.

In the tests presented, failure of the specimen was assumed to occur when the soil specimen reaches its critical state. Roscoe at al. (1958) defined the critical state as the state at which the soil continues to deform at constant stress and constant void ratio. The critical state concept represents the idealized behavior of remoulded clays, but it is assumed to apply also to undisturbed clays in triaxial compression tests. The secant modulus E_{50} for each specimen was calculated for the stiffness of all the specimens.

Figure 4.10 - 4.12 presents deviatoric stress, q against axial strain, ε_a for specimens with different diameters of hydrate veins (0.25", 0.5", 0.75" and 1") along with a specimen with no hydrate vein. Three different effective stress conditions were investigated, namely 100, 200 and 400 kPa. A comparison between the hydrate-free specimen and those containing hydrate veins of different diameters shows that the peak deviatoric stress and stiffness of the specimens increases with hydrate vein diameter under the same effective stress.

To better consider the influence of effective stress on the observed behaviour, Figure 4.13 presents deviatoric stress, q against axial strain, ε_a for the specimens for the different vein sizes considered. The results clearly show that peak deviatoric stress and stiffness increase with effective stress. Given that soil strength is stress dependent, but the hydrate vein itself was independent of effective stress, it is suggested that the increase in specimen strength was related to the soil matrix mobilizing more soil strength, which in turn resisted the failure of the vein during the shear.

4.3.2 Pore pressure response.

The relationship between the strength of the soil tested under undrained condition and the strength characteristics expressed in terms of effective stress is dependent on the pore pressure measured during a test (Skempton, 1954). To better understand how the pore pressure responded to the different combinations of applied stress, excess pore pressure (u) was measured during the tests and the pore pressure parameter (A) was calculated. Figure 4.14 and 4.15 shows u and A against axial strain, ε_a for tests on the hydrate-free and hydrate-bearing specimens under different effective stress conditions. It can be seen in Figure 4.14 that the pore pressure response is

dominated by the change in effective stress and appears to be independent of hydrate vein size. In contrast the pore pressure coefficient, A is significantly influenced by vein size. The value of A depends on whether the soil is normally consolidated or over-consolidated, and on the relative applied stresses at failure. It can be seen that for the specimen without hydrate, and those with small vein diameters, that A displays an early peak, indicating compression of the sample and then decreases as the soil dilates with increasing strain. It can be seen that as σ' increases the post peak reduction is somewhat muted (less dilation post shear). At higher vein diameters the increased hydrate vein diameter is capable of carrying the higher deviatoric stresses, and therefore not fully felt by the soil before failure of the vein and the sediment. As such the increase in σ' is also muted.

4.3.3 Effective stress paths.

Figure 4.18 shows a plot of the deviatoric stress, q vs mean effective principal stress, p' during triaxial shear highlighting the effective stress path followed by the specimens. The fine-grained specimens without hydrate vein show a typical stress path for normally consolidated fine-grained sediments, where increasing deviatoric stress gives rise to an increase in pore pressure (compression of the specimen) leading to a reduction in p' at increasing shear stress until the specimen fails, at which point a reduction in pore pressure occurs such that p' starts increasing with increasing q, as plotted in Figure 4.16. The presence of hydrate vein reduces the pore pressure response of the host sediments, and allows the sediments to withstand higher deviatoric stress conditions that lead to identifiable peak stresses at failure. After reaching the peak deviatoric stress, the stress path of hydrate-bearing specimen falls backward. This indicates that the presence of hydrate vein influences the post-peak behavior of the fine-grained sediments.

For the specimens with 1”-diameter hydrate vein at 100 kPa, effective stress, the large strength of the vein is such that the specimen follows a very different stress path with q increasing sufficiently quicker than the pore pressure such that p’ does not reduce, and therefore the soil exhibits a more typical ‘drained response’. At higher effective stresses a more typical response is observed for specimen with 1” veins.

4.3.4 Strength criteria.

Figure 4.17 presents the Mohr-Coulomb failure lines for of hydrate-free and hydrate-bearing soil specimens. It can be observed that the increase in strength of hydrate-bearing soils as the hydrate vein size increases is mainly manifested as an increase in cohesion induced by the hydrate vein. The value of cohesion derived for both the hydrate-free and hydrate-bearing specimens as a function of hydrate vein cross-sectional area is shown in Figure 4.18. The increase in cohesion of the specimens is clearly dependent on the size of hydrate veins and not significantly influenced by the increase in effective stress. The friction angle when the hydrate vein area increased from 0 to 285 mm^2 (0 – 0.75” diameter) was reasonably constant varying from 35° to 37°. However, the frictional angle for the specimen with 506 mm^2 (1” diameter) hydrate vein area reduced significantly (22°) highlighting that both cohesion and friction angle are dominated by the 1”–diameter hydrate vein, which contributes to the majority of the strength of the hydrate-bearing soil specimen. These results show that the strength of the fine-grained sediments is enhanced with the presence of hydrate vein of any size, with the relative changes in cohesion and friction angle appearing to be dependent on the hydrate vein size rather than effective stresses.

4.3.5 Failure modes and post-shear analysis.

For fine-grained specimens without hydrate veins, the failure of the soil exhibited plastic yielding, while for hydrate-bearing specimens the shear failure become increasingly brittle as the hydrate vein diameter increased. For the hydrate-bearing specimens different failure modes were observed including horizontal fracturing, diagonal fracturing and plastic creep failure, which are presented in Figure 4.19. Among the failure modes, horizontal fracturing was the most common failure mode, especially for the smaller diameter veins. It can be considered that as the hydrate vein was ruptured horizontally, the top segment started to rotate about the fracture with increasing axial strain since the two segments were not able to slide past one another due to the geometry of horizontal fracture. Diagonal fracturing may allow a shear plane to be developed through the soil and hydrate vein allowing the two hydrate segments to slide pass one another, but has no distinctive effect on the strength behavior of hydrate-bearing specimens. Plastic creep failure was only noted for 0.75" and 1"-diameter hydrate veins, possibly due to their higher diameter to height ratio, which may reduce bending stress in the vein, and aided by confinement provided by the soil.

In tests conducted by Smith (2016) a significant increase in peak strength was observed for hydrate-bearing specimens where the hydrate vein failed by horizontal fracture. Given the results from the tests on hydrate veins themselves it is considered that the differences between the peak strength observed for THF veins and hydrate-bearing sediments when a horizontal fracture occurs is a function of the confining stresses applied by the sediment. For the THF veins once the vein has fractured the top and bottom parts are reasonably free to rotate or slide over each other. However, for hydrate-bearing sediments, especially when a horizontal fracture

occurs, the sediment can prevent the hydrate vein from rotating, leading to an enhanced observed strength when compared to a diagonal fracture where sliding of the two parts of the vein maybe easier.

4.4 Geomechanical impact of THF hydrate veins and effective stress on hydrate-bearing specimens

4.4.1 Geomechanical impact of THF hydrate veins on hydrate-bearing specimens.

Quantifying the geomechanical impact of THF hydrate veins on hydrate-bearing specimens is essential in order to understand the relationship between the size of hydrate vein and geomechanical behavior of the specimen.

Hydrate content is usually defined as hydrate saturation of the pore space(S_h), which is the ratio of the hydrate volume (V_h) to the void space of the soil (V_v):

$$S_h = \frac{V_h}{V_v} \times 100\% \tag{4.1}$$

However, hydrate saturation is typically used to quantify hydrate content which is homogeneously distributed within the interconnected pore space of the sediment. This definition might not be appropriate for laboratory-formed hydrate-bearing fine-grained specimen, in which hydrate exists as solid cylindrical veins, and no hydrate exists within the pore space of the soil surrounding the hydrate vein.

Therefore, an alternative definition of hydrate vein saturation (S_{vh}) was suggested by Smith (2016) as the ratio of the volume of hydrate vein to the total volume of voids, which is the sum

of volume of hydrate vein (V_{vein}) and volume of voids in the surrounding soil ($V_{v(soil)}$) as given by

$$S_{vh} = \frac{V_h}{V_{vein}+V_{v(soil)}} \times 100\% \quad (4.2)$$

Smith further suggested another alternative definition called the area ratio (AR), which was the ratio of the cross-sectional area of the vein (A_{vein}) to the specimen area ($A_{specimen}$) given by:

$$AR = \frac{A_{vein}}{A_{specimen}} \quad (4.3)$$

By using this definition, the behavior of natural hydrate-bearing sediments could be estimated when the hydrate volume and soil's void ratio are unknown or variable but the relevant areal proportion of hydrate veins can be estimated (Smith, 2016).

4.4.1.1 Strength dependency on hydrate vein size.

The undrained shear strength (S_u) of all the specimens tested are listed in Table 4.2 and is defined as half of the deviatoric stress when the specimen reaches the critical state (q_{cs}), as given by:

$$S_u = \frac{q_{cs}}{2} \quad (4.4)$$

Figure 4.20 shows the variation in undrained shear strength with hydrate vein area ratio for the specimens tested under different effective stresses (100, 200 and 400 kPa). The results demonstrate that the undrained shear strength of the specimens is principally governed by hydrate vein area ratio; increasing area ratio leads to linear increase in undrained shear strength. Fitting a linear trendline to the data the relationship between undrained shear strength and hydrate vein size, as a function of effective stress, could be defined by equations:

$$S_u = 1862AR + 30 \quad (4.5)$$

$$S_u = 1554AR + 81 \quad (4.6)$$

$$S_u = 1314AR + 151 \quad (4.7)$$

for effective stress of 100, 200 and 400 kPa, respectively. These trendlines show that the influence of the hydrate vein on Su reduces with increasing effective stress.

4.4.1.2 Stiffness dependency on hydrate vein size.

The stiffness (E_{50}) of all the specimens were calculated and shown in Table 4.2. Figure 4.21 shows the variations in stiffness of the specimens with hydrate vein area ratio under different effective stresses (100, 200 and 400 kPa). The results demonstrate that the stiffness of the specimens is largely governed by hydrate vein area ratio; increasing area ratio leads to increase in stiffness. A relatively linear relationship, relating the stiffness of the specimen to the hydrate vein area ratio under effective stress of 100 kPa, is defined by equation 4.9. However, at higher effective stresses the relationship is somewhat different, in that for hydrate veins with an area ratio lower than 0.074 the stiffness is influenced by the effective stress, while for specimens with hydrate vein area ratio greater than 0.074 stiffness is independent of confining stress

$$E_{50} = 308731AR + 22917 \quad (4.8)$$

4.4.2 Geomechanical impact of soil's effective stress on hydrate-bearing specimens.

Quantifying the geomechanical impact of effective stress on the behaviour of hydrate-bearing sediments is essential in order to investigate however the natural state of the soil in the sediment column may dictate its behaviour.

4.4.2.1 Strength dependency on effective stress.

Figure 4.22 shows the variation in undrained shear strength of different specimens with effective stress. The results demonstrate that the undrained shear strength is influenced by effective stress; increasing effective stress leads to increase in undrained shear strength. Since the strength of hydrate vein was not influenced by the effective stress acting on it, would suggest the increase in the strength of hydrate-bearing specimen is a function of the effective stress acting on the soil matrix. Linear relationships defined by equations:

$$S_u = 0.37\,\sigma' + 2.5 \tag{4.9}$$

$$S_u = 0.37\,\sigma' + 9.75 \tag{4.10}$$

$$S_u = 0.33\,\sigma' + 63 \tag{4.11}$$

$$S_u = 0.3\,\sigma' + 132.5 \tag{4.12}$$

$$S_u = 0.16\,\sigma' + 260.5 \tag{4.13}$$

were observed to be able to empirically relate undrained shear strength to the effective stress for specimens of 0, 0.008, 0.03, 0.07 and 0.13 area ratio, respectively. In the absence of hydrate, the undrained shear strength of sediments is of a frictional nature as suggested by the Mohr-Coulomb failure criteria and therefore a function of effective stress. When hydrate vein is

present, the undrained shear strength increases with hydrate vein area ratio and becomes less dependent on effective stress in specimens of higher hydrate vein area ratio.

4.4.2.2 Stiffness dependency on effective stress.

Figure 4.23 shows the variation in stiffness of different specimens with effective stress. The results demonstrate that the stiffness of sediments without hydrate, and with low hydrate vein area ratio (0.008), is governed by effective stress; increasing effective stress leads to increase in stiffness. For specimens with higher hydrate vein area ratio (0.03 and 0.07), the stiffness increases by around 36% to 33% when effective stress is increased from 100 kPa to 200 kPa. However, the stiffness of the specimens become somewhat independent of effective stress when the effective stress is higher than 200 kPa. For specimens with hydrate vein area ratio of 0.13, the stiffness of specimen is somewhat independent of effective stress.

4.4.3 Stiffness-strength correlation.

The dependency of undrained shear strength and stiffness of the specimens on effective stress and hydrate vein area ratio suggests a correlation between undrained shear strength and stiffness. Figure 4.24 shows the calculated stiffness against undrained shear strength for all test specimens. A linear best fit line, of the form $E_{50} = 165\ S_u + 16500$ can be applied to define the correlation between stiffness and strength that can help better understand the geomechanical behavior of hydrate-bearing fine-grained specimens.

4.5 Potential impact of hydrate veins on natural sediments

Theoretical and laboratory evidence shows that the inclusion of hydrate veins will result in increased in-situ strength and stiffness of the hydrate-bearing sediments. Thus the natural hydrate-bearing sediments within the sediment column would be able to support more overburden stress than expected at a given depth due to the inclusion of hydrate veins. Therefore, the compressibility of the host sediments will be reduced significantly under vertical loading by the presence of hydrate vein within the sediments and reduce or prevent the normal consolidation process of the sediments since the hydrate veins are strong enough to support the overload. Therefore, if the hydrate vein formation occurred at shallower depths the sediments around the hydrate veins would be under-consolidated. This under-consolidation process would lead to significant reduction in in-situ sediment strength if the hydrate were to dissociate, and potentially lead to the failure of the soil. Therefore, quantifying the impact of hydrate vein area ratio or hydrate saturation on the strength and stiffness increase of the sediments is essential to understand the behavior of hydrate-bearing fine-grained sediments and assess the risk of soil failure after hydrate dissociation. If the hydrate veins are hosted within the soft and under-consolidated soil, the relationship between geomechanical behavior of the hydrate-bearing sediments and hydrate vein area ratio under low effective stress shown in Figure 4.20 and 4.21 can be used to predict the strength and stiffness of the hydrate-bearing fine-grained sediments in terms of known hydrate vein area ratio. If the fine-grained soil around the hydrate vein is consolidated to a significant effective confining stress due to the sediment overburden prior to hydrate formation, the results of CU tests under different effective stress shown in Figure 4.22 and 4.23 may be useful to predict the geomechanical behavior of hydrate-bearing fine-grained sediments. Therefore, the location where hydrate veins are formed is important for sediments

failure assessment. On the one hand, the hydrate-bearing fine-grained sediments close to the seafloor are more likely to fail if the hydrates were to dissociate, considering the veins at near surface dominate strength and stiffness of the hydrate-bearing fine-grained sediments. The in-situ sediments tend to be under-consolidated since most of the load subjected to the sediments is supported by the hydrate veins, which hinder the ongoing consolidation process. Also, the dissociation of hydrate close to the seafloor is more likely to happen due to the less time required for the heat transfer. On the other hand, the hydrate-bearing fine-grained sediments close to the base of hydrate stability zone are less likely to fail if the hydrates were to dissociate, considering the hydrate vein has less impact on the sediments at higher effective stress. Therefore, the change in strength behavior of hydrate-bearing fine-grained sediments might not be as great.

Apparently, the hydrate-bearing fine-grained sediments are strengthened by the inclusion of hydrate veins and able to support more overburden stress at a given depth. However, the dissociation of gas hydrate would lead to a significant reduction in sediment strength due to the loss of hydrate veins. The consolidation process of the soil matrix around the hydrate vein continues after the hydrate veins disappear. The continuing consolidation of the soil would lead to the enhanced pore pressure and hence reduced effective stress, possibly leading to seafloor instability. Therefore, the risk of marine sediments failure can be better assessed by predicting the strength and stiffness of the hydrate-bearing sediments within known hydrate saturation and depth.

4.6 Summary

The stress-strain behavior of THF hydrate veins was analyzed to investigate the strength and stiffness of THF hydrate veins. By carrying out axial compression tests on standalone cylindrical hydrate veins of different sizes it was shown that although the deviatoric load carried by hydrate veins increased with vein diameter, the peak strength and the stiffness of the different hydrate veins were comparable. The results also showed that factors such as strain rate, confining pressure and failure modes of hydrate veins had no appreciable effect on stress-strain behavior of hydrate veins. These results are of value to help increase our understanding of the impact of hydrate veins on the behaviour of hydrate-bearing fine-grained sediments.

The stress-strain behavior of hydrate-free and hydrate-bearing fine-grained specimens were analyzed to investigate the impact of hydrate vein size and effective stress on the strength and stiffness of hydrate-bearing specimens. Undrained shear strength and stiffness are observed to increase with both hydrate vein size and effective stress. The Mohr-Coulomb criterions of hydrate-free and hydrate-bearing specimens have been developed to better understand the hydrate-bearing soil behavior. The results indicate that strengthening of hydrate-bearing soils as the hydrate vein size increases is mainly due to an apparent increase in cohesion from the hydrate vein.

The impact of hydrate vein size and effective stress was quantified to investigate the strength and stiffness dependency on hydrate vein size and effective stress. The undrained shear strength and stiffness of hydrate-bearing fine-grained specimen can be predicted in terms of hydrate vein area

ratio and effective stress. A simple linear relationship of $E_{50} = 165\ S_u + 16500$ is developed to predict the geomechanical behavior of hydrate-bearing fine-grained specimens.

Table 4.1: Summary of compression tests on hydrate vein specimens.

Specimen No.	Diameter (inch/mm)	Confining Pressure (kPa)	Strain Rate (%/min)	Failure Mode	Peak Strength (kN)	Peak Stress (kPa)	Stiffness (MPa)
V1	0.25/6.35	0	0.05	Diagonal	0.09	2749	221
V2	0.5/12.7	0	0.05	Diagonal	0.36	2843	237
V3	0.75/19.05	0	0.05	Horizontal	0.83	2914	246
V4	1/25.4	0	0.05	Diagonal	1.46	2883	263
V5	1/25.4	500	0.05	Diagonal	1.35	2666	255
V6	0.5/12.7	0	0.3	Diagonal	0.33	2606	240
V7	0.5/12.7	0	0.5	Horizontal	0.3	2369	228
V8	0.75/19.05	0	0.3	Diagonal	0.76	2668	242
V9	0.75/19.05	0	0.5	Diagonal	0.74	2598	256
V10	1/25.4	0	0.3	Diagonal	1.41	2784	258
V11	1/25.4	0	0.5	Horizontal	1.22	2410	251

Table 4.2: Summary of CU tests on hydrate-free and hydrate-bearing specimens.

Specimen No.	Hydrate Vein Diameter (inch/mm)	Area Ratio	Effective Stress (kPa)	Undrained Shear Strength (kPa)	Stiffness (kPa)	Failure Mode
S1	0/0	0	100	37.5	21000	N/A
S2	0.25/6.35	0.008	100	43.5	25000	Horizontal
S3	0.5/12.7	0.03	100	88	35384	Horizontal
S4	0.75/19.05	0.07	100	160	47192	Diagonal
S5	1/25.4	0.13	100	280.5	62222	Horizontal

S6	0/0	0	200	80	27272	N/A
S7	0.25/6.35	0.008	200	90	32068	Horizontal
S8	0.5/12.7	0.03	200	140	48158	Diagonal
S9	0.75/19.05	0.07	200	195	63000	Diagonal
S10	1/25.4	0.13	200	285	65000	Creep
S11	0/0	0	400	157.5	35106	N/A
S12	0.25/6.35	0.008	400	158.5	08	Horizontal
S13	0.5/12.7	0.03	400	190	46896	Diagonal
S14	0.75/19.05	0.07	400	250	66486	Creep
S15	1/25.4	0.13	400	325	68076	Creep

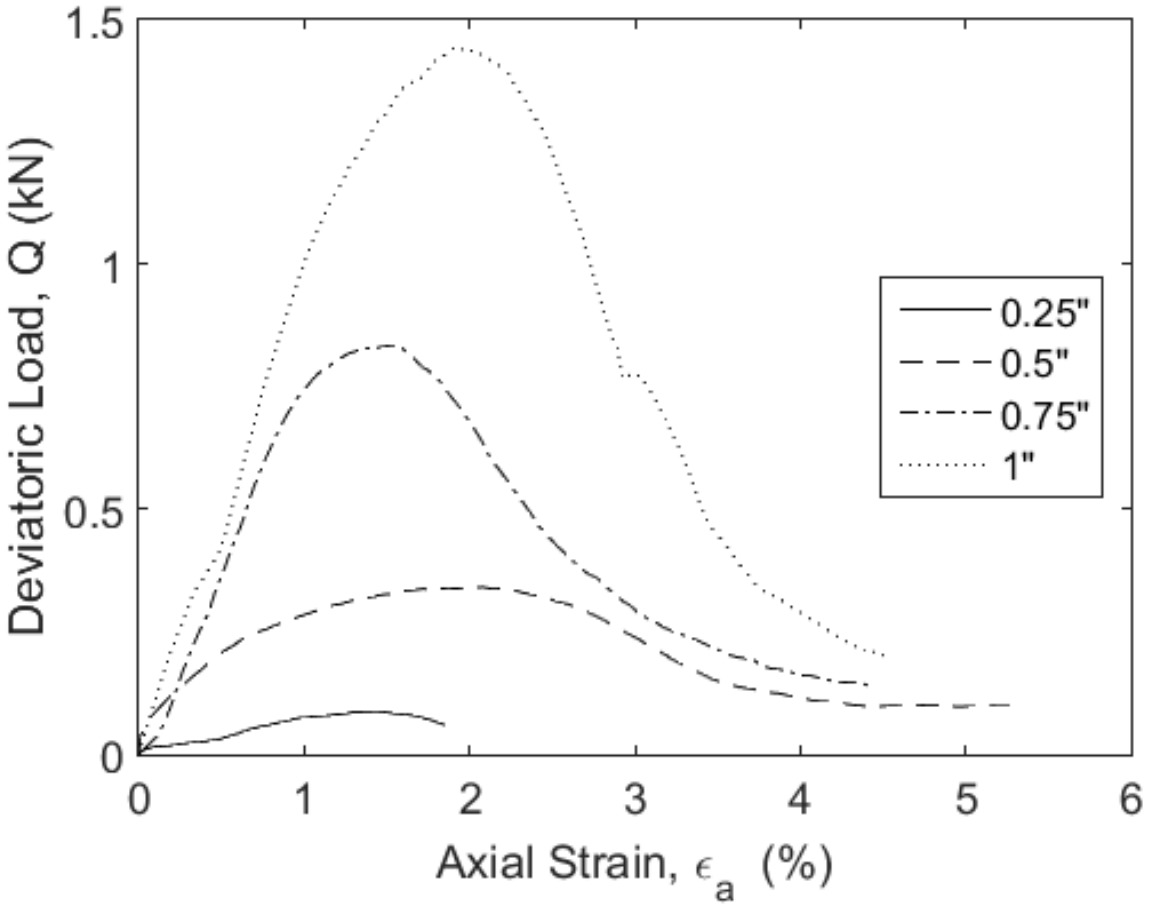

Figure 4.1: Deviatoric load against axial strain for different diameters of hydrate veins.

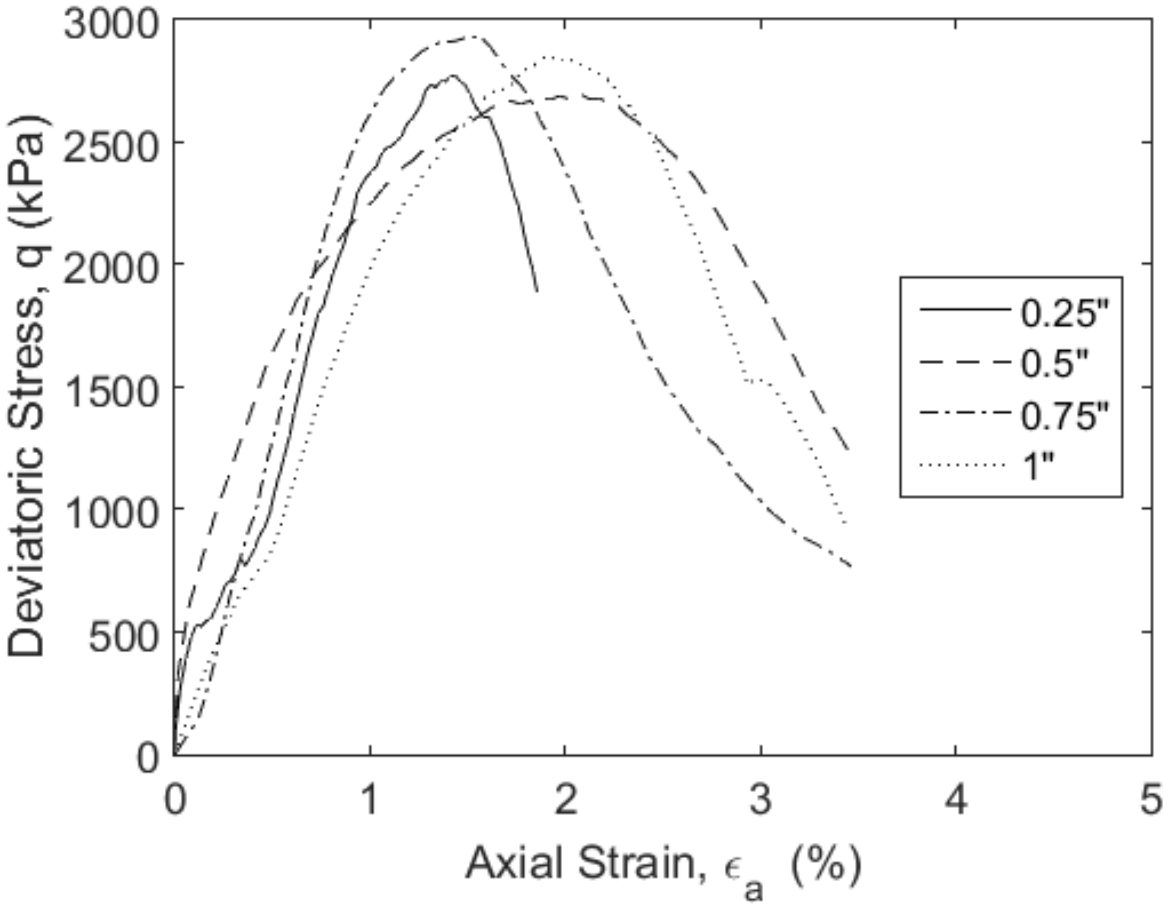

Figure 4.2: Deviatoric stress against axial strain for different diameters of hydrate veins.

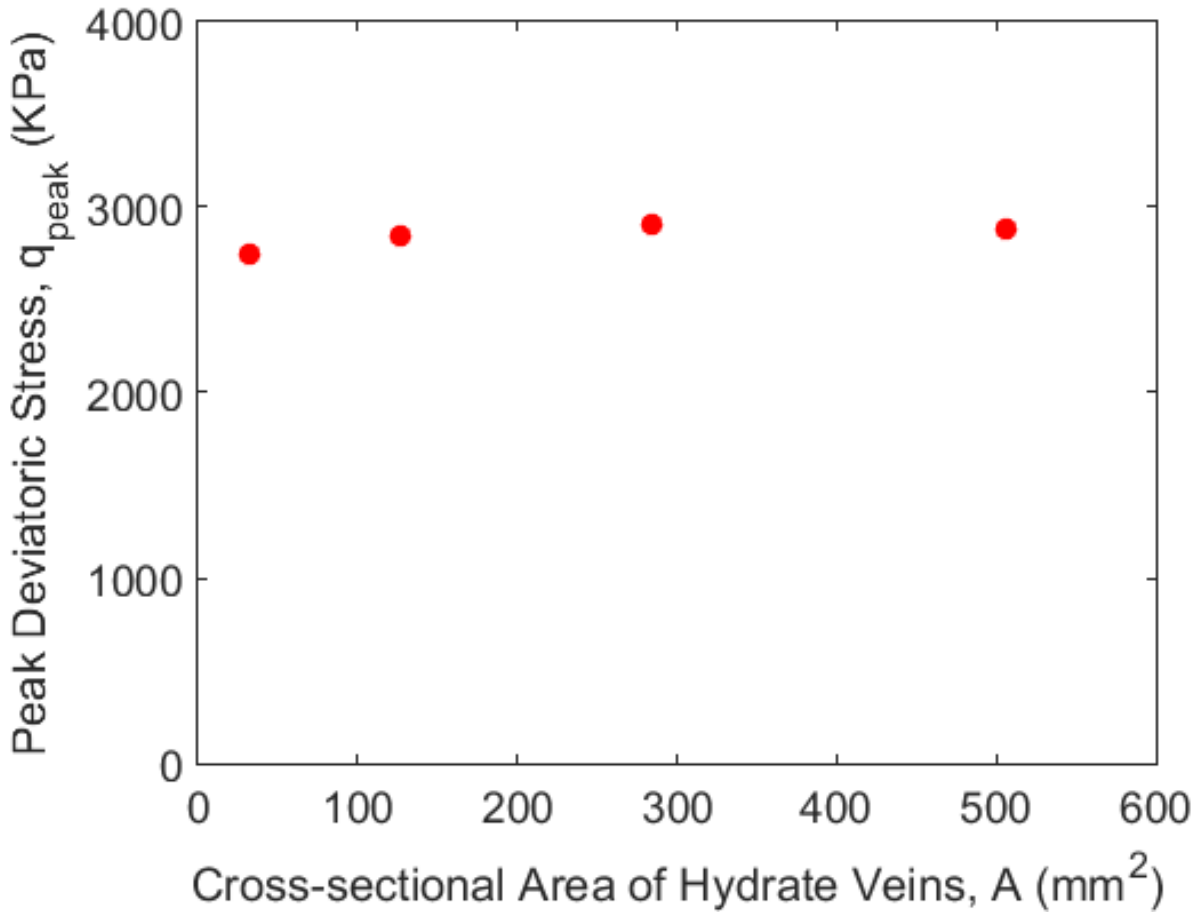

Figure 4.3: Peak stress applied to hydrate veins against cross-sectional area for the different hydrate veins.

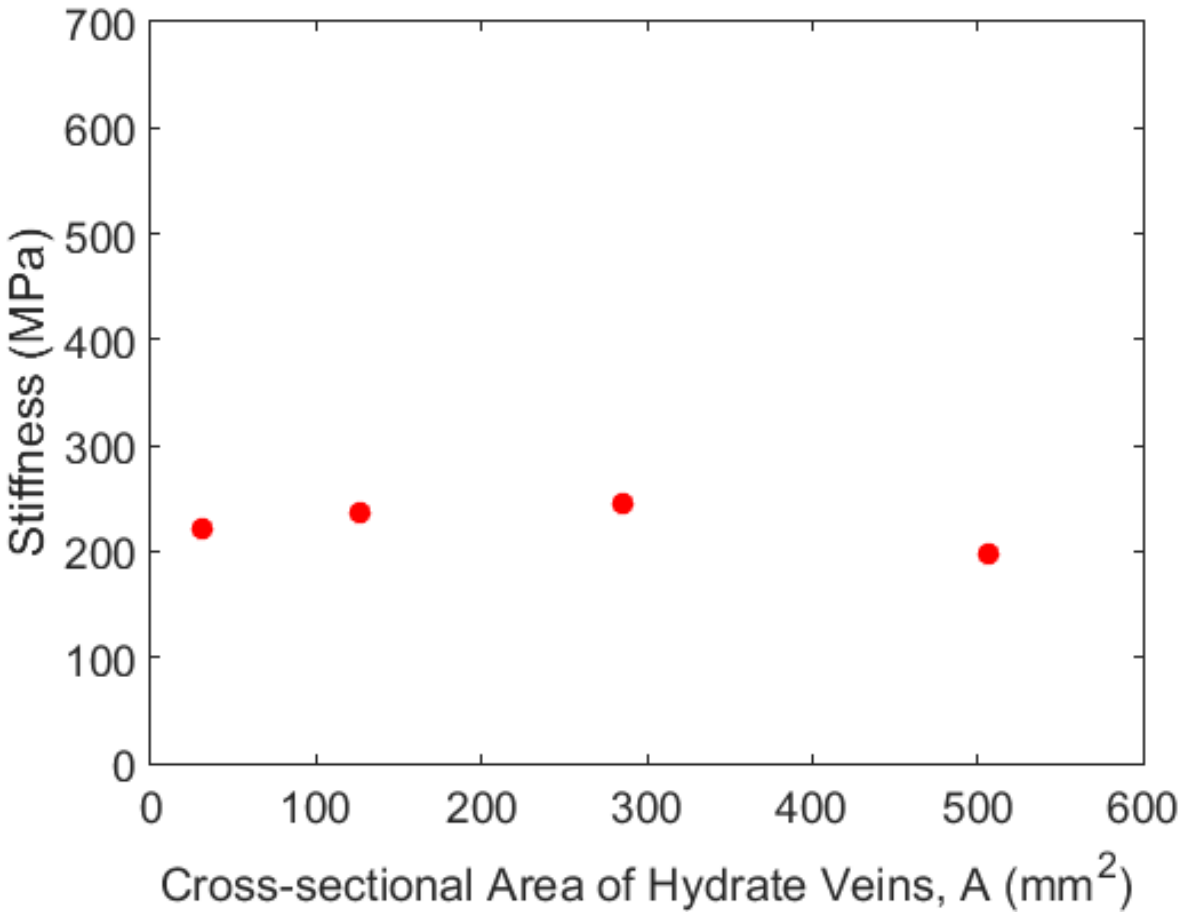

Figure 4.4: Stiffness of hydrate veins against cross-sectional area for the different hydrate veins.

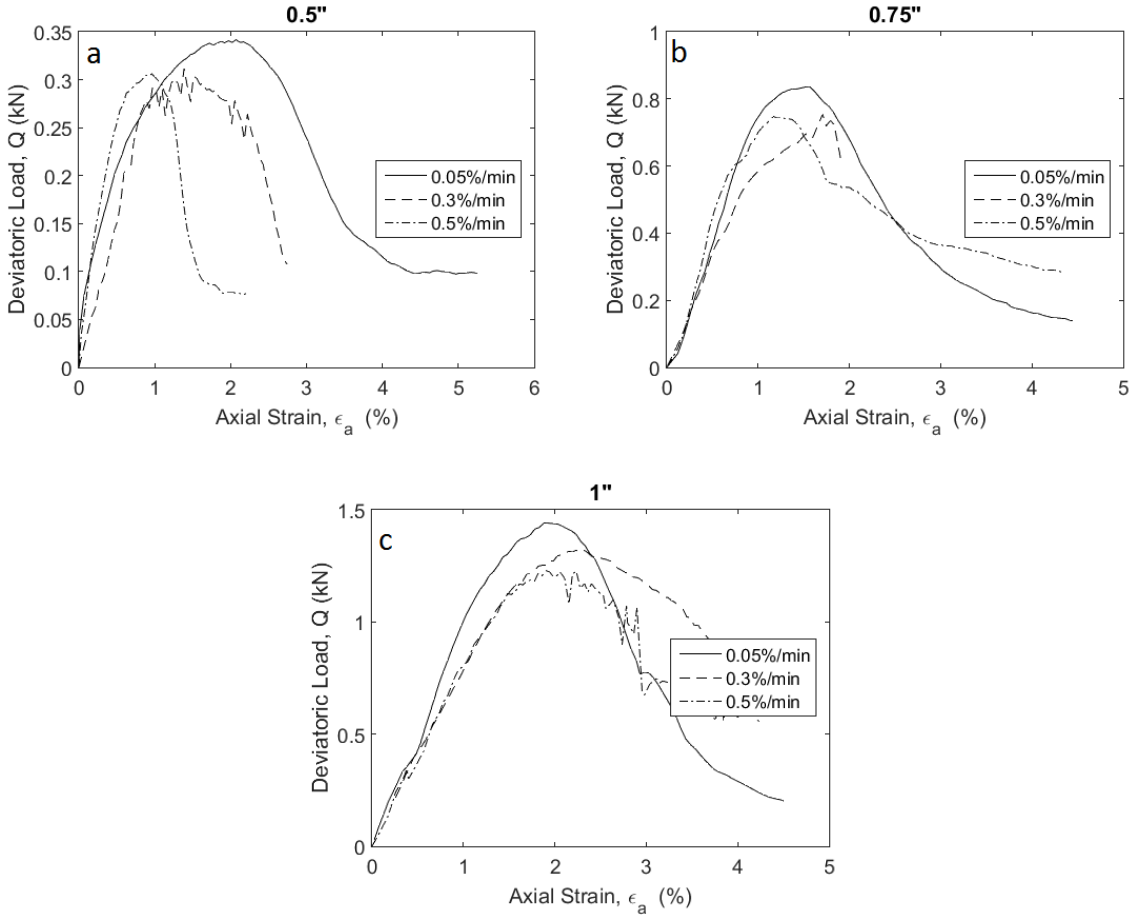

Figure 4.5: Deviatoric load against axial strain for hydrate vein specimens of (a) 0.5", (b) 0.75" and (c) 1" diameter subjected to different strain rates.

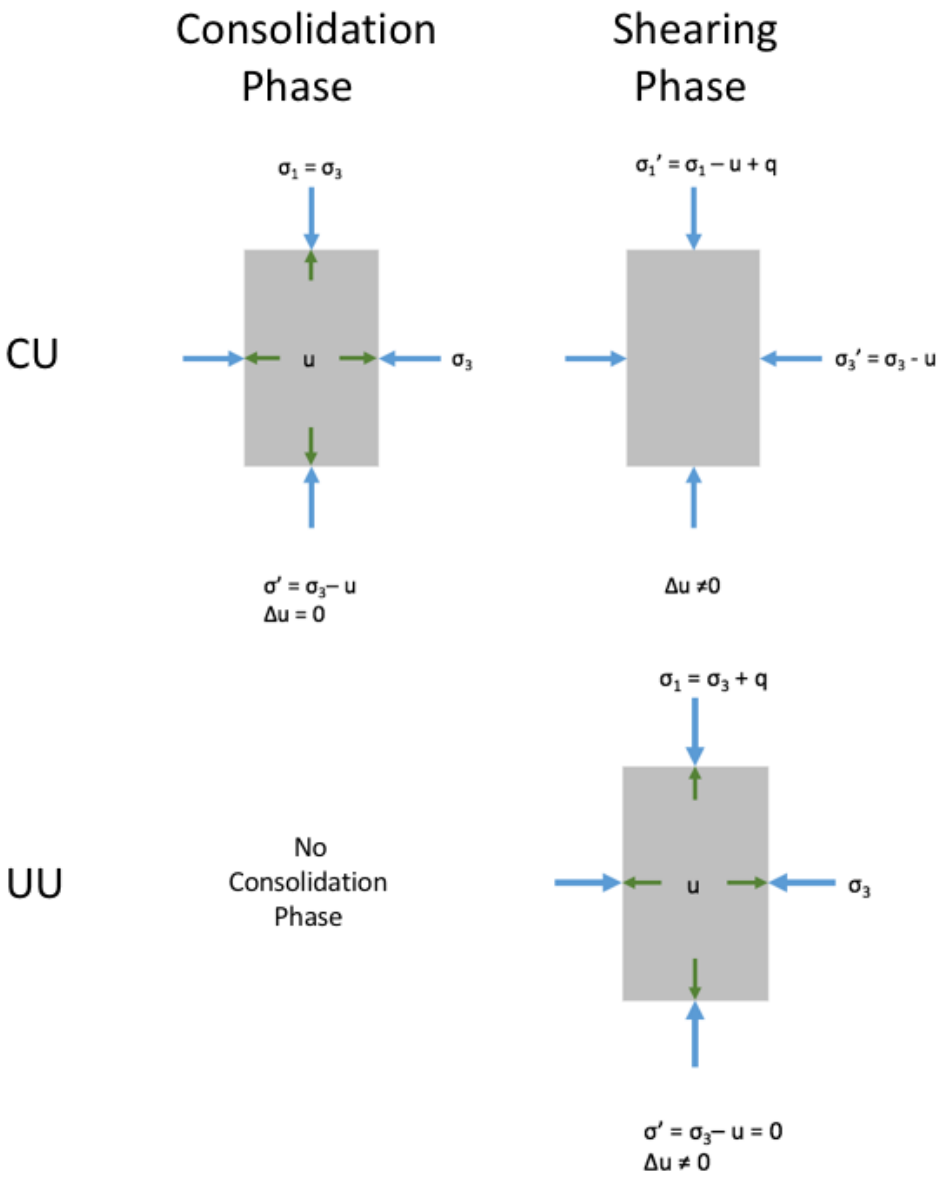

Figure 4.6: Schematic diagram showing the stress condition of CU and UU tests on soil specimens.

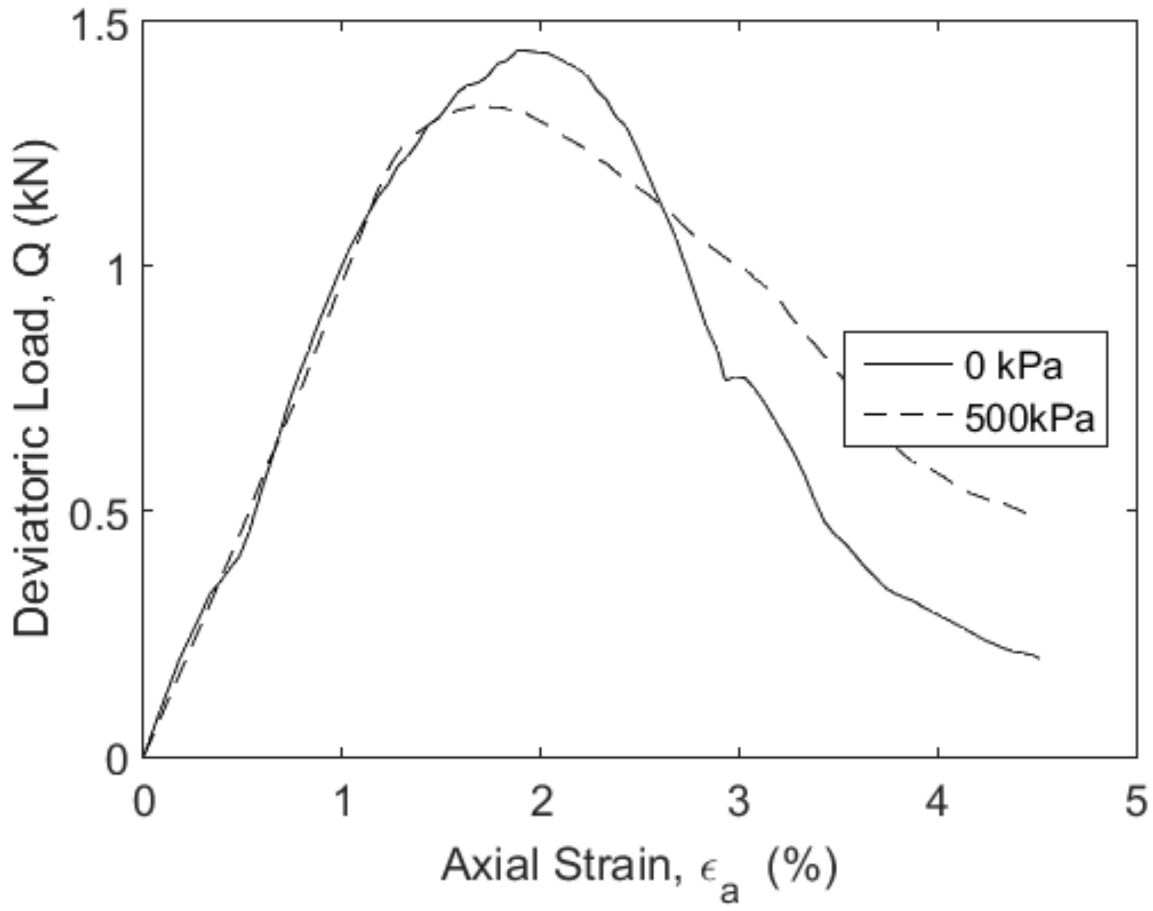

Figure 4.7: Deviatoric load against axial strain for 1”-diameter hydrate vein specimens under 0 kPa and 500 kPa confining pressure.

Figure 4.8: Image of 0.5”-diameter hydrate vein showing failure due to horizontal fracturing.

Figure 4.9: Image of 0.75”-diameter hydrate vein showing failure due to diagonal fracturing.

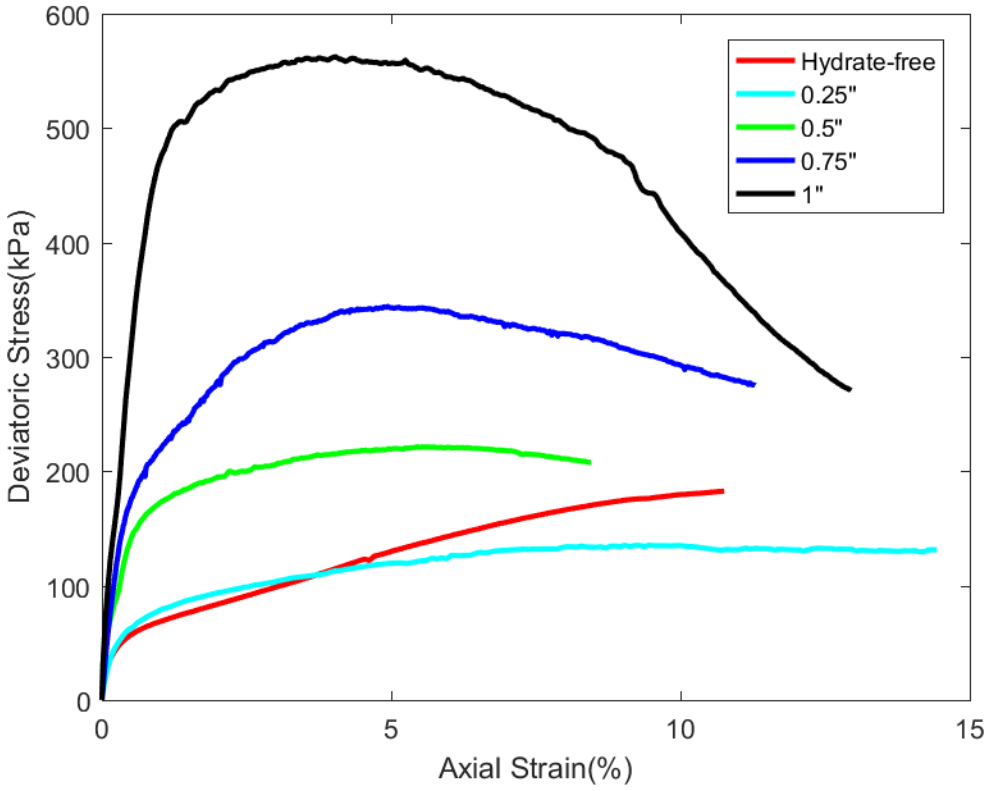

Figure 4.10: Stress-strain curves for hydrate-free and hydrate-bearing specimens under 100 kPa effective stress.

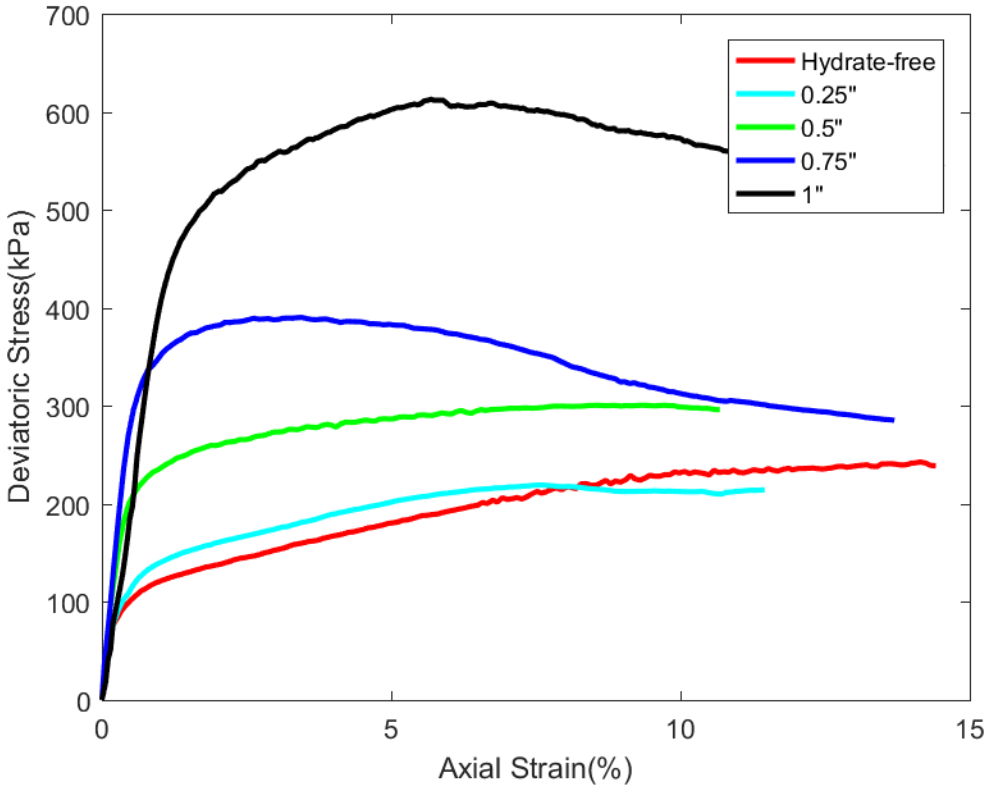

Figure 4.11: Stress-strain curves for hydrate-free and hydrate-bearing specimens under 200 kPa effective stress.

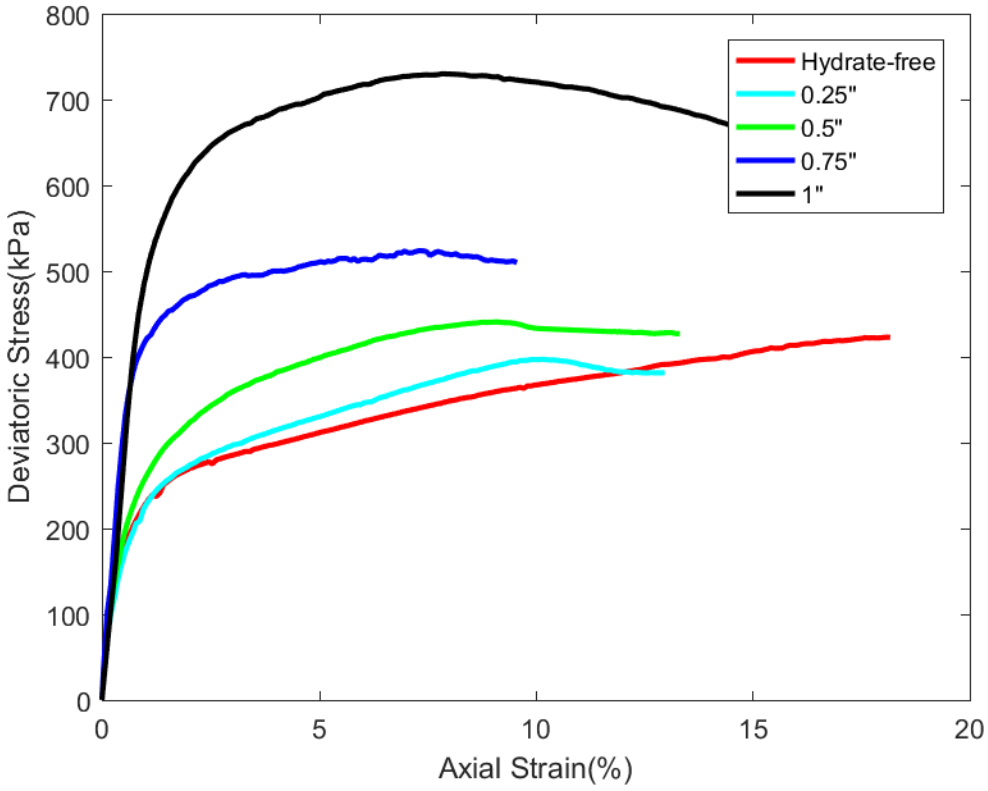

Figure 4.12: Stress-strain curves for hydrate-free and hydrate-bearing specimens under 400 kPa effective stress.

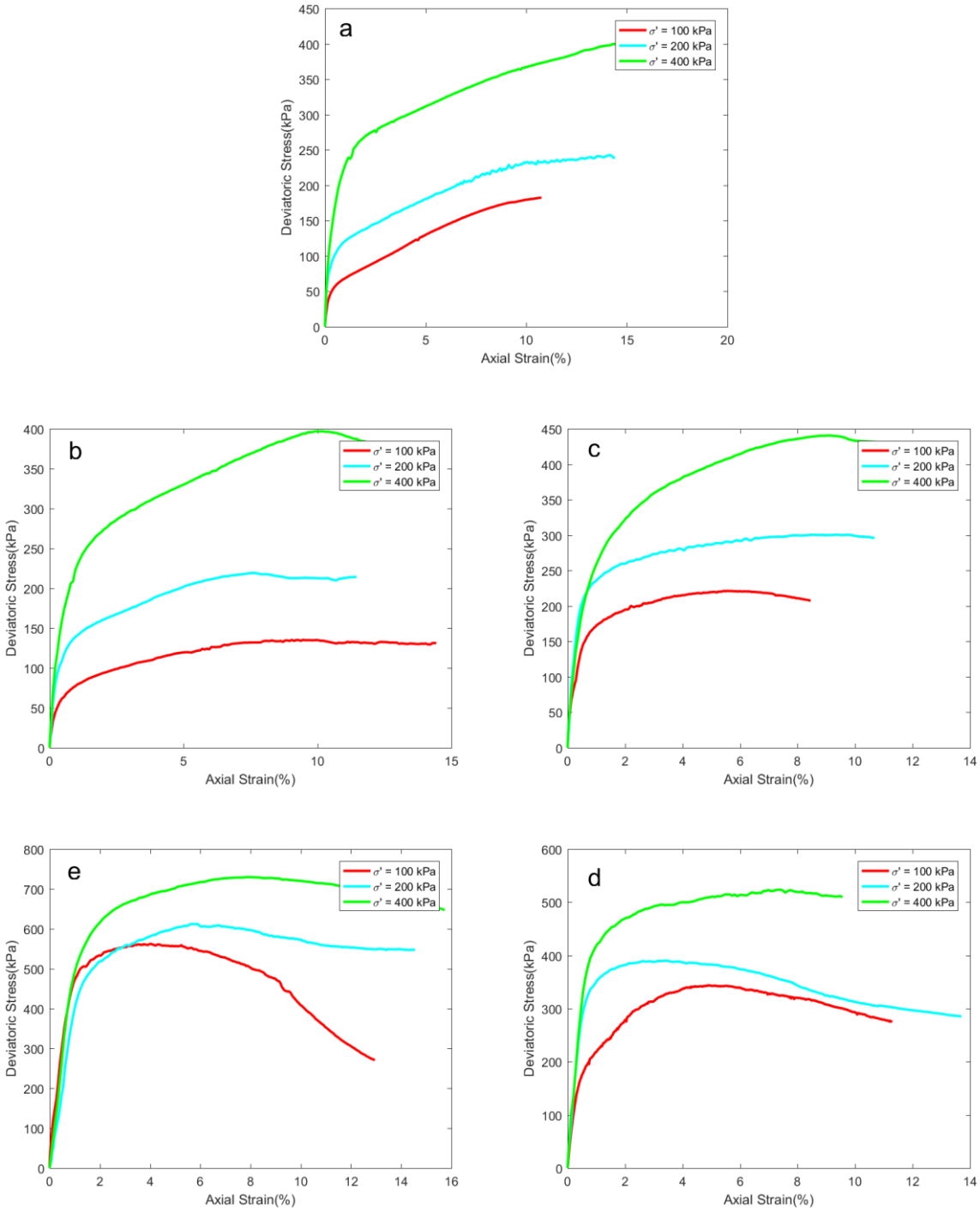

Figure 4.13: Stress-strain curves for fine-grained specimens containing (a) no veins, (b) 0.25”-diameter vein, (c) 0.5”-diameter vein, (d) 0.75”-diameter vein and (e) 1”-diameter vein under different effective stress (100, 200 and 400 kPa).

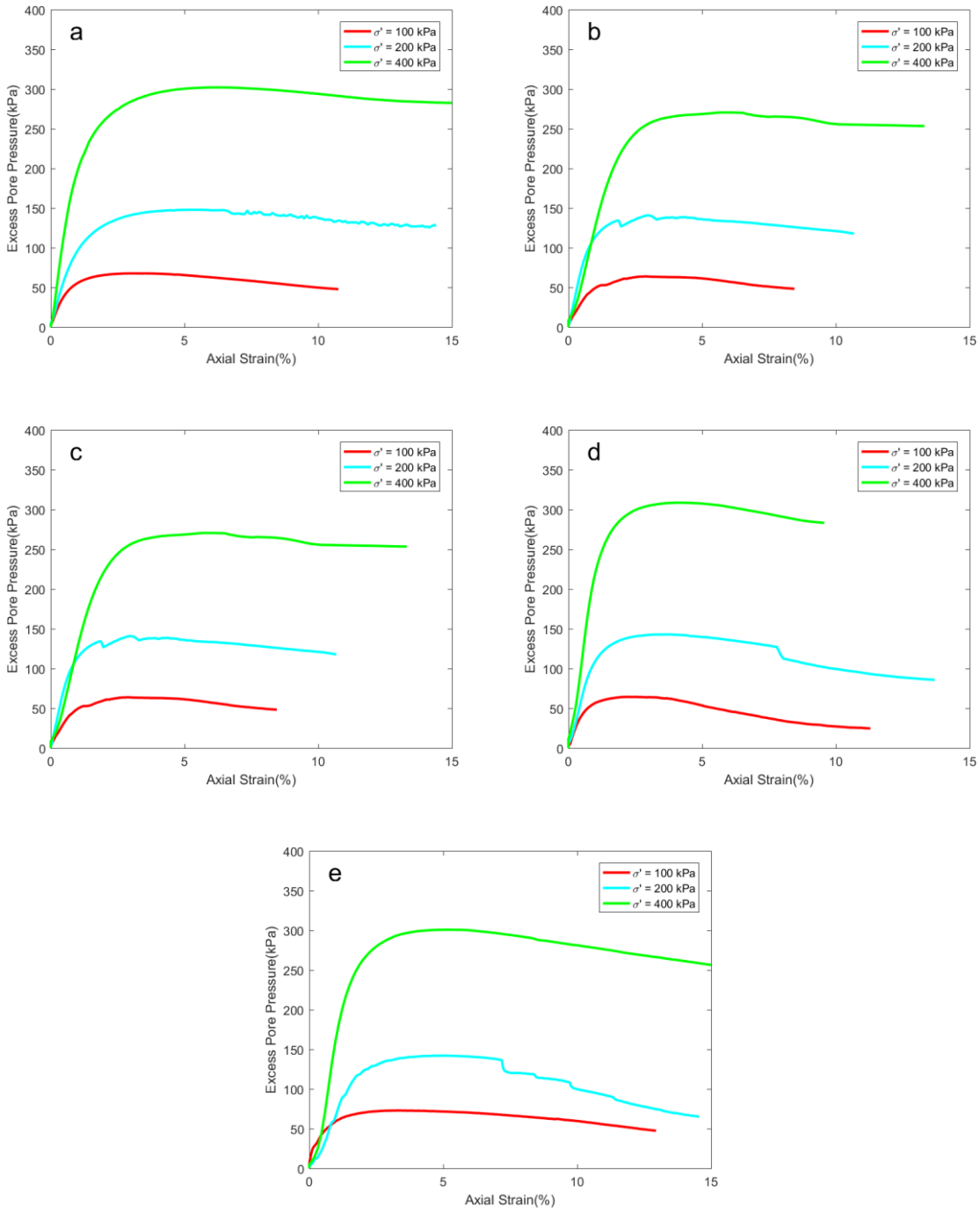

Figure 4.14: Excess pore pressure measured during loading within (a) hydrate-free sediments and hydrate-bearing sediments containing (b) 0.25”-diameter hydrate vein, (c) 0.5”-diameter hydrate vein, (d) 0.75”-diameter hydrate vein and (e) 1”-diameter hydrate vein under different effective stress (100, 200 and 400 kPa).

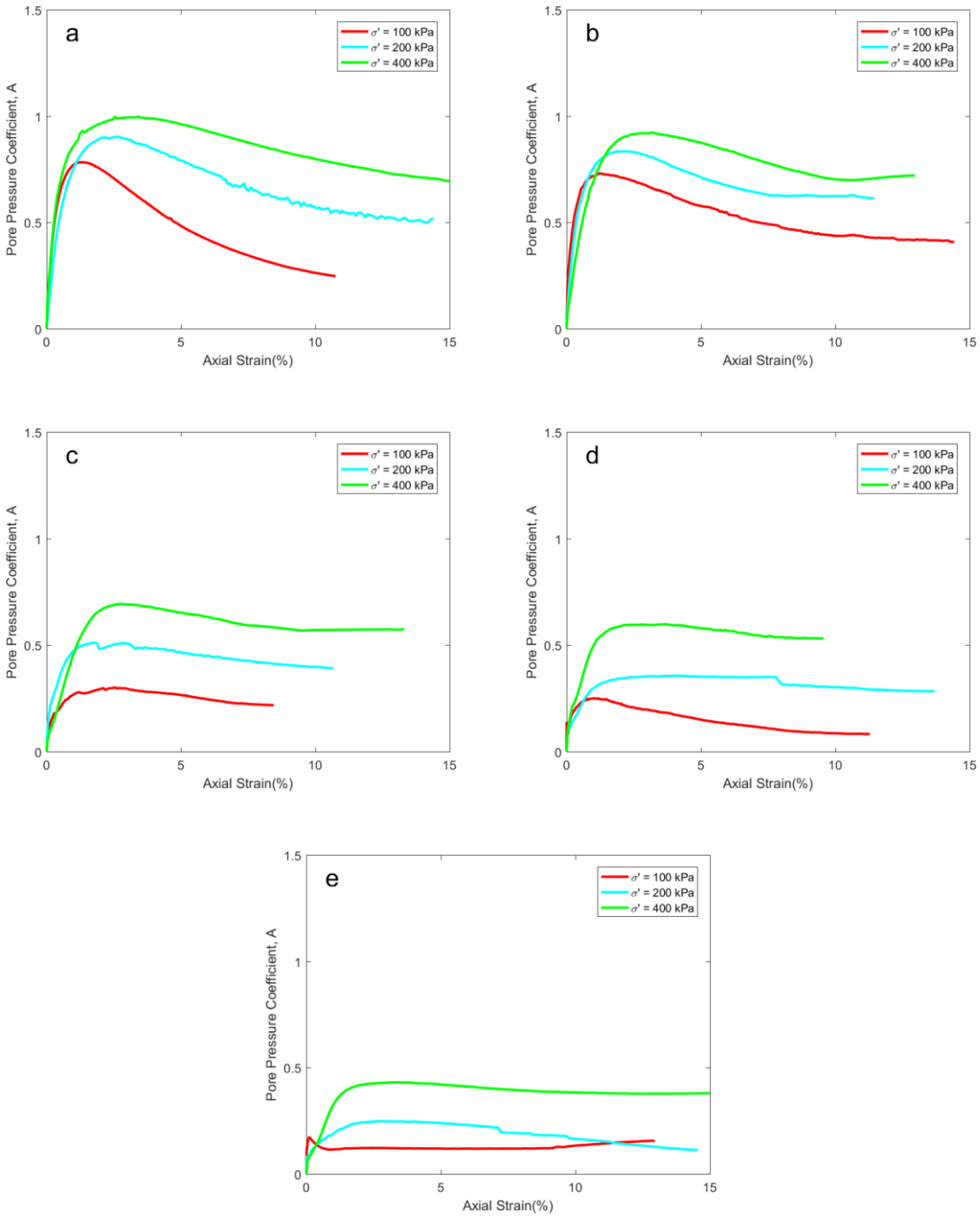

Figure 4.15: Pore pressure coefficient (A) calculated for (a) hydrate-free sediments and hydrate-bearing sediments containing (b) 0.25”-diameter hydrate vein, (c) 0.5”-diameter hydrate vein, (d) 0.75”-diameter hydrate vein and (e) 1”-diameter hydrate vein under different effective stress (100, 200 and 400 kPa).

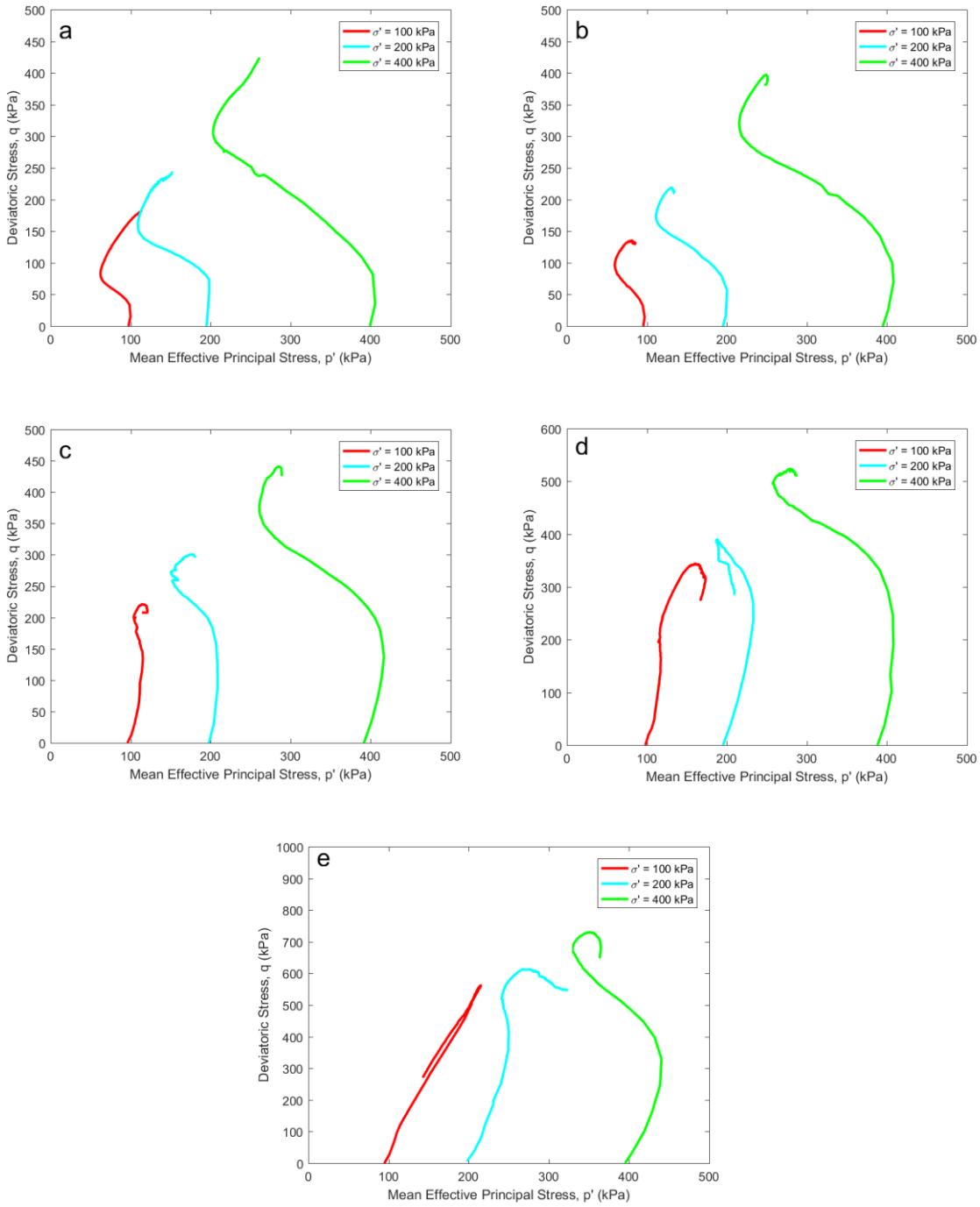

Figure 4.16: Effective stress path in q-p' space for (a) hydrate-free sediments and hydrate-bearing sediments containing (b) 0.25"-diameter hydrate vein, (c) 0.5"-diameter hydrate vein, (d) 0.75"-diameter hydrate vein and (e) 1"-diameter hydrate vein under different effective stress (100, 200 and 400 kPa).

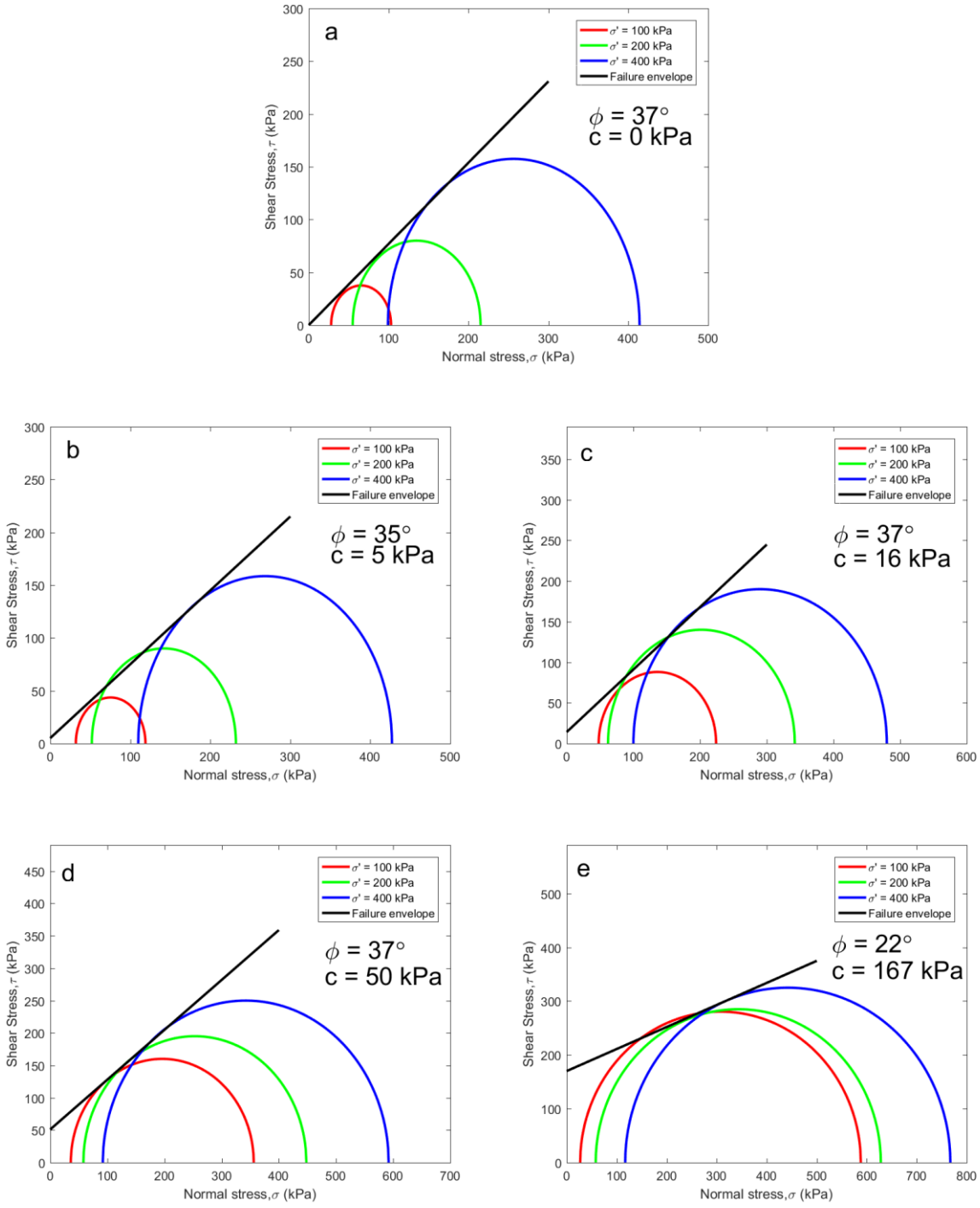

Figure 4.17: Mohr circles of stress, including Mohr-Coulomb failure lines for (a) hydrate-free sediments and hydrate-bearing sediments containing (b) 0.25”-diameter hydrate vein, (c) 0.5”-diameter hydrate vein, (d) 0.75”-diameter hydrate vein and (e) 1”-diameter hydrate vein.

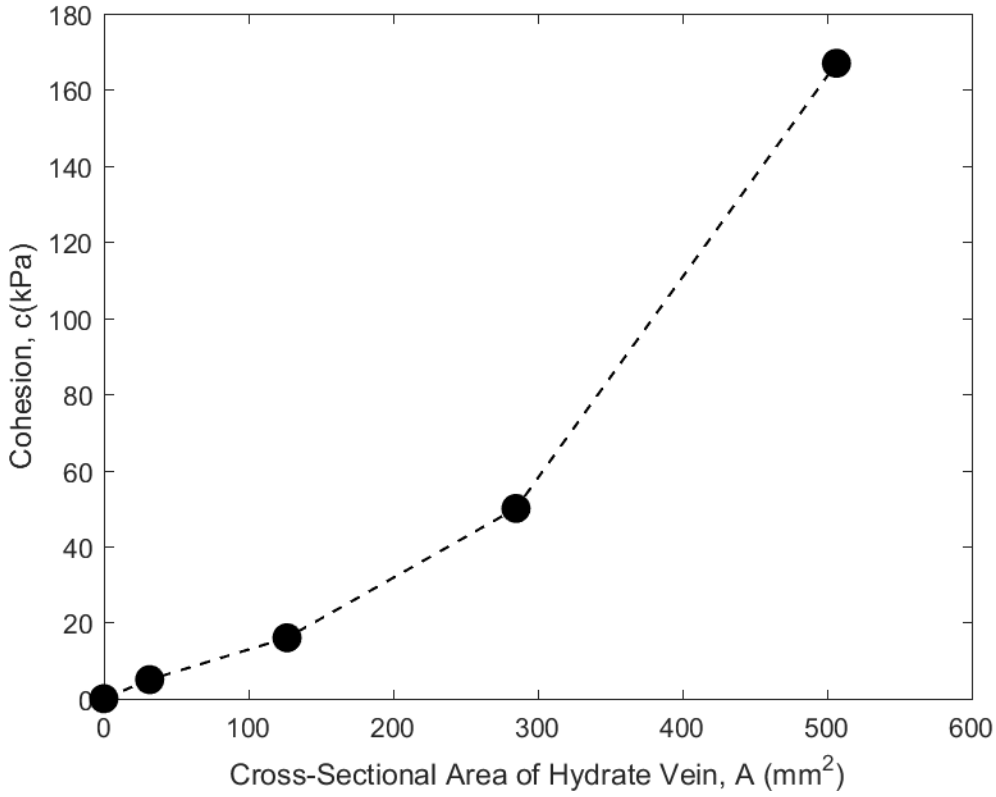

Figure 4.18: Values of cohesion derived from Mohr-Coulomb failure criteria for fine-grained specimens as a function of the cross-sectional area of hydrate vein within the fine-grained specimens.

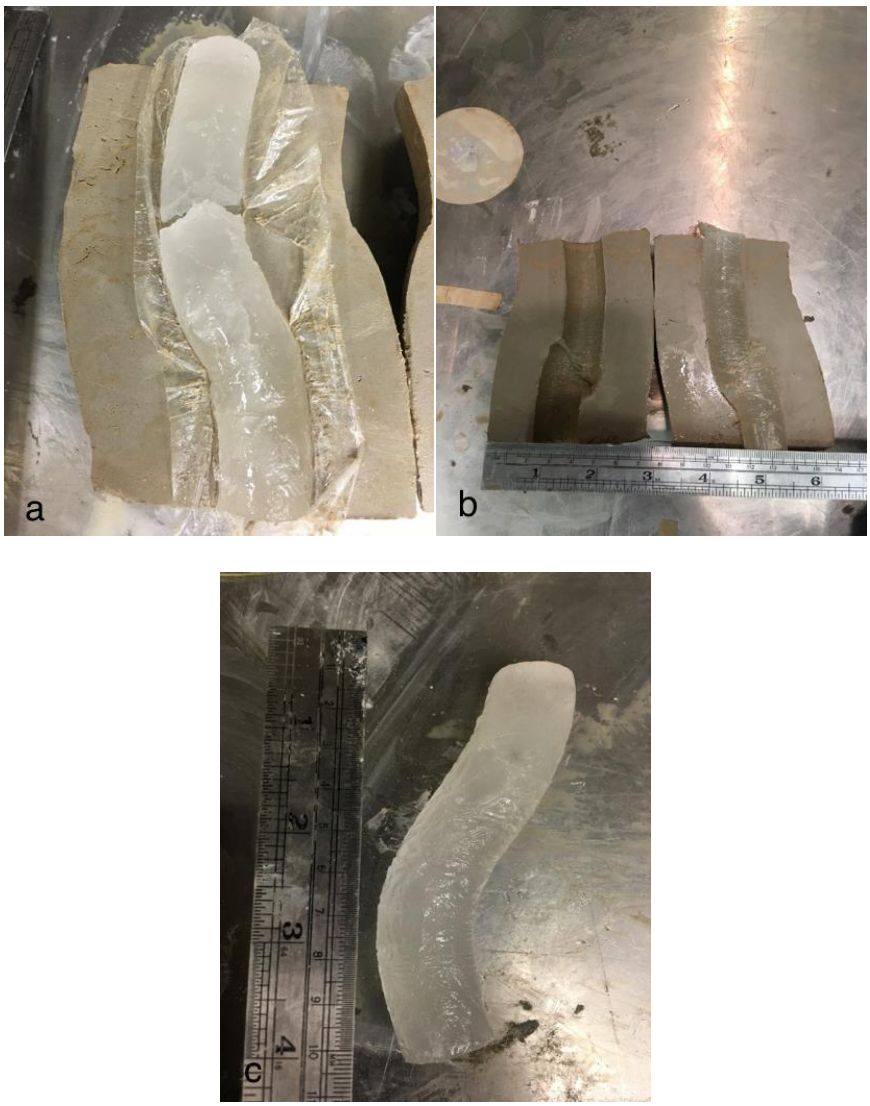

Figure 4.19: Examples of different failure modes of hydrate veins in hydrate-bearing specimens including (a) horizontal fracturing, (b) diagonal fracturing and (c) plastic creep failure.

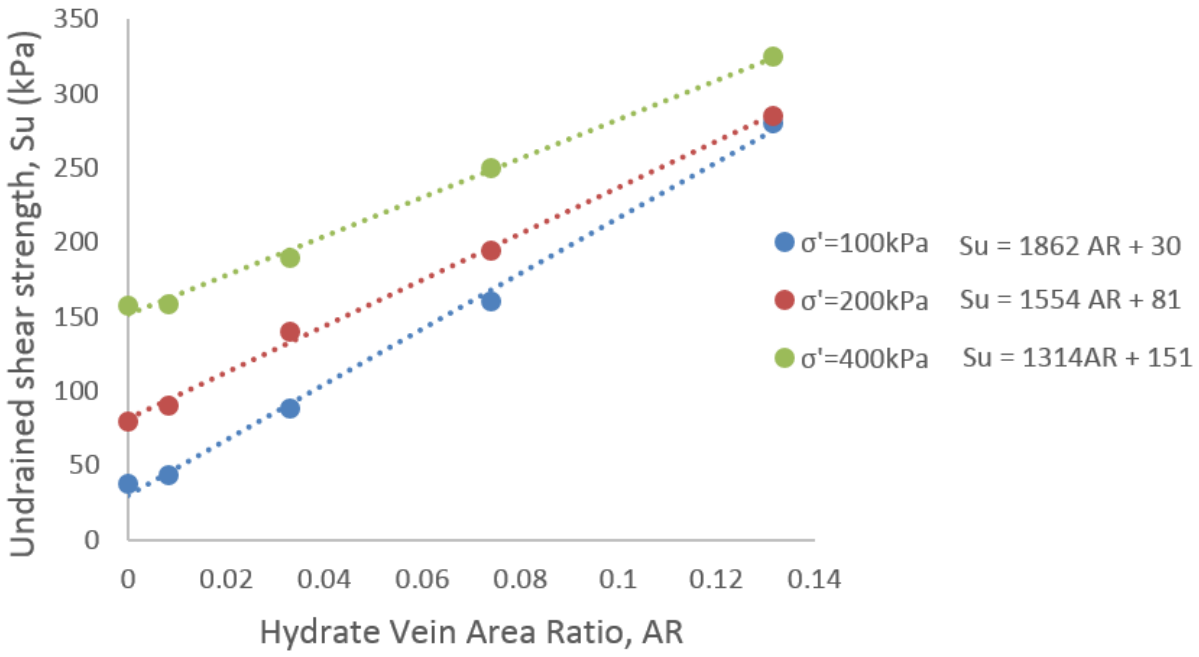

Figure 4.20: Undrained shear strength, Su as a function of hydrate vein area ratio for the specimens under different effective stress (100, 200 and 400 kPa).

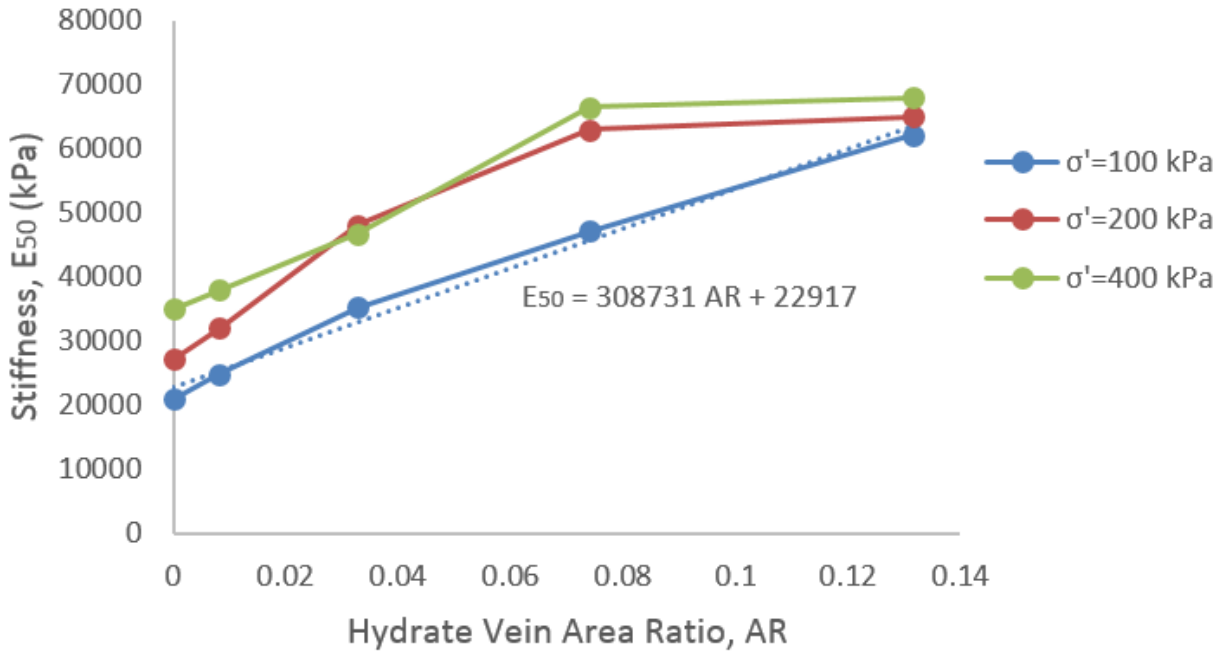

Figure 4.21: Stiffness, E_{50} as a function of hydrate vein area ratio for the specimens under different effective stresses (100, 200 and 400 kPa).

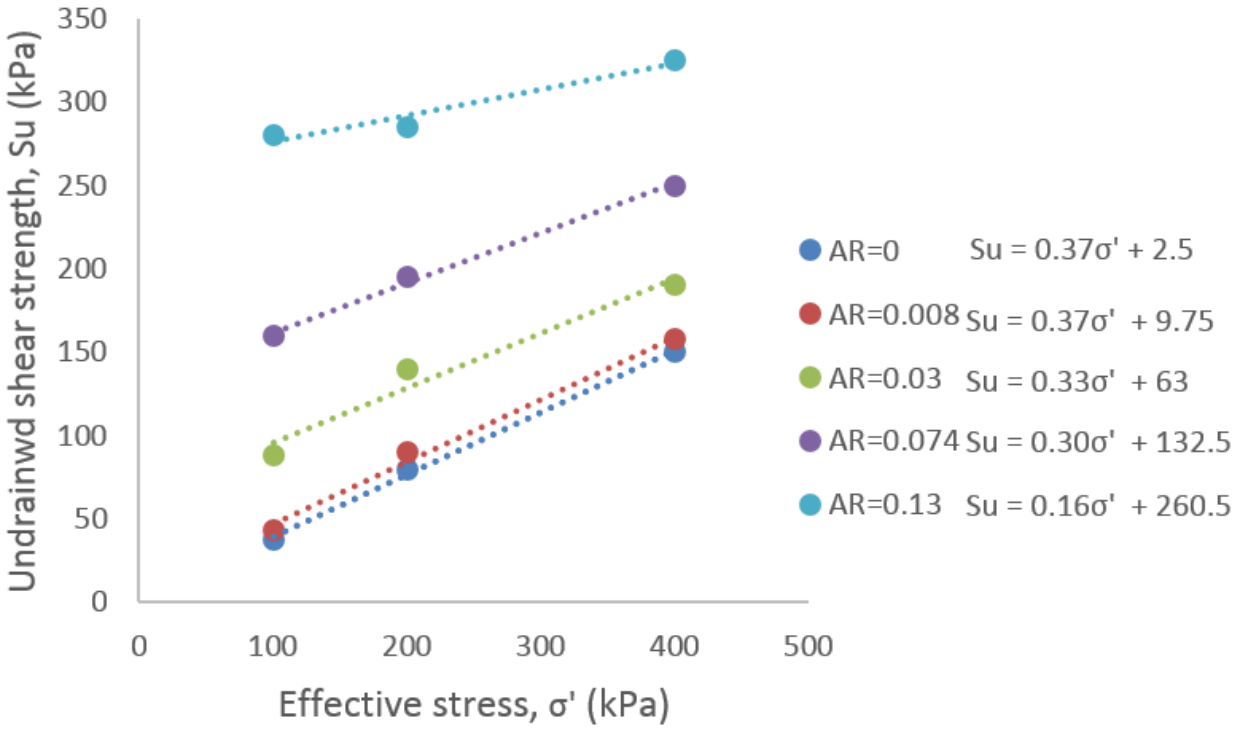

Figure 4.22: Undrained shear strength as a function of effective stress for the specimens with different hydrate vein area ratio.

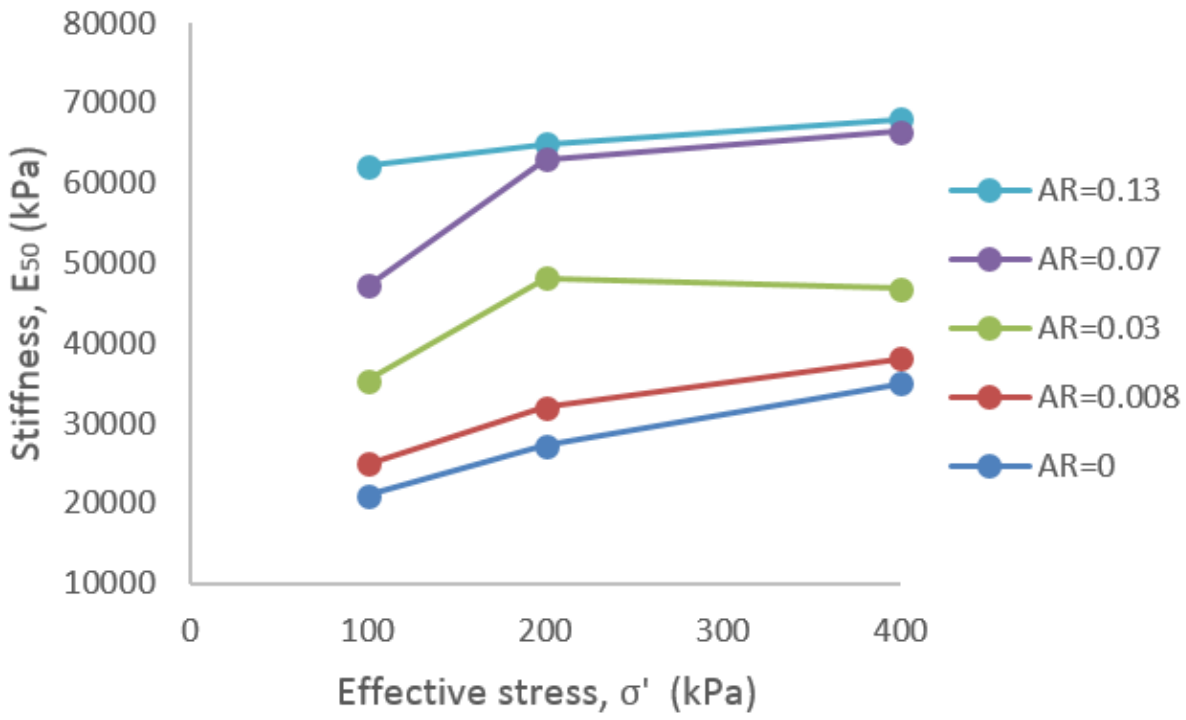

Figure 4.23: Stiffness as a function of hydrate vein area ratio for the specimens under different effective stresses (100, 200 and 400 kPa).

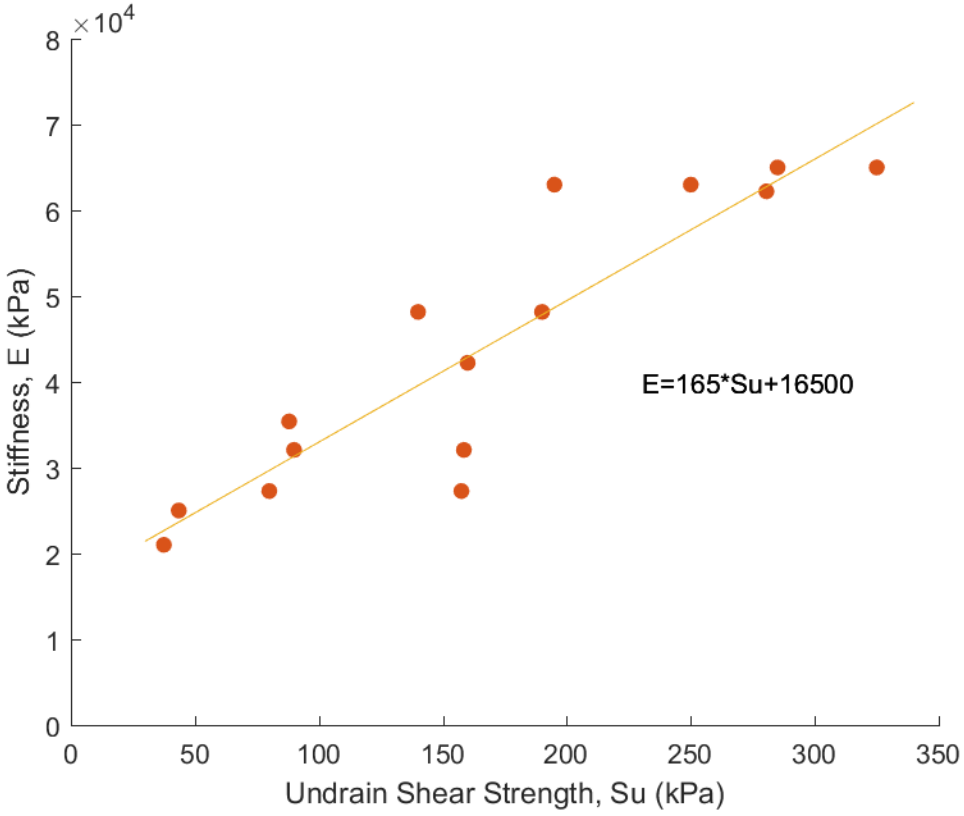

Figure 4.24: Correlation between undrained shear strength and stiffness of the hydrate-free and hydrate-bearing specimens.

Chapter Five: Conclusion

5.1 Overview

Assessing the impact of gas hydrate-bearing fine-grained sediments as a potential geohazards requires a detailed understanding of the influence of hydrate veins on the geomechanical behavior of the fine-grained sediments in which they reside.

The effect of hydrate veins on the behavior of fine-grained sediments is poorly understood (Chapter 2). To address this shortfall in our understanding a laboratory program was devised and applied to investigate the strength behavior of THF hydrate veins and hydrate-bearing fine-grained soil specimens (Chapter 3). The results of compression tests on THF hydrate veins and CU triaxial tests on hydrate-bearing soil specimens were analyzed to investigate the role of THF hydrate veins on the geomechanical behavior of hydrate-bearing fine-grained soils (Chapter 4).

5.2 Summary of laboratory program

The fine-grained soil used for this research program was prepared by consolidating a soil mixture of 65% silt and 35% clay. The dimension of the fine-grained soil specimen were 140 mm in height and 70 mm in diameter. Tetrahydrofuran (THF) was used to form standalone cylindrical hydrate veins of the same height as the soil specimens and with different diameters (0.25”, 0.5”, 0.75” and 1”). Hydrate-bearing fine-grained soil specimens were prepared by placing the pre-formed THF hydrate vein within pre-drilled voids, of the same dimensions, within the center of fine-grained soil specimen.

Initially, compression tests were carried out on standalone, cylindrical THF hydrate veins. Tests were conducted under strain control with continuous measurement of axial load and axial displacement. Different strain rates and confining pressures were considered to investigate their impact on the strength behavior of hydrate veins. Consolidated-undrained (CU) triaxial tests were then conducted on hydrate-free and hydrate-bearing fine-grained soil specimens to determine the strength and stress-strain behavior of cylindrical specimens. The specimens were consolidated to different effective stress condition (100, 200 and 400 kPa) during the consolidation phase prior to shearing at a constant shear rate (0.05%/min).

5.3 Conclusions

1. An improved laboratory THF hydrate vein formation technique was developed to prevent hydrate dissociation and dissolution during long-term tests. The THF hydrate vein were wrapped in a thin plastic wrap membrane to avoid direct contact between the THF hydrate vein and water. This significantly reduced any potential dissolution of the THF hydrate vein so that it remained stable during the long-term CU tests.

2. By carrying out axial compression tests on standalone cylindrical THF hydrate veins of different sizes it was shown that although the deviatoric load carried by hydrate veins increased with vein diameter, the peak strength and stiffness of the different hydrate veins were comparable. The results also showed that factors such as strain rate, confining pressure and failure modes of hydrate veins had no appreciable effect on stress-strain behavior of hydrate veins. The results were of tremendous value to help understand and quantify the impact of hydrate veins on the geomechanical behavior of hydrate-bearing fine-grained sediments.

3. By carrying out CU tests on hydrate-free and hydrate-bearing fine-grained soils, the stress-strain behavior of the respective fine-grained soil specimens were investigated. The results were analyzed to investigate the impact of hydrate vein size and effective stress on the undrained shear strength and stiffness of the specimens. Both undrained shear strength and stiffness were observed to increase with hydrate vein size and effective stress. In considering the behaviour of the specimens with respect to the Mohr-Coulomb failure criteria the increased strength of hydrate-bearing soils was mainly due to an apparent increase in cohesion from the hydrate vein.

4. The pore pressure response from CU tests is dominated by the change in effective stress while appears to be independent of hydrate vein size. In contrast, the pore pressure coefficient, A is significantly influenced by vein size. The specimen without hydrate and those with small vein diameters, that A displays an early peak, indicating compression of the sample and then decreases as the soil dilates with increasing strain. It can be seen that as σ' increases the post peak reduction is somewhat muted. At higher vein diameters the increased hydrate vein diameter is capable of carrying the higher deviatoric stresses, and therefore not fully felt by the soil before failure of the vein and the sediment. As such the increase in σ' is also muted.

5. The presence of hydrate vein reduces the pore pressure response of the host sediments, and allows the sediments to withstand higher deviatoric stress conditions that lead to identifiable peak stresses at failure such that the specimens exceed the critical state line of the soil. After reaching the peak deviatoric stress, the stress path of hydrate-bearing specimen falls back to the critical state line of the sediments. This indicates that the presence of hydrate vein influences the

post-peak behavior of the fine-grained sediments. Once failure occurs the specimen strength is quickly reduced and may reach the critical state line.

6. The observed behaviour from CU tests suggest the depth at which the hydrate veins form may have a significant impact on sediment failure assessment. The formation of hydrate veins at shallow depths will hinder ongoing consolidation processes. At greater depths, the impact of hydrate veins on soil strength will be less marked. Therefore, current warming trends especially in the Arctic are likely to lead to near surface sediments warming, and thus the reduced sediment strength where hydrate is present may lead to slope instability if the hydrate were to dissociate.

7. If the hydrate veins are hosted within the soft and under-consolidated soil, the relationship between geomechanical behavior of the hydrate-bearing sediments and hydrate vein area ratio under low effective stress shown in Figure 4.20 and 4.21 can be used to predict the strength and stiffness of the hydrate-bearing fine-grained sediments in terms of known hydrate vein area ratio. If the fine-grained soil around the hydrate vein is consolidated to a significant effective confining stress due to the sediment overburden prior to hydrate formation, the results of CU tests under different effective stress shown in Figure 4.22 and 4.23 may be useful to predict the geomechanical behavior of hydrate-bearing fine-grained sediments.

5.4 Recommendations

1. The present study considered cylindrical simplified veins, however more representative hydrate vein morphology needs to be considered, such as different orientation, shape and location within the fine-grained sediments to better mimic that observed in nature.

2. The impact of hydrate dissociation on hydrate-bearing fine-grained soil behavior needs to be investigated. Understanding the response to a change in strength and stiffness of fine-grained sediments after the hydrate vein dissociate is required to better assess soil instability.

3. More detailed investigations are required to understand the creep behavior of hydrate veins within fine-grained sediments. It was shown that under loading THF veins could exhibit plastic deformation, and therefore the long-term consolidation of fine-grained soil may not be hampered as much as suggested. Therefore, understanding the long-term deformation of hydrate veins is required for better understanding long-term sediment instability.

Bibliography

ASTM Standard D4767, 2011. Standard test method for consolidated undrained triaxial compression test for cohesive soils. doi:10.1520/D4767-11

Bahk, J.-J., Kim, J.-H., Kong, G.-S., Park, Y., Lee, H., Park, Y., & Park, K. P. (2009). Occurrence of near-seafloor gas hydrates and associated cold vents in the Ulleung Basin, East Sea. *Geosciences Journal*, *13*(4), 371-385.

Bathe, M., Vagle, S., Saunders, G., & Lambson, E. (1984). Ultrasonic wave velocities in the structure II clathrate hydrate THF· 17H 2 O. *Journal of materials science letters*, *3*(10), 904-906.

Boswell, R., & Collett, T. (2006). The gas hydrates resource pyramid. *Natural Gas & Oil, 304*, 285-4541.

Boswell, R., & Collett, T. S. (2011). Current perspectives on gas hydrate resources. *Energy & environmental science*, *4*(4), 1206-1215.

Brewer, P. G., Orr, F. M., Friederich, G., Kvenvolden, K. A., & Orange, D. L. (1998). Gas hydrate formation in the deep sea: In situ experiments with controlled release of methane, natural gas, and carbon dioxide. *Energy & Fuels*, *12*(1), 183-188.

Clennell, M. B., Hovland, M., Booth, J. S., Henry, P., & Winters, W. J. (1999). Formation of natural gas hydrates in marine sediments: 1. Conceptual model of gas hydrate growth conditioned by host sediment properties. *Journal of Geophysical Research: Solid Earth (1978–2012)*, *104*(B10), 22985-23003.

Collett, T. S. (1993). Natural gas hydrates of the Prudhoe Bay and Kuparuk River area, north slope, Alaska. *AAPG bulletin*, *77*(5), 793-812.

Collett, T. S., & Dallimore, S. R. (1999). Hydrocarbon gases associated with permafrost in the

Mackenzie Delta, Northwest Territories, Canada. *Applied geochemistry, 14*(5), 607-620.

Collett, T. S., Johnson, A. H., Knapp, C. C., & Boswell, R. (2009). Natural gas hydrates: a review.

Collett, T. S., Riedel, M., Cochran, J. R., Boswell, R., Kumar, P., & Sathe, A. (2008). Indian continental margin gas hydrate prospects: results of the Indian National Gas Hydrate Program (NGHP) expedition 01.

Cook, A. E., Goldberg, D., & Kleinberg, R. L. (2008). Fracture-controlled gas hydrate systems in the northern Gulf of Mexico. *Marine and Petroleum Geology, 25*(9), 932-941.

Ebinuma, T., Kamata, Y., Minagawa, H., Ohmura, R., Nagao, J., & Narita, H. (2005). *Mechanical properties of sandy sediment containing methane hydrate.* Paper presented at the Proceedings of Fifth International Conference on Gas Hydrates, Pap.

Gough, S., & Davidson, D. (1971). Composition of tetrahydrofuran hydrate and the effect of pressure on the decomposition. *Canadian Journal of Chemistry, 49*(16), 2691-2699.

Grozic, J. (2010). Interplay between gas hydrates and submarine slope failure *Submarine mass movements and their consequences* (pp. 11-30): Springer.

Haq, B. (1998). Natural gas hydrates: searching for the long-term climatic and slope-stability records. *Geological Society, London, Special Publications, 137*(1), 303-318.

Kayen, R. E., & Lee, H. J. (1991). Pleistocene slope instability of gas hydrate-laden sediment on the Beaufort sea margin. *Marine Georesources & Geotechnology, 10*(1-2), 125-141.

Kim, G. Y., Yi, B. Y., Yoo, D. G., Ryu, B. J., & Riedel, M. (2011). Evidence of gas hydrate from downhole logging data in the Ulleung Basin, East Sea. *Marine and Petroleum Geology, 28*(10), 1979-1985.

Kim, H.-S., Cho, G.-C., Lee, J. Y., & Kim, S.-J. (2013). Geotechnical and geophysical properties

of deep marine fine-grained sediments recovered during the second Ulleung Basin Gas Hydrate expedition, East Sea, Korea. *Marine and Petroleum Geology, 47,* 56-65.

Kim, H. S., Cho, G. C., & Kwon, T. H. (2013). Effect of CO2 hydrate formation on seismic wave velocities of fine-grained sediments. *Geochemistry, Geophysics, Geosystems, 14*(6), 1787-1799.

Kvenvolden, K. A. (1993). Gas hydrates—geological perspective and global change. *Reviews of Geophysics, 31*(2), 173-187.

Kwon, T.-H., Song, K.-I., & Cho, G.-C. (2010). Destabilization of marine gas hydrate-bearing sediments induced by a hot wellbore: A numerical approach. *Energy & Fuels, 24*(10), 5493-5507.

Kwon, T. H., Cho, G. C., & Santamarina, J. C. (2008). Gas hydrate dissociation in sediments: Pressure-temperature evolution. *Geochemistry, Geophysics, Geosystems, 9*(3).

Lee, J., Francisca, F. M., Santamarina, J. C., & Ruppel, C. (2010). Parametric study of the physical properties of hydrate-bearing sand, silt, and clay sediments: 2. Small-strain mechanical properties. *Journal of Geophysical Research: Solid Earth (1978–2012), 115*(B11).

Lee, J., Santamarina, J., & Ruppel, C. (2008). Mechanical and electromagnetic properties of northern Gulf of Mexico sediments with and without THF hydrates. *Marine and Petroleum Geology, 25*(9), 884-895.

Lee, J., Santamarina, J. C., & Ruppel, C. (2010). Volume change associated with formation and dissociation of hydrate in sediment. *Geochemistry, Geophysics, Geosystems, 11*(3).

Lee, J., Santamarina, J. C., & Ruppel, C. (2010). Parametric study of the physical properties of hydrate-bearing sand, silt, and clay sediments: 1. Electromagnetic properties. *Journal of*

Geophysical Research: Solid Earth (1978–2012), 115(B11).

Lee, J., Yun, T., Santamarina, J., & Ruppel, C. (2007). Observations related to tetrahydrofuran and methane hydrates for laboratory studies of hydrate-bearing sediments. *Geochemistry, Geophysics, Geosystems, 8*(6).

Li, Y., Song, Y., Liu, W., Yu, F., Wang, R., & Nie, X. (2012). Analysis of mechanical properties and strength criteria of methane hydrate-bearing sediments. *International Journal of Offshore and Polar Engineering, 22*(4), 290-296.

Li, Y.-h., Song, Y.-c., Yu, F., Liu, W.-g., & Zhao, J.-f. (2011). Experimental study on mechanical properties of gas hydrate-bearing sediments using kaolin clay. *China Ocean Engineering, 25*, 113-122.

Makogon, I. U. r. F. (1981). *Hydrates of natural gas*: PennWell Books Tulsa, Okla, USA.

Masui, A., Haneda, H., Ogata, Y., & Aoki, K. (2005). *The effect of saturation degree of methane hydrate on the shear strength of synthetic methane hydrate sediments.* Paper presented at the Proceedings of the 5th International Conference on Gas Hydrates, Trondheim, Norway.

Nimblett, J., Shipp, R., & Strijbos, F. (2005). *Gas hydrate as a drilling hazard: examples from global deepwater settings.* Paper presented at the Offshore Technology Conference.

Priest, J. A., Best, A. I., & Clayton, C. R. (2005). A laboratory investigation into the seismic velocities of methane gas hydrate-bearing sand. *Journal of Geophysical Research: Solid Earth (1978–2012), 110*(B4).

Priest, J. A., Clayton, C. R., & Rees, E. V. (2014). Potential impact of gas hydrate and its dissociation on the strength of host sediment in the Krishna–Godavari Basin. *Marine and Petroleum Geology, 58*, 187-198.

Priest, J. A., Rees, E. V., & Clayton, C. R. (2009). Influence of gas hydrate morphology on the seismic velocities of sands. *Journal of Geophysical Research: Solid Earth (1978–2012), 114*(B11).

Rees, E. V., Priest, J. A., & Clayton, C. R. (2011). The structure of methane gas hydrate bearing sediments from the Krishna–Godavari Basin as seen from Micro-CT scanning. *Marine and Petroleum Geology, 28*(7), 1283-1293.

Ruppel, C. (1997). Anomalously cold temperatures observed at the base of the gas hydrate stability zone on the US Atlantic passive margin. *Geology, 25*(8), 699-702.

Scherer, G. W. (1993). Freezing gels. *Journal of Non-Crystalline Solids, 155*(1), 1-25.

Schultheiss, P., Francis, T., Holland, M., Roberts, J., Amann, H., Parkes, R., . . . Jackson, P. (2006). Pressure coring, logging and subsampling with the HYACINTH system. *Geological Society, London, Special Publications, 267*(1), 151-163.

Schultheiss, P., Holland, M., & Humphreys, G. (2008). *Borehole pressure coring and laboratory pressure core analysis for gas hydrate investigations.* Paper presented at the Offshore Technology Conference, Houston, Tex.

Skempton, A. (1954). The pore-pressure coefficients A and B. *Geotechnique, 4*(4), 143-147.

Sloan, E. D. (1998). Gas hydrates: review of physical/chemical properties. *Energy & Fuels, 12*(2), 191-196.

Sloan Jr, E., & Koh, C. A. (2008). Clathrate Hydrates of Natural Gases, Vol. 119. Boca Raton, Florida: Chemical Industries: CRC Press.

Smith, W.E. (2016). The Influence of Tetrahydrofuran Hydrate Veins on Fine-Grained Soil Behaviour (Master dissertation, University of Calgray).

Spangenberg, E., Kulenkampff, J., Naumann, R., & Erzinger, J. (2005). Pore space hydrate

formation in a glass bead sample from methane dissolved in water. *Geophysical Research Letters, 32*(24).

Stern, L. A., Kirby, S. H., & Durham, W. B. (1996). Peculiarities of methane clathrate hydrate formation and solid-state deformation, including possible superheating of water ice. *Science, 273*(5283), 1843.

Stoll, R. D., & Bryan, G. M. (1979). Physical properties of sediments containing gas hydrates. *Journal of Geophysical Research: Solid Earth, 84*(B4), 1629-1634.

Sultan, N., Cochonat, P., Canals, M., Cattaneo, A., Dennielou, B., Haflidason, H., . . . Trincardi, F. (2004). Triggering mechanisms of slope instability processes and sediment failures on continental margins: a geotechnical approach. *Marine Geology, 213*(1), 291-321.

Sultan, N., Voisset, M., Marsset, T., Vernant, A.-M., Cauquil, E., Colliat, J., & Curinier, V. (2007). Detection of free gas and gas hydrate based on 3D seismic data and cone penetration testing: An example from the Nigerian Continental Slope. *Marine Geology, 240*(1), 235-255.

Waite, W. F., Santamarina, J. C., Cortes, D. D., Dugan, B., Espinoza, D., Germaine, J., . . . Shin, H. (2009). Physical properties of hydrate-bearing sediments. *Reviews of Geophysics, 47*(4).

Waite, W. F., Santamarina, J. C., Cortes, D. D., Dugan, B., Espinoza, D., Germaine, J., . . . Shin, H. (2009). Physical properties of hydrate-bearing sediments. *Reviews of Geophysics, 47*(4).

Winters, W. (1999). Properties of samples containing natural gas hydrate from the JAPEX/JNOC/GSC Mallik 2L-38 gas hydrate research well, determined using Gas Hydrate And Sediment Test Laboratory Instrument (GHASTLI). *Bulletin of the*

Geological Survey of Canada(544), 241-250.

Winters, W. (2011). *Physical and geotechnical properties of gas-hydrate-bearing sediment from offshore India and the northern Cascadia margin compared to other hydrate reservoirs.* Paper presented at the 7th International conference on gas hydrates, Edinburgh.

Winters, W., Walker, M., Hunter, R., Collett, T., Boswell, R., Rose, K., . . . Dandekar, A. (2011). Physical properties of sediment from the Mount Elbert gas hydrate stratigraphic test well, Alaska North Slope. *Marine and Petroleum Geology, 28*(2), 361-380.

Winters, W. J., Dillon, W. P., Pecher, I. A., & Mason, D. H. (2000). GHASTLI—Determining physical properties of sediment containing natural and laboratory-formed gas hydrate *Natural Gas Hydrate* (pp. 311-322): Springer.

Winters, W. J., Pecher, I. A., Waite, W. F., & Mason, D. H. (2004). Physical properties and rock physics models of sediment containing natural and laboratory-formed methane gas hydrate. *American Mineralogist, 89*(8-9), 1221-1227.

Winters, W. J., Pecher, I. A., Waite, W. F., & Mason, D. H. (2004). Physical properties and rock physics models of sediment containing natural and laboratory-formed methane gas hydrate. *American Mineralogist, 89*(8-9), 1221-1227.

Yun, T. S., Fratta, D., & Santamarina, J. C. (2010). Hydrate-bearing sediments from the Krishna− Godavari Basin: physical characterization, pressure core testing, and scaled production monitoring. *Energy & Fuels, 24*(11), 5972-5983.

Yun, T. S., Santamarina, J. C., & Ruppel, C. (2007). Mechanical properties of sand, silt, and clay containing tetrahydrofuran hydrate. *Journal of Geophysical Research: Solid Earth (1978–2012), 112*(B4).

Zhang, X., Lu, X., Shi, Y., & Xia, Z. (2015). Study on the mechanical properties of hydrate-

bearing silty clay. *Marine and Petroleum Geology, 67*, 72-80.